Politecnico di Torino

Master's Degree in Automotive Engineering

A.a. 2025/2026

July 2026

A vehicle simulation environment to validate rotary electromechanical shock absorbers

Supervisors:

Prof. Nicola Amati
Prof. Renato Galluzzi
Dr. Giulia Moscone
Dr. Giorgio Bisciaio

Candidate:

Carlo Centorame

Abstract

Suspension systems directly govern the interaction between the vehicle body and the road surface, influencing both ride comfort and vehicle stability. The inherent limitations of passive suspensions, whose parameters are fixed once and for all during the design phase, have motivated the development of semi-active and active technologies capable of adapting their behaviour in real time to changing operating conditions. The present thesis addresses the dynamic characterisation and control of vehicle suspension systems, taking the Alfa Romeo Stelvio as the reference platform. The work develops along three main directions. The opening part reviews passive, semi-active and active suspension configurations from both a conceptual and an analytical standpoint, deriving the equations of motion for each case through the two-degree-of-freedom quarter-car model and examining the main actuation technologies currently available, with particular attention devoted to electromechanical systems in light of their growing relevance in modern electrified vehicles. The central part describes the construction and validation of the vehicle model: the Alfa Romeo Stelvio is implemented and systematically calibrated in CarSim, then validated against the default reference configuration through an extensive simulation campaign covering multiple road surface types and handling manoeuvres, with both vertical and lateral dynamic responses examined. The final part focuses on the control layer, where two control strategies — the Skyhook and Groundhook algorithms — are implemented in MATLAB/Simulink, coupled with the CarSim model through a co-simulation interface, and assessed over the same operating conditions used during validation. The performance of each controller is quantified using both comfort-oriented and safety-oriented metrics, providing a consistent and meaningful comparison against the passive baseline.

Table of Contents

List of Figures

Chapter 1

Introduction

1.1 Vehicle suspension fundamentals

Vehicle suspension systems are among the most fundamental subsystems of a road vehicle, as they directly affect both dynamic performance and passenger comfort. Their design must simultaneously satisfy two primary objectives: ride comfort and road holding, which are often in conflict. Ride comfort refers to the ability to isolate the vehicle body, or sprung mass, from road surface irregularities, thereby reducing the accelerations transmitted to passengers. Road holding is related to the capability of maintaining adequate tire–road contact, which depends on the controlled motion of the unsprung mass, including wheels, hubs, brake components and associated linkages. In practice, soft damping improves comfort but tends to compromise tire grip, whereas stiffer settings enhance handling at the expense of ride quality [1].

The suspension acts as the mechanical interface between the vehicle and the road, absorbing shocks and vibrations generated by uneven surfaces, which represent the main disturbance acting on the system. Beyond basic isolation, an effective suspension must limit suspension deflection to avoid mechanical interference, minimize dynamic variations in tire load that degrade braking and cornering performance, and suppress undesirable body motions. These include vertical bouncing excited by road inputs, pitching during acceleration and braking, and rolling in cornering due to lateral load transfer.

From a modeling perspective, these phenomena are studied using mathematical representations of increasing complexity: the quarter-car model for single-wheel vertical dynamics, the half-car model to capture bounce-pitch coupling, and full-vehicle models for a complete description of ride and handling. These models are often combined with advanced control strategies, such as optimal and nonlinear control, to reduce body motions under a wide range of driving conditions [2].

1.2 Vehicle characterization and body motions

In a road vehicle, the suspension system provides the mechanical link between the wheels and the body. It serves two main purposes: on one hand, it must attenuate the shocks and vibrations generated by road irregularities before they reach the occupants and delicate components; on the other hand, it has to transmit the static weight and dynamic loads to the road through the tires, while preserving stability during acceleration, braking and cornering [3]. Managing these objectives is intrinsically difficult, because making the suspension more compliant generally improves ride comfort but tends to deteriorate handling and road-holding, and the opposite holds for a stiffer setup [4].

From the viewpoint of mass distribution, the vehicle can be modeled as a system composed of a sprung mass and an unsprung mass. The sprung mass includes the body, frame, interior, passengers and cargo, that is, all the elements whose weight is carried by the suspension units [5]. The unsprung mass, in contrast, groups the components that move essentially together with the wheels, such as hubs, bearings, tires, brake assemblies and a fraction of the suspension links directly attached to the wheel carriers [6]. The dynamic interaction between these two masses through the suspension springs and dampers has a decisive influence on both vertical comfort and the ability of the tires to follow the road profile [7].

The response of the vehicle to road inputs and driver manoeuvres can be conveniently described in terms of a few dominant rigid-body motions of the sprung mass. In the low-frequency range, the most relevant modes are:

- *Bouncing*, which corresponds to an almost pure vertical translation of the vehicle body and is strongly associated with the subjective perception of ride comfort on uneven roads;

- *Pitching*, a rotation about the lateral axis of the vehicle, mainly excited by longitudinal load transfer during acceleration and braking and manifested as squat and dive of the body;

- *Rolling*, a rotation about the longitudinal axis, primarily induced by lateral acceleration in cornering or asymmetric road excitation, with a direct impact on handling behaviour and the occupants' feeling of stability.

An effective suspension must control these dynamic motions within acceptable levels through the appropriate tuning of spring and damper characteristics and, where present, the implementation of suitable control strategies.

To meet these objectives, the suspension is required to satisfy several conflicting design criteria. It should restrict relative displacements to prevent mechanical interference and ensure operation within the designated suspension working space, while keeping the normal loads at the tire–road interface as uniform as possible to

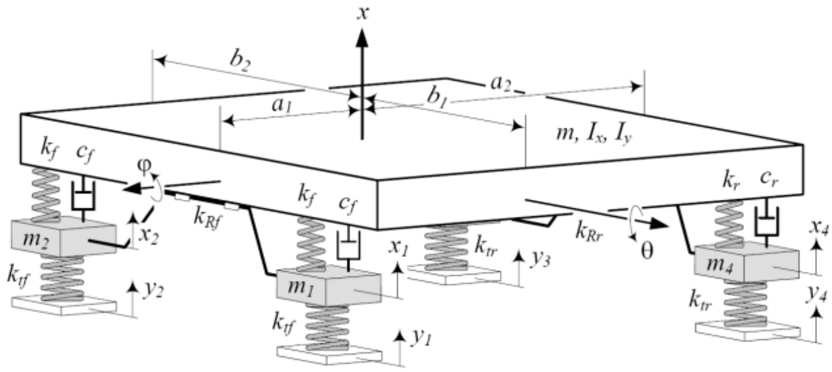

Figure 1.1: Full-car model - Physical schematic representation

ensure adequate grip. At the same time, it is expected to provide sufficient isolation for the occupants, to be lightweight, and to remain competitive in terms of cost and maintainability. The inherent compromise between ride comfort, road-holding and structural constraints has motivated the development of increasingly advanced suspension layouts and control solutions, which are addressed in the following sections. [8].

1.3 Suspension physical structure

After outlining the role of the suspension within the vehicle, together with the vehicle structure and the associated body motions, it becomes necessary to describe in greater detail the physical layout of the suspension system.

1.3.1 Suspension spring

The suspension spring is the elastic element that supports the vehicle's sprung mass and permits relative vertical motion between the body and the wheels. Its primary role is to carry the static weight of the vehicle while attenuating the effects of road irregularities, so that the motions transmitted to the occupants remain within acceptable comfort limits [5]. When a wheel encounters a bump, the spring compresses and converts part of the input into elastic potential energy; once the disturbance has passed, it extends and releases this energy, bringing the system back towards its equilibrium position [9, 10]. Without any damping, this sequence of compression and rebound would produce a long-lasting oscillatory motion, so the spring is always used together with a shock absorber that controls how quickly the stored energy is dissipated [10].

1.3.2 Suspension shock absorber

The shock absorber is the suspension component that damps the motion of the springs and dissipates the associated kinetic energy. Its main role is to control the oscillations of the sprung mass after a disturbance, so that the body motions decay quickly instead of persisting over time [11]. In this way, the damper contributes both to ride comfort and to maintain continuous tire contact with the road surface.

In a conventional hydraulic damper, a piston attached to a rod moves inside an oil-filled cylinder as the suspension compresses and rebounds. The fluid is forced through calibrated orifices and valves, which generate a resistive force approximately proportional to the piston velocity and convert the suspension motion into heat [12]. As a result, the spring and suspension movements are progressively reduced, and the system returns towards its equilibrium position within a few cycles.

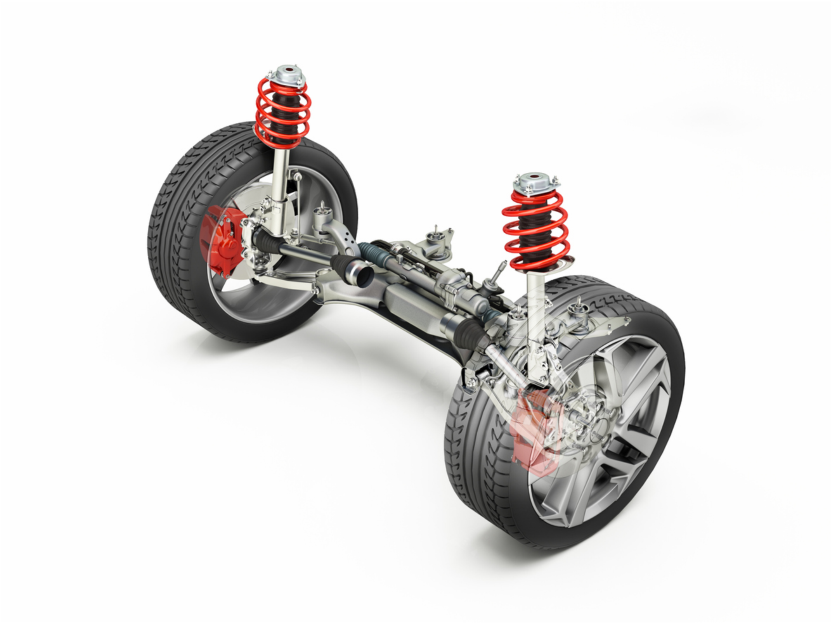

Figure 1.2: Physical layout of a vehicle suspension.

1.4 Chapter outline

This chapter has provided a general overview of the suspension system, from its functional role in the vehicle to the associated body motions and the main spring–damper components. The following chapter introduces the mathematical models of vertical vehicle dynamics that will be used as the foundation for the subsequent analysis and suspension control strategies.

Chapter 2

State of the art

2.1 Suspension types overview

Suspension systems for road vehicles are generally divided into three main categories: passive, semi-active and active suspensions. Each category is characterised by specific functional features and control requirements, which will be analysed separately in the following subsections.

2.1.1 Passive suspensions

A passive suspension system is defined by fixed mechanical properties of its main elements, namely the springs and dampers, which are specified at the design stage on the basis of the vehicle load capacity and dynamic performance targets [13]. The suspension can store energy in the elastic elements and dissipate it in the damping elements. However, as it cannot supply net energy to the system, its dynamic response is entirely governed by these preset parameters.
From an operational point of view, spring and damper are tuned to realize a compromise between ride comfort and road holding [14]. In particular:

- A relatively *low damping coefficient* improves isolation from high-frequency road irregularities and hence enhances comfort, but offers limited control of the resonances associated with the sprung and unsprung masses;
- On the other hand, a *high damping coefficient* provides better resonance suppression at the expense of transmitting more vibrations to the vehicle body.

Once the spring stiffness has been selected to satisfy static load requirements, the damper effectively becomes the main tuning element for the vertical dynamics, influencing bounce, pitch and roll motions and keeping the motion of both masses within acceptable bounds over the expected range of road profiles.

Despite their simplicity and robustness, passive suspensions can only provide a single, fixed trade-off between ride comfort and road holding, which is truly optimal only within a limited range of operating conditions, such as vehicle load and road excitation. When the actual conditions deviate significantly from those considered in the design, their performance inevitably degrades. This limitation has motivated the development of semi-active and active suspension systems, which can adapt their behaviour in real time [14].

2.1.2 Semi-active suspensions

A semi-active suspension system is defined by the presence of a controllable damper whose damping coefficient can be adjusted in real time by an electronic controller, while the spring element usually remains passive [15]. In contrast to passive suspensions, where spring and damper properties are fixed once selected during the design phase, semi-active suspensions are conceived to adapt their damping characteristics to changing operating conditions without altering the fundamental mechanical architecture of the suspension. In other words, they preserve the baseline passive spring–damper layout, integrating sensory and control systems to actively modulate the damping force..

Operationally, a semi-active suspension draws external power only to vary the damping level and to supply the embedded controller and sensors, but it does not inject net mechanical energy into the vehicle–road system [14]. The controller computes the desired damping force from measured quantities, such as accelerations or relative velocities, according to a given control law (for example, skyhook, groundhook or clipped-optimal), and then commands the damper so that the realized force remains within predefined limits, which may correspond to a small set of discrete damping levels or to an almost continuous range. Since the actual damping force still depends on both the selected damping coefficient and the relative velocity across the damper, semi-active suspensions retain a purely dissipative nature and act by modulating, rather than generating, forces.

Compared to purely passive suspensions, semi-active systems, therefore, offer a more adaptable balance between ride comfort and road holding, especially when the vehicle is subjected to highly variable operating conditions [15]. At the same time, they avoid the high energy demand and hardware complexity associated with fully active suspensions, because hydraulic actuators, pumps and accumulators are replaced by controllable dampers that rely on similar sensing and control hardware but operate with significantly lower power requirements.

2.1.3 Active suspensions

An active suspension system is distinguished by the use of a force actuator that generates a controlled interaction force between the sprung and unsprung masses, based on measurements from onboard sensors and a feedback control algorithm. In this configuration the actuator replaces the passive damper, or both the damper and the spring, and is able to both supply and dissipate energy, whereas a conventional damper can only dissipate it [14].

The mechanical layout still includes elastic elements and, in many designs, auxiliary damping, but the vertical forces transmitted between body and wheel are largely governed by the actuator force commanded by the controller. Since this force can be applied essentially independently of the instantaneous relative displacement or velocity across the suspension, the controller has a much wider authority to shape the vehicle response and to counteract the vertical loads produced by road irregularities and driving manoeuvres .

With an appropriate control strategy, active suspensions can therefore achieve a significantly improved balance between ride comfort and road holding compared with passive and semi-active systems, reducing both body accelerations and dynamic wheel loads over a broad range of operating conditions [14]. This enhanced performance is obtained at the expense of increased system complexity, higher energy consumption and more demanding reliability and fail-safe requirements, which currently limit the widespread adoption of fully active suspensions to high-end or specialised vehicle applications.

2.2 Analytical modelling of suspension systems

After having characterised the different suspension types from a purely theoretical standpoint, an analytical description of the topic is now introduced. To this purpose, the quarter-car model is adopted as the reference framework for the subsequent analysis, and its equations of motion are derived separately for each of the three suspension configurations considered.

2.2.1 Passive suspensions

A quarter-car model is a simplified, two-degree-of-freedom representation of a vehicle in which only the vertical dynamics of a single wheel–suspension assembly are taken into account. The sprung mass, approximating one quarter of the vehicle body, is linked to the unsprung mass, associated with the wheel and its attachments, by a suspension spring and damper, whereas the tyre is introduced as an additional elastic element between the unsprung mass and the road input.

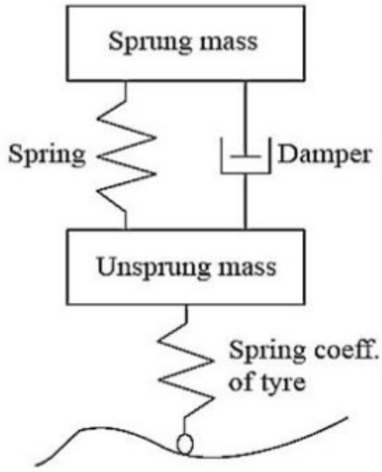

Figure 2.1: Passive quarter-car model - Physical schematic representation

A key modeling assumption is that the tire does not lose contact with the road surface; this is typically reasonable at low excitation frequencies but may become inaccurate when the vehicle encounters sharp irregularities of high - frequency.

To derive the equations of motion, it is first convenient to define the quantities that describe the internal deformations of the suspension system.

Symbol	Description	Unit
m_s	Sprung mass	kg
m_u	Unsprung mass	kg
k_s	Suspension spring stiffness	N/m
c_s	Suspension damping coefficient	N s/m
k_t	Tyre stiffness	N/m
c_t	Tyre damping coefficient	N s/m
z_s	Vertical displacement of the sprung mass	m
z_u	Vertical displacement of the unsprung mass	m
r	Road profile input	m

Table 2.1: Parameters of the passive quarter-car model.

The dynamic behaviour of the passive quarter-car model is described by the following equations of motion:

$$m\ddot{z}_s + c_s(\dot{z}_s - \dot{z}_u) + k_s(z_s - z_u) = 0 \tag{2.1}$$

$$m_u\ddot{z}_u + c_s(\dot{z}_u - \dot{z}_s) + c_t(\dot{z}_u - \dot{r}) + k_s(z_u - z_s) + k_t(z_u - r) = 0 \tag{2.2}$$

which can be rewritten in compact matrix form, called *configuration space*, as:

$$\begin{bmatrix} m_s & 0 \\ 0 & m_u \end{bmatrix} \begin{Bmatrix} \ddot{z}_s \\ \ddot{z}_u \end{Bmatrix} + \begin{bmatrix} c_s & -c_s \\ -c_s & c_s + c_t \end{bmatrix} \begin{Bmatrix} \dot{z}_s \\ \dot{z}_u \end{Bmatrix} + \begin{bmatrix} k_s & -k_s \\ -k_s & k_s + k_t \end{bmatrix} \begin{Bmatrix} z_s \\ z_u \end{Bmatrix} = \begin{Bmatrix} 0 \\ c_t\dot{r} + k_t r \end{Bmatrix} \tag{2.3}$$

2.2.2 Semi-active and active suspensions

From a mathematical standpoint, the analytical models for semi-active and active suspensions share the same structure as the passive quarter-car, with the key difference that an additional force term is introduced in the equations of motion. In the semi-active case this term is governed by a variable damping coefficient adjusted in real time by the controller, whereas in the active case it represents an independent actuator force that can be commanded regardless of the suspension kinematics.

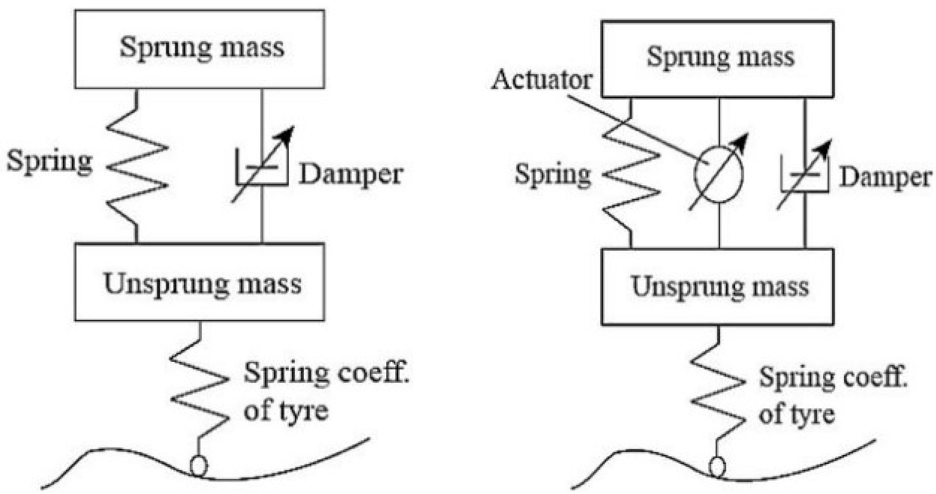

Figure 2.2: Semi-active and active quarter-car model - Physical schematic representation

The equations of motion of the *semi-active quarter-car model* are:

$$m_s\ddot{z}_s + c_s(t)(\dot{z}_s - \dot{z}_u) + k_s(z_s - z_u) = 0 \tag{2.4}$$

$$m_u\ddot{z}_u + c_s(t)(\dot{z}_u - \dot{z}_s) + c_t(\dot{z}_u - \dot{r}) + k_s(z_u - z_s) + k_t(z_u - r) = 0 \tag{2.5}$$

which can be rewritten in compact matrix form as:

$$\begin{bmatrix} m_s & 0 \\ 0 & m_u \end{bmatrix} \begin{Bmatrix} \ddot{z}_s \\ \ddot{z}_u \end{Bmatrix} + \begin{bmatrix} c_s(t) & -c_s(t) \\ -c_s(t) & c_s(t) + c_t \end{bmatrix} \begin{Bmatrix} \dot{z}_s \\ \dot{z}_u \end{Bmatrix} + \begin{bmatrix} k_s & -k_s \\ -k_s & k_s + k_t \end{bmatrix} \begin{Bmatrix} z_s \\ z_u \end{Bmatrix} = \begin{Bmatrix} 0 \\ c_t\dot{r} + k_t r \end{Bmatrix} \tag{2.6}$$

For the *active configuration*, the introduction of the actuator force F_a yields:

$$m_s\ddot{z}_s + c_s(\dot{z}_s - \dot{z}_u) + k_s(z_s - z_u) - F_a = 0 \tag{2.7}$$

$$m_u\ddot{z}_u + c_s(\dot{z}_u - \dot{z}_s) + c_t(\dot{z}_u - \dot{r}) + k_s(z_u - z_s) + k_t(z_u - r) + F_a = 0 \tag{2.8}$$

which in configuration space are:

$$\begin{bmatrix} m_s & 0 \\ 0 & m_u \end{bmatrix} \begin{Bmatrix} \ddot{z}_s \\ \ddot{z}_u \end{Bmatrix} + \begin{bmatrix} c_s & -c_s \\ -c_s & c_s + c_t \end{bmatrix} \begin{Bmatrix} \dot{z}_s \\ \dot{z}_u \end{Bmatrix} + \begin{bmatrix} k_s & -k_s \\ -k_s & k_s + k_t \end{bmatrix} \begin{Bmatrix} z_s \\ z_u \end{Bmatrix} = \begin{Bmatrix} F_a \\ c_t\dot{r} + k_t r - F_a \end{Bmatrix} \tag{2.9}$$

2.2.3 Conclusions

The analytical models derived for the three suspension configurations constitute the theoretical foundation upon which the control strategies and the simulation framework presented in the following chapters are built.

2.3 Semi-active suspension technologies

Semi-active suspensions achieve controllability through damping elements whose dissipative properties can be varied in real time by an external signal, without the need for active force generation. The following sections provide an overview of the most relevant technologies currently employed in this context.

2.3.1 Magnetorheological dampers

A magnetorheological damper is a controllable dissipative device whose behaviour is governed by the properties of magnetorheological fluids — suspensions of micron-sized ferromagnetic particles dispersed in a non-magnetic carrier medium, typically synthetic or silicone oil. In the absence of an external magnetic field, the particles remain randomly distributed within the fluid, which behaves as a conventional low-viscosity liquid and offers little resistance to flow. Upon application of a magnetic field, the particles rapidly organize into chain-like structures oriented along the field lines, producing a sharp and reversible increase in the fluid's apparent viscosity and yield stress. This transition takes place within a few milliseconds and is continuously tunable by adjusting the field intensity, which is the fundamental property that makes MR dampers suitable for real-time suspension control.[16]
The mechanical configuration of an MR damper determines how the fluid interacts with the moving components and, consequently, what levels of damping force can be achieved. Three operating modes are generally distinguished:

- In *shear mode*, the fluid is sheared between two surfaces in relative tangential motion, with the magnetic field applied perpendicularly to the direction of movement; this arrangement is compact and fast-responding but produces comparatively modest damping forces, limiting its use to rotary or space-constrained applications.

- In *flow mode*, the fluid is driven through a narrow channel or orifice by the piston motion, and the magnetic field acts across the flow path, increasing the resistance to flow and thus the damping force; this is by far the most common configuration in automotive applications, due to its ability to generate large and continuously variable forces over a wide stroke range.

- In *squeeze mode*, the fluid is compressed between two surfaces moving perpendicularly to the gap, yielding very high damping forces in a compact volume but over a very limited stroke, which restricts its applicability to specialized use cases.

In automotive semi-active suspensions, MR dampers operate almost exclusively in flow mode, with the electromagnetic coil embedded in the piston assembly and supplied by a current signal generated by the vehicle's electronic control unit.[16]
The damping force is thus modulated continuously between a passive lower bound, corresponding to the unexcited state of the coil, and an upper bound set by the magnetic saturation of the fluid. This mechanism combines the mechanical robustness and inherent fail-safe nature of a passive hydraulic damper with a level of real-time controllability that would otherwise demand fully active actuation, making MR dampers one of the most technically mature and industrially established solutions in the field of semi-active vehicle suspensions.

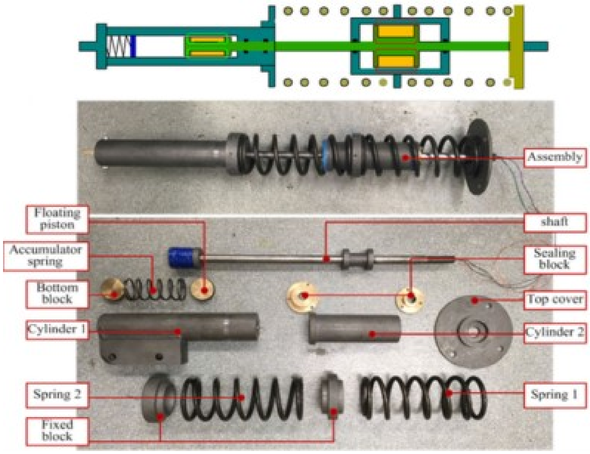

Figure 2.3: Magnetorheological damper with 2 springs

Among the more advanced MR damper configurations proposed in the literature, some designs extend the conventional single-cylinder layout by integrating variable stiffness capabilities alongside the standard variable damping function. In one such architecture, two MR cylinders are arranged in series along a common piston rod, each governed by an independent current input, and two springs of different stiffness are incorporated into the assembly.[17] The effective stiffness of the device is not fixed, but depends on how much relative motion is permitted between the piston rod and the upper cylinder: a low current in the upper coil leaves the upper spring free to deform in series with the lower one, yielding a soft overall response, whereas a progressively higher current restricts that motion and gradually transfers the elastic load to the lower spring alone, stiffening the device. At full activation of the upper coil, only the lower spring remains mechanically engaged and the stiffness reaches its maximum value. The damping level, independently set by the lower coil current, can be varied across its full range regardless of the stiffness state. This decoupled control of stiffness and damping represents a meaningful extension of the standard MR damper concept, offering a broader and more flexible operating envelope for suspension control applications.

2.3.2 Electrorheological dampers

Electrorheological dampers rely on the same operational concept as MR dampers, with the key difference that the controllable fluid responds to an electric field rather than a magnetic one. An ER fluid consists of polarizable particles suspended in a non-conducting carrier liquid; when an external voltage is applied across the fluid, the particles organize into chain-like structures that significantly increase the fluid's resistance to flow, raising both its apparent viscosity and yield stress. This process is fully reversible and takes place within a few milliseconds, making ER dampers inherently compatible with real-time control applications. Structurally, the device consists of a piston that separates two fluid-filled chambers, with the inner and outer cylinders serving as the positive and negative electrodes, respectively. As the piston moves, the ER fluid is forced through the annular gap between the electrodes, where the applied electric field governs its flow resistance. With no voltage applied, the damper behaves as a passive viscous element; as the field intensity increases, an additional damping force is generated on top of the baseline viscous contribution, and this force can be continuously adjusted by varying the supply voltage. Despite their fast response and simple mechanical layout, ER dampers present some practical limitations compared to MR devices. The high voltages required — typically in the kilovolt range — demand dedicated power electronics and careful electrical insulation, increasing system complexity. Furthermore, the achievable damping force range is generally narrower than that of MR dampers, which has restricted the adoption of ER technology in series production vehicles.[18]

2.4 Active suspension technologies

Active suspension systems demand a fundamentally different hardware approach, as the damping element is replaced by a force actuator capable of both injecting and dissipating energy into the suspension. The following sections examine the main actuation technologies currently employed in automotive active suspensions.

2.4.1 Electromechanical actuators

Electromechanical actuators represent one of the most promising technologies for active suspension systems, driven by the increasing demand for energy efficiency and compatibility with vehicle electrification.[19] Unlike hydraulic systems, which rely on continuous fluid pressurization and require complex auxiliary circuits, electromechanical actuators generate a controlled force or torque directly between the sprung and unsprung masses, offering a simpler architecture, reduced energy consumption, and wider frequency bandwidth.
Depending on the geometric layout, two main configurations can be identified:

- In *linear actuators*, force is generated directly along the vertical axis of suspension travel through the electromagnetic interaction between a permanent magnet array and a set of electrical windings, enabling a direct-drive solution with fast dynamic response and high control precision.

- In *rotary actuators*, a rotating electric motor is coupled with a motion conversion mechanism — typically a ball screw or a magnetic lead screw —

which transforms the motor torque into a controllable linear force along the suspension axis. This configuration inherently allows the system to operate in regenerative mode, recovering kinetic energy during suspension travel and converting it into electrical energy.[19]

The general operating principle of an electromechanical active suspension follows a closed-loop logic articulated in sequential stages:

- *Sensing*: sensors distributed across the vehicle continuously monitor the dynamic states of the system, acquiring body accelerations, wheel displacements, and driver inputs.
- *Processing*: the ECU processes the acquired signals in real time and computes the force or torque demand at each corner according to the adopted control strategy.
- *Actuation*: the electric motor generates the commanded force between the sprung and unsprung masses, actively compensating for road disturbances and managing the chassis attitude in roll, pitch and heave;
- *Energy recovery*: when operating in regenerative mode, the actuator behaves as a generator, converting the kinetic energy associated with suspension travel into recoverable electrical energy, thus contributing to the overall efficiency of the vehicle.

Among the electromechanical actuator configurations investigated in the literature, the *Rotary regenerative shock absorber* stands out as a particularly complete solution. In this architecture, the linear suspension motion is converted into angular displacement through a linkage and a planetary gearbox, whose output shaft drives a permanent-magnet synchronous machine [20]. The device is designed to simultaneously fulfil an active damping function and recover part of the energy dissipated by road-induced vibrations, which can be stored in an on-board battery.

The electric machine at the core of the system can operate in two distinct modes depending on the control strategy applied. When commanded as a motor, it draws power from its electrical supply and exerts a controlled force on the suspension; when operating as a generator, it exploits the relative motion between sprung and unsprung masses to perform mechanical-to-electrical energy conversion. The linkage connects the wheel upright to the gearbox input shaft, which acts as a speed multiplier to match the slow oscillatory motion of the suspension with the higher rotational speed required by the machine. The transmission ratio between the suspension linear speed and the machine angular speed is a key design variable, since it simultaneously governs the torque and size requirements of the electric machine and the magnitude of the equivalent damping introduced by mechanical losses in the transmission. Low values of this ratio lead to compact and lightweight machines, but magnify the dissipative contribution of gearbox friction; high values extend the force output range at the expense of a larger and heavier machine [20].

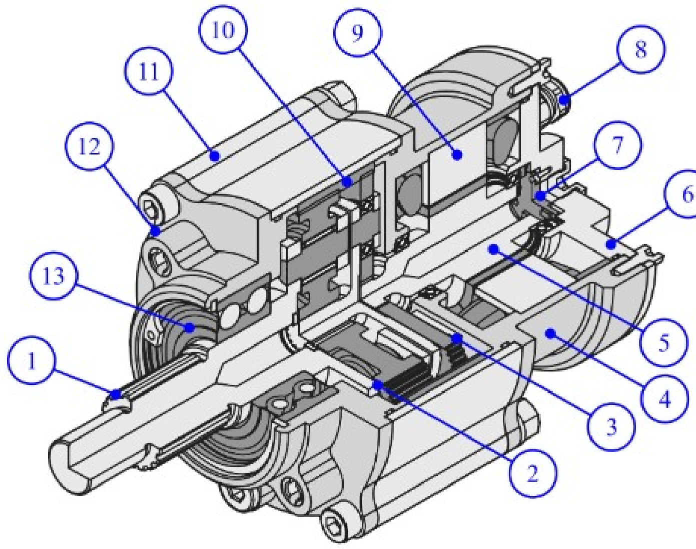

Figure 2.4: Isometric cut view of the rotary regenerative damper prototype.[20] Splined input shaft (1), first stage (2), second stage (3), motor casing (4), rotor (5), back cover (6), angular position sensor (7), cable gland [×4] (8), stator (9), outer ring gear (10), gearbox casing (11), front cover (12), input bearing (13).

Experimental validation of a prototype RRSA [20] confirmed the effectiveness of this architecture across three performance dimensions: damping capability, energy recovery efficiency and acoustic behaviour.

In terms of *damping*, the prototype achieved a damping-to-mass ratio of 3.23 kNs/(m · kg), which exceeds the maximum value of 2.44 kNs/(m · kg) documented in the literature for comparable regenerative suspension technologies. This result was primarily attributed to the reduced bulk and added mass characteristic of the rotary layout compared to alternative implementations.

Regarding *energy recovery*, the device demonstrated a maximum total conversion efficiency of 59.86%, sustained above 50% over a broad operating range spanning suspension speeds between 0.12 and 0.9 m/s. These figures compare favorably with electrohydrostatic solutions, which rarely achieve efficiencies beyond 40% and are further penalized by the simultaneous presence of volumetric and hydro-mechanical losses that restrict high-efficiency operation to a narrow portion of the force-speed envelope. State-of-the-art electromechanical alternatives report mechanical efficiencies in the 60–70% range, which are further reduced once the losses of the electric machine are included.

Acoustic characterization showed that prototype noise levels remain within standard limits throughout the relevant operating range, confirming the suitability of the rotary architecture for passenger vehicle applications.

2.4.2 Electrohydraulic actuators

Electrohydraulic active suspension systems represent one of the most established fully active technologies in the automotive field, characterized by high force density, technological maturity and wide commercial availability of components [21, 19]. In this configuration, a hydraulic actuator is interposed between the sprung and unsprung masses and controlled by a central ECU through low-power electromagnetic valves, which regulate the fluid flow and thus the force output at each wheel corner independently. The hydraulic energy is supplied by a pump driven either by the internal combustion engine or by a dedicated electric motor, drawing power from the vehicle electrical system [21].

The operating principle follows a closed-loop logic: onboard sensors — including vehicle height sensors, accelerometers, and inertial measurement units — continuously monitor the dynamic state of the vehicle and transmit signals to the ECU, which processes this information and commands the hydraulic valves to adjust the oil pressure in each suspension strut. The resulting forces actively compensate for road disturbances and manage the chassis attitude in roll, pitch and heave [21, 19]. Due to the inherently limited bandwidth of hydraulic circuits, these systems are primarily suited for *low-bandwidth* applications, effectively controlling body motions up to approximately 3 Hz, while higher-frequency road-induced vibrations are attenuated by the passive elements of the suspension [22].

A representative industrial example is the Mercedes-Benz *Active Body Control (ABC)* system, introduced in series production in 1999 [19]. In this system, hydraulic struts are positioned between the wheels and the vehicle body, and high-pressure hydraulics pre-stress the suspension springs to generate anti-roll forces independently at each wheel, without the need for a conventional anti-roll bar. The ECU continuously analyzes sensor signals and adjusts the oil flow into each strut to counteract body roll, pitch and vertical motion. A road surface scan function was later introduced to enable predictive control, responding to the road profile up to 15 m ahead of the vehicle at speeds of up to 130 km/h [19].

Despite their maturity and high force output, electrohydraulic systems present notable limitations: the need for continuous hydraulic pressurization results in significant energy consumption, the auxiliary circuits introduce additional weight and mechanical complexity, and no energy recovery is possible, as the dissipated energy is lost in the form of heat [19, 22]. These drawbacks have historically confined their adoption to high-end luxury vehicles.

2.5 CarSim Simulation Software

2.5.1 Introduction

The growing complexity of modern vehicle development programs has made physical testing alone an insufficient and economically unsustainable approach to subsystem validation. As product development timelines continue to compress, automotive engineers increasingly rely on high-fidelity numerical simulation to evaluate vehicle behaviour across a wide range of operating conditions before any hardware prototype is built [23]. In this context, simulation environments capable of reproducing full-vehicle dynamics with engineering-grade accuracy have become integral to the development workflow, enabling virtual experimentation at a fraction of the cost and time associated with instrumented road tests.

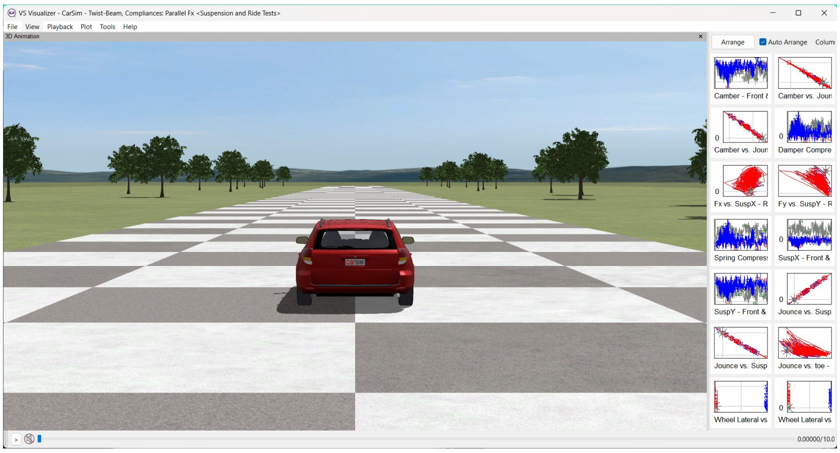

Figure 2.5: CarSim interface example

CarSim, developed by Mechanical Simulation Corporation (MSC), is a vehicle dynamics simulation platform whose mathematical core originates from research activity carried out at the University of Michigan Transportation Research Institute (UMTRI) [23]. The software follows a parametric modeling approach: each vehicle subsystem is defined through a set of performance-oriented parameters rather than through its detailed structural geometry, which reduces model setup time without sacrificing the physical accuracy required for engineering analysis [23]. The platform supports both open-loop and closed-loop simulation configurations, making it equally applicable to steady-state performance characterization and to the design and evaluation of active control systems [23]. Its native interface with MATLAB/Simulink further extends its applicability to controller-in-the-loop workflows, where the vehicle model and the control algorithm run simultaneously within a co-simulation environment [24]. As noted in recent comprehensive reviews of active suspension technologies, CarSim belongs to the class of simulation platforms that provide accurate and realistic evaluation of suspension performance metrics such as ride comfort, road holding and energy consumption.

2.5.2 Software Architecture

CarSim is organized around three main components: a graphical database, a mathematical solver and a post-processing module [23].

- The *graphical database* represents the primary user interface, where all vehicle and simulation parameters are defined and stored across dedicated panels, covering subsystems such as suspension kinematics, tire characteristics, steering and braking settings, driver model and road surface definitions [23].
- The *mathematical solver* computes the vehicle dynamic response based on a multibody model that schematizes the vehicle as ten rigid bodies, yielding a system with 27 degrees of freedom that captures the dynamics of the sprung mass, the four unsprung masses, the wheel assemblies and the powertrain [23]. The solver also supports co-simulation with external environments, most notably MATLAB/Simulink, through a dedicated S-Function interface [24].
- Finally, the *post-processing module* allows the user to visualize simulation results through a 3D animation viewer and a signal plotter, with the possibility to export output data to external tools such as MATLAB or Microsoft Excel for further analysis [23].

2.5.3 Applications to Vehicle Dynamics Research

CarSim has been applied across a broad range of vehicle dynamics problems, spanning lateral and longitudinal stability analysis, active safety system evaluation, and road surface response characterization.

- In the area of *lateral dynamics*, studies using CarSim have demonstrated its ability to reproduce steering response characteristics with good accuracy relative to experimental measurements collected on instrumented test vehicles [23]. The software supports ISO-defined test procedures including steady-state circular driving (ISO 4138), step and sinusoidal steering input (ISO 7401), braking in a turn (ISO 7975) and double lane change maneuvers, enabling systematic characterization of handling limits across representative driving conditions [19].
- For the assessment of *vertical dynamics*, CarSim supports the generation of road surface profiles conforming to the ISO 8608 standard, covering roughness classes

from A to H. These profiles can be synthetically generated as filtered white noise sequences or imported from measured data. Non-standard road events such as speed bumps and isolated obstacles can also be defined, providing flexible excitation inputs for transient vertical response analysis. The availability of standardized and reproducible road inputs is particularly important in suspension research, where consistent excitation conditions are required for fair comparison between different configurations and control strategies [19].

2.5.4 CarSim in Semi-Active and Active Suspension Research

In the specific domain of semi-active and active suspension research, which constitutes the central focus of the present thesis, CarSim serves as the full-vehicle simulation environment within which the proposed control strategies are validated. By coupling CarSim with a Simulink-based controller model, suspension performance can be evaluated under the simultaneous influence of longitudinal, lateral and vertical vehicle dynamics — a level of completeness that simplified quarter-car or half-car models cannot provide [19].

The co-simulation architecture exploits the S-Function interface to maintain a clear separation between the plant model and the control logic: the suspension controller is designed and tuned within Simulink, while the full nonlinear vehicle response is computed by the CarSim solver at each integration step [24, 23]. This approach has been adopted in the literature for the evaluation of strategies ranging from skyhook and groundhook control to LQR, H-infinity and model predictive control formulations [19].

Key performance indicators extracted from CarSim output channels include the vertical acceleration of the sprung mass — as a proxy for passenger ride comfort — the dynamic tire force variation — related to road holding and lateral stability — and the suspension deflection — relevant to stroke constraints and actuator sizing. These quantities provide the quantitative basis for comparing passive, semi-active and active configurations under identical excitation conditions and driving maneuvers [19, 23].

Chapter 3

Vehicle model development and testing

3.1 Vehicle model development

3.1.1 The Reference Vehicle: Alfa Romeo Stelvio

The reference vehicle considered in this work is the Alfa Romeo Stelvio, the first crossover SUV introduced by the Italian manufacturer and named after the renowned Alpine pass. It is developed on the modular "Giorgio" platform, sharing most of its mechanical layout with the Giulia sedan, but with specific adaptations to meet the requirements of the SUV segment, such as increased ground clearance and extended suspension travel for improved ride comfort on uneven roads.

Figure 3.1: Alfa Romeo Stelvio model

Offered in both rear-wheel and all-wheel-drive configurations, the Stelvio was designed to combine everyday utility with a strong focus on driving dynamics. Over its production cycle, successive updates have enhanced its onboard technology and interior quality, consolidating its position in the premium SUV segment. Thanks to this balance between handling precision, structural stiffness and suspension travel, the model provides a suitable benchmark for the development and assessment of advanced suspension control strategies.

In this thesis, the vehicle is represented by a virtual prototype built in the CarSim environment. The model has been parametrized using the structural, inertial and kinematic data supplied by the manufacturer, together with the suspension and damper characteristics measured on the front and rear axles. This parametrization aims at reproducing as closely as possible the on-road behaviour of the real vehicle in the vertical and lateral dynamics domains, relevant to ride comfort and handling.

3.1.2 Vehicle Parametrization and Experimental Datasets

This section describes the parametrization of the CarSim model of the Alfa Romeo Stelvio, following the same sequence adopted during the model development. Starting from the basic vehicle data, the front and rear suspension characteristics and the corresponding spring and damper curves are progressively implemented, using the datasets provided by the manufacturer.

As a first step, the main geometric, elastic and inertial characteristics of the vehicle are defined. In particular, the geometric dimensions and the elastic properties of the suspension system are directly taken from the manufacturer-specific dataset, as summarised in Table 3.1.

Parameter	**Symbol**	**Value**
Wheelbase	L	2.818 m
Front wheelbase	l_1	1.536 m
Rear wheelbase	l_2	1.282 m
Front track width	t_1	1.615 m
Rear track width	t_2	1.655 m
Sprung mass	m_s	1 537 kg
Total unsprung mass	m_u	220 kg
Wheel free radius	R_{wh}	0.379 m
Height of sprung-mass CoG	Z_{Cog}	0.613 m
Front anti-roll bar stiffness	$K_{\mathrm{arb},f}$	39 250 N/m
Rear anti-roll bar stiffness	$K_{\mathrm{arb},r}$	6 300 N/m

Table 3.1: Main geometric and elastic parameters implemented in the CarSim model.

In addition to these quantities, the inertial parameters of the **sprung mass** are estimated from the available mass and geometry data. In particular, the front and rear contributions to the sprung mass are obtained from the static load distribution along the wheelbase, using the distances between the centre of gravity and the axles. This leads to the following expressions:

$$m_1 = m_s \frac{l_2}{L}, \qquad m_2 = m_s \frac{l_1}{L},$$

The roll, pitch and yaw moments of inertia of the sprung mass are then computed in a consistent way by lumping the masses m_1 and m_2 at the corresponding axle locations and track widths. Under this assumption, the inertial properties used in the CarSim model are given by:

$$\begin{aligned} I_{xx} &= m_1 \frac{t_1^2}{4} + m_2 \frac{t_2^2}{4}, \\ I_{yy} &= (m_1 + m_2)\, l_1\, l_2, \\ I_{zz} &= m_1 \left(\frac{t_1^2}{4} + l_1^2 \right) + m_2 \left(\frac{t_2^2}{4} + l_2^2 \right). \end{aligned}$$

These relations provide a compact approximation of the vehicle body inertias that is fully compatible with the geometric parameters reported in Table 3.1.
The geometric configuration of the sprung mass and the position of its centre of gravity in the CarSim model are illustrated in Figure 3.2.

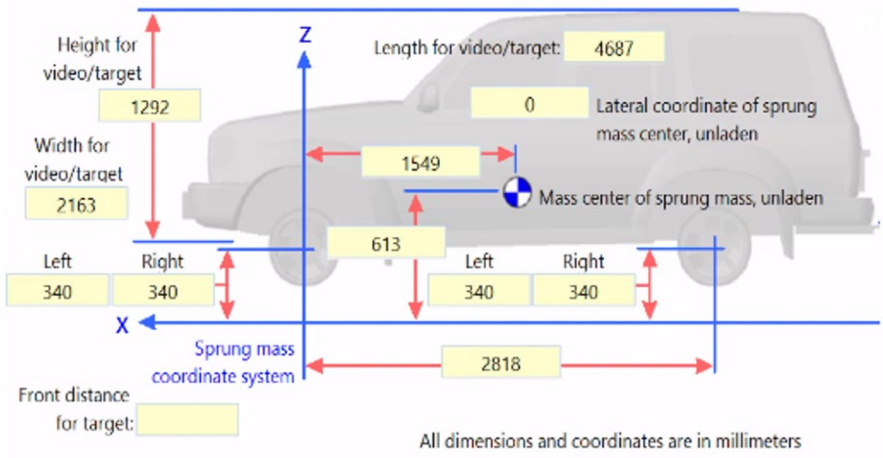

Figure 3.2: CarSim interface defining the geometric layout and the coordinate system of the sprung mass

In a similar way, Figure 3.3 shows the CarSim interface in which the inertial properties of the sprung mass are specified. It is important to point out that the roll, pitch and yaw moments of inertia reported in this window are consistent with the analytical expressions derived above.

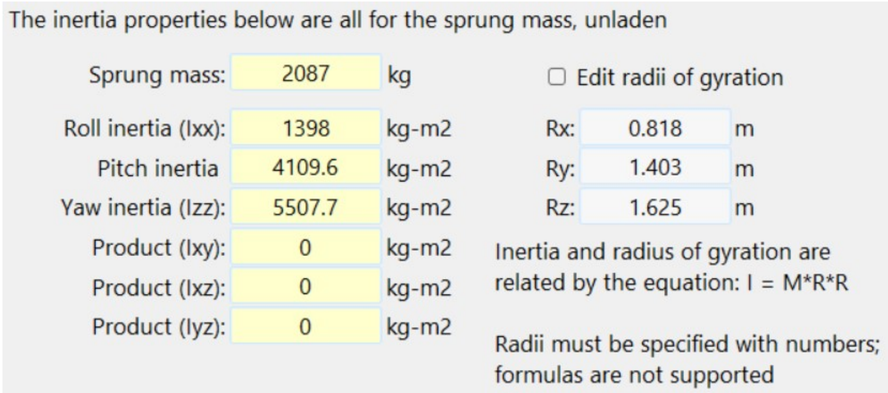

Figure 3.3: Sprung-mass inertial properties: mass, roll, pitch and yaw moments of inertia and the associated radii of gyration.

After defining the properties of the sprung mass, the parametrization of the **unsprung masses** and of the **suspension kinematics** is carried out for the front and rear axles. For each axle, CarSim requires the unsprung masses, the geometric position of the wheel centres and a set of kinematic relationships as functions of wheel jounce.

Starting from the total unsprung mass values provided in the dataset, the unsprung mass and inertia properties are specified for each axle in the "Mass and Inertia" fields, as shown in Figure 3.4.

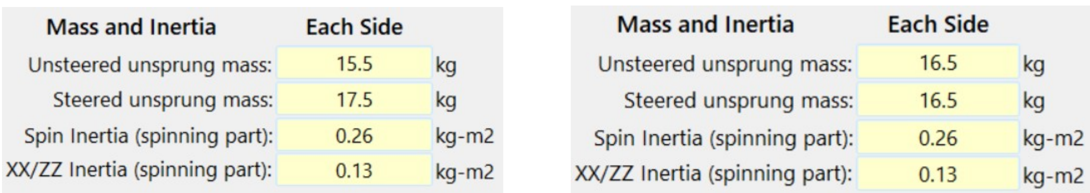

(a) Front axle. **(b)** Rear axle.

Figure 3.4: Unsprung mass and inertia properties for the front and rear axles

In this window, the unsteered and steered unsprung masses per side, the spin inertia and the XX/ZZ inertia of the spinning parts are specified so that the vertical dynamics of the wheel–tire assemblies are correctly represented in the model.

In addition, it is important to point out that the value of the steered unsprung mass is entered without including the tire mass, since the tire mass is handled separately in the CarSim *Tyres* section. To better clarify this point, the following calculations can be reported. Given a total front unsprung mass of 39.5 kg per side and a tire mass of 22 kg, the steered unsprung mass for the front axle is:

$$m_{\text{u,front}}^{\text{steered}} = 39.5 - 22 = 17.5 \text{ kg}.$$

Similarly, for the rear axle, with a total rear unsprung mass of 38.5 kg per side and the same tire mass, the steered unsprung mass is:

$$m_{\text{u,rear}}^{\text{steered}} = 38.5 - 22 = 16.5 \text{ kg}.$$

Once the unsprung mass and inertia properties have been defined, the kinematics definition starts from the geometric layout of the wheel centres. In the "Independent System Kinematics" window of CarSim, their position with respect to the sprung-mass origin is set according to the manufacturer data, as shown in Figure 3.5a for the front axle and in Figure 3.5b for the rear axle.

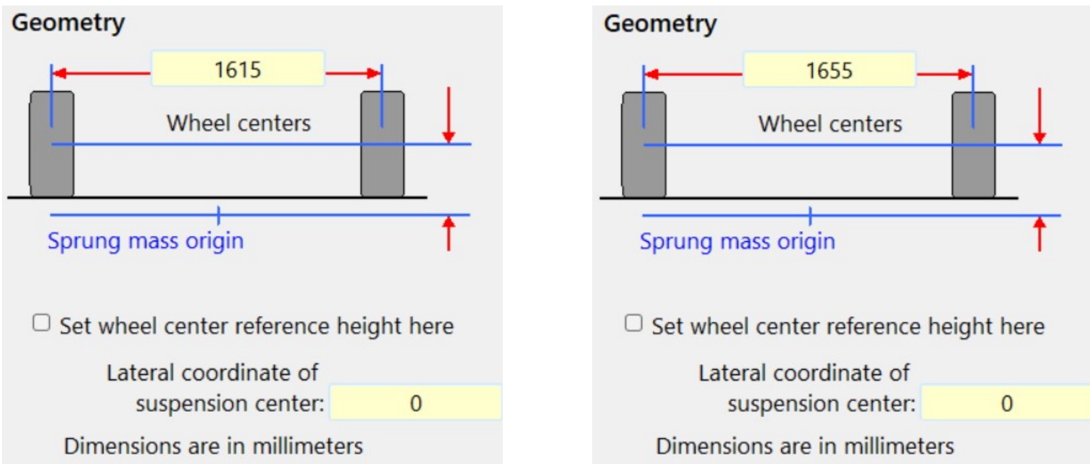

(a) Front axle. **(b)** Rear axle.

Figure 3.5: Unsprung mass geometric properties for the front and rear axles as defined in the CarSim kinematics interface.

Moreover, the geometry block includes the lateral coordinate of the suspension centre. In the present model this coordinate is set to zero, so that the suspension centre lies on the vehicle longitudinal symmetry plane. This information ensures that the geometry of the unsprung assemblies is consistently represented in the model.

Once the geometric layout of the wheel centres and the suspension centre has been defined, the suspension kinematics are specified in terms of their variation with wheel jounce. In the CarSim kinematics interface, the main kinematic relationships (such as wheel camber, toe angle and lateral/longitudinal wheel centre displacements) are provided as functions of wheel jounce in dedicated lookup tables for the front and rear axles. In particular:

- the *longitudinal displacement* of the wheel centre versus jounce curve quantifies the fore–aft motion of the wheel centre produced by the suspension links under bump and rebound;
- the *wheel camber angle* versus jounce curve describes how the inclination of the wheel plane with respect to the vertical changes as the suspension travels;
- the *lateral displacement* of the wheel centre versus jounce curve represents the inboard/outboard motion of the wheel centre induced by the suspension geometry;
- the *wheel toe angle* versus jounce curve expresses the variation of the wheel heading direction relative to the vehicle longitudinal axis as a function of jounce.

Following the order of the above list, the corresponding kinematic curves as functions of wheel jounce are reported in the next figures for the front and rear axles. These curves are obtained from the lookup tables of kinematic data provided by the vehicle manufacturer and implemented in the CarSim suspension model.

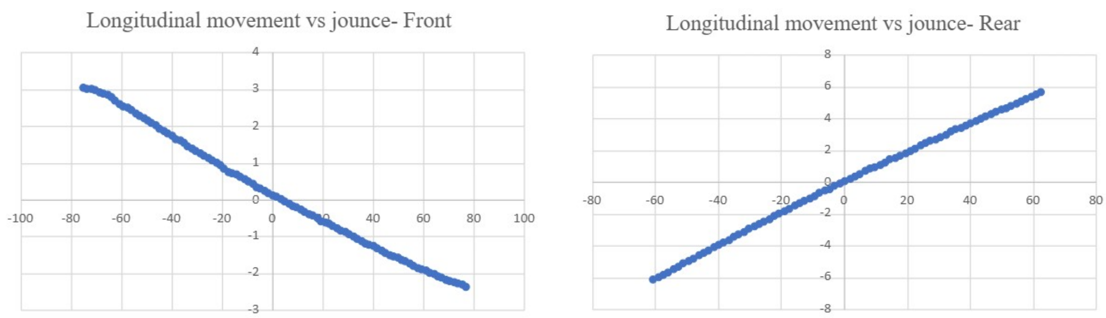

Figure 3.6: Longitudinal movement of the wheel centres versus jounce for the front and rear axles.

The front curve shows a rearward movement of the wheel centre in bump and a forward movement in rebound, whereas the rear curve exhibits the opposite trend, consistently with the suspension geometry adopted in the vehicle.

After the longitudinal movement–jounce relationship, the second kinematic parameter considered is the wheel camber angle as a function of jounce. The plots of the wheel camber angle for the two axles are reported in the figures below.

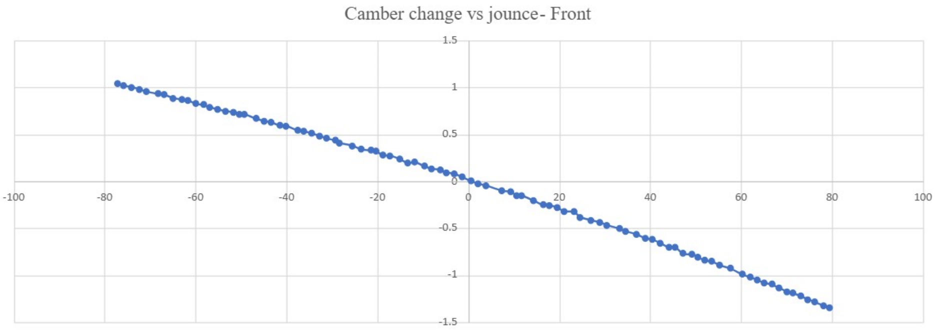

(a) Front axle.

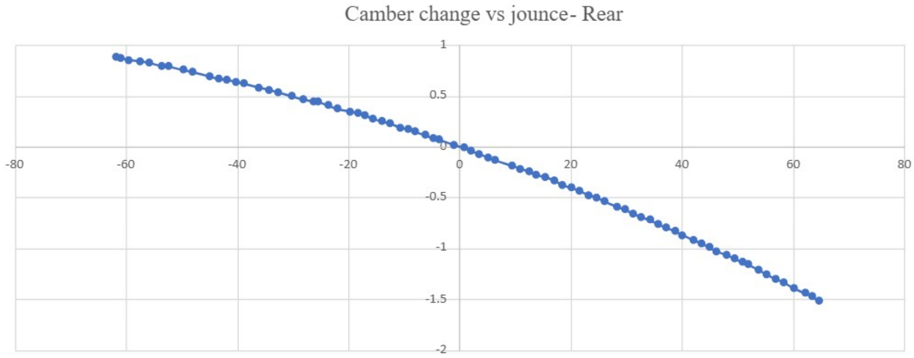

(b) Rear axle.

Figure 3.7: Wheel camber angle versus jounce for the front and rear axles.

The figures show a progressive change of camber with wheel jounce, with increasingly negative camber in bump and positive camber in rebound, consistently with the suspension geometry adopted in the vehicle.

After the camber–jounce relationship, the next kinematic parameter considered is the lateral movement of the wheel centres as a function of jounce. The lateral displacement–jounce curves describe the inboard or outboard motion of the wheels induced by the suspension links during bump and rebound, As for the other kinematic relationships, the two lateral movement–jounce curves are obtained from the lookup tables of lateral kinematic data supplied by the vehicle manufacturer and implemented in the CarSim suspension model. The corresponding plots for the front and rear axles are reported below.

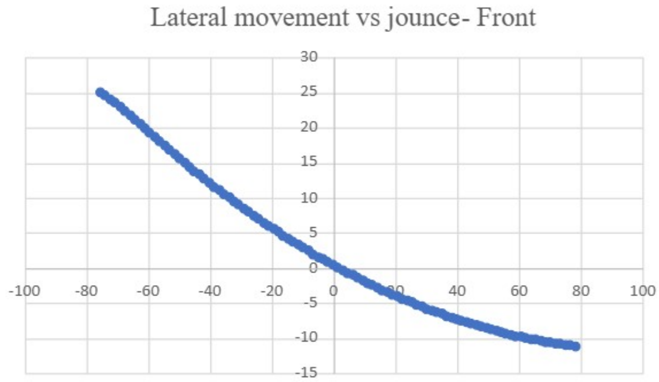

(a) Front axle.

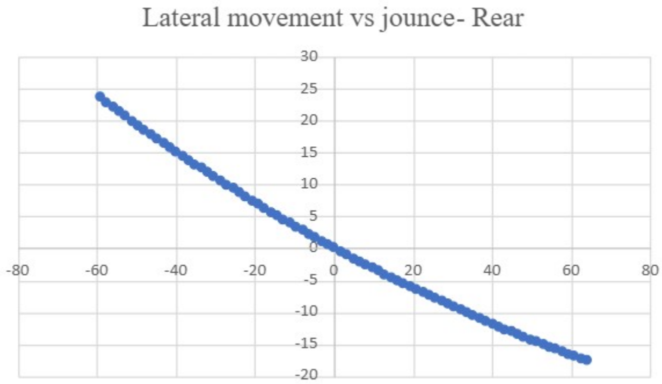

(b) Rear axle.

Figure 3.8: Lateral movement of the wheel centres versus jounce for the front and rear axles.

For both axles, the lateral displacement decreases monotonically with jounce, indicating an inboard motion of the wheel centres in bump and an outboard motion in rebound.

After the lateral movement–jounce relationship, the last kinematic parameter considered is the wheel toe angle. The toe–jounce curves describe how the wheel heading direction relative to the vehicle longitudinal axis changes as the suspension moves in bump and rebound.

For the front axle, the toe angle shows a nearly linear trend, with positive toe in rebound that gradually turns into negative toe as jounce increases. The rear axle exhibits a different behaviour, with toe starting from a relatively high positive value in rebound and quickly decreasing towards a small positive toe around the nominal ride height, then remaining almost constant for increasing jounce. The corresponding plots for the front and rear axles are reported below.

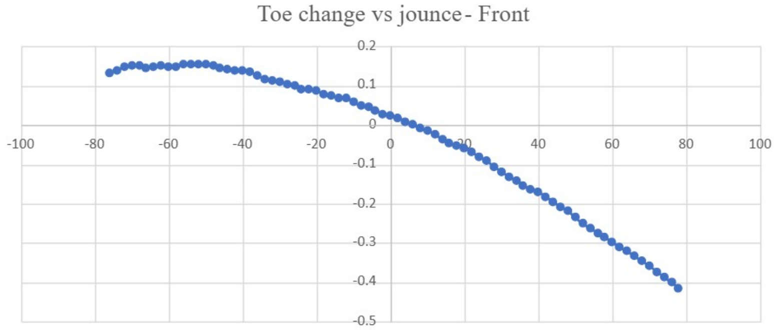

(a) Front axle.

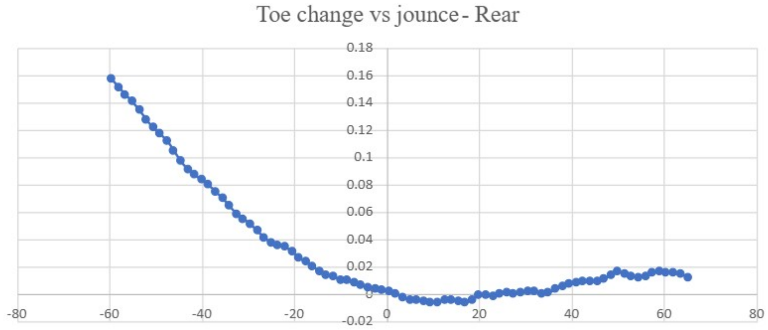

(b) Rear axle.

Figure 3.9: Wheel toe angle versus jounce for the front and rear axles.

After the definition of the kinematic relationships as functions of wheel jounce, the parametrization of the suspension is completed in the subsection *Spring, dampers and compliance*. In this subsection, the spring force–spring compression and damper force–damper compression rate characteristics of the elastic and damping elements are specified. In particular:

- *Spring force vs spring compression curve*: describes the variation of the vertical force transmitted by the suspension as a function of spring compression, thereby determining the effective stiffness at the wheels over the operating range of vertical travel;
- *Damper force vs damper compression rate curve*: relates the damping force to the suspension velocity in bump and rebound, and is responsible for controlling the attenuation of vertical oscillations and the transient response of the sprung mass.

In the present model, the spring force–compression and damper force–velocity relationships for the front and rear axles are implemented in CarSim using the datasets provided by the vehicle manufacturer.

Following the above definitions, the first curve that is reported is the spring force–spring compression relationship.

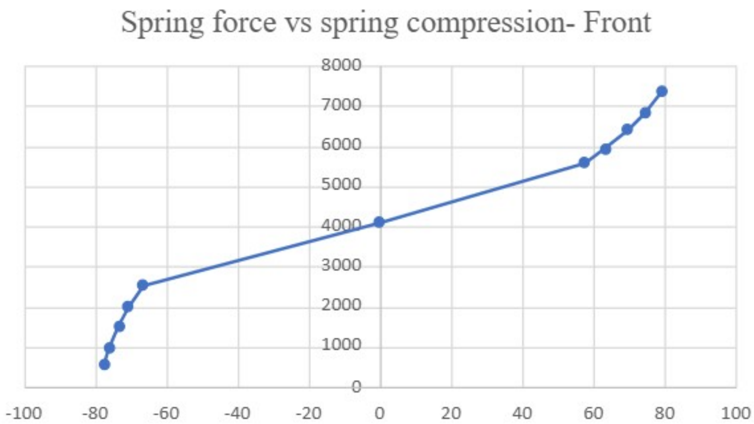

(a) Front axle.

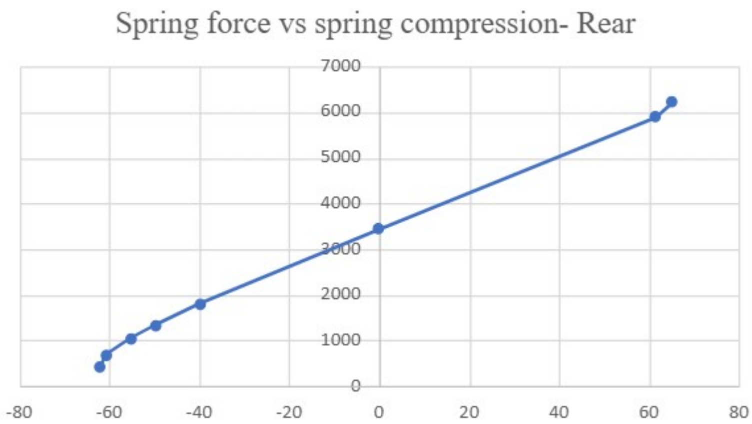

(b) Rear axle.

Figure 3.10: Spring force versus spring compression for the front and rear axles.

For the front axle, the curve presents a nearly linear increase of spring force with compression in the central range, with a softer behaviour at low compression and a steeper stiffness at high compression, reflecting the progressive characteristic of the front suspension. The rear axle exhibits a more uniform trend, with an almost linear increase of force over the whole compression range, corresponding to a more constant effective spring rate at the rear.

The second curve that we are going to report to conclude the vehicle model characterization is the shock absorber force as a function of damper compression rate. This plot characterizes the damping behaviour of the suspension, showing how the force generated by the shock absorber increases with the compression velocity in bump and rebound, and therefore how the damper controls the rate at which the suspension moves and dissipates energy.

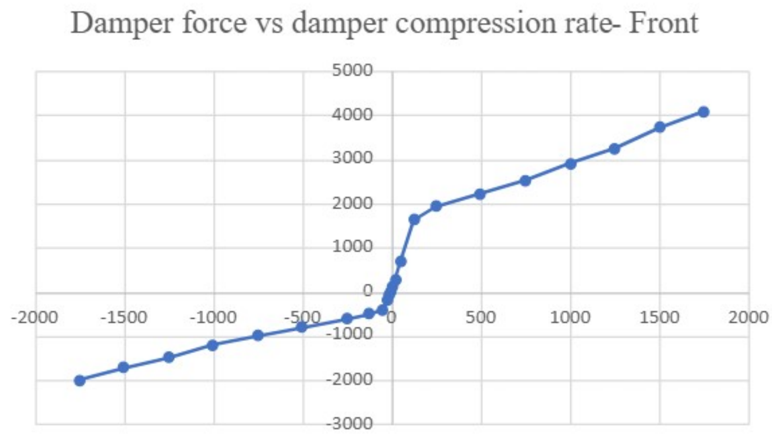

(a) Front axle.

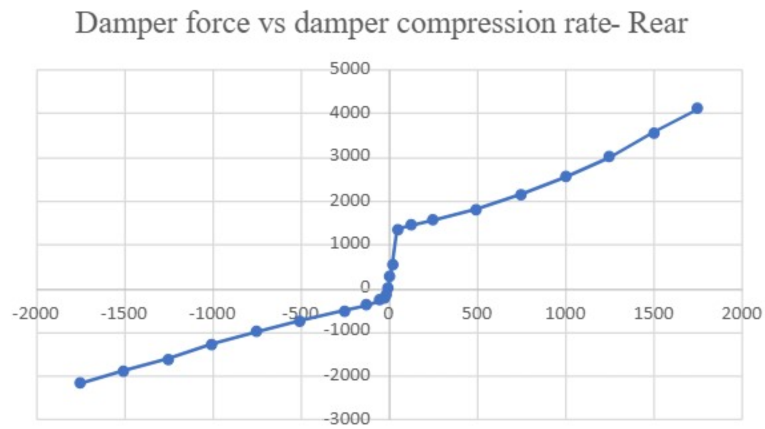

(b) Rear axle.

Figure 3.11: Damper force versus damper compression rate for the front and rear axles.

It is important to note that, in the CarSim interface, the spring and damper curves are defined with respect to the motion of the elastic and damping elements, rather than directly to the wheel motion. For this reason, the ratios *Spring position/Suspension position* and *Damper motion/wheel motion* are introduced to convert the wheel jounce into the corresponding spring compression and damper stroke. For completeness, the numerical values of the scaling ratios are reported below.

$$\left(\frac{\text{Spring position}}{\text{Suspension position}}\right)_{\text{front}} = 0.63$$

$$\left(\frac{\text{Spring position}}{\text{Suspension position}}\right)_{\text{rear}} = 0.68$$

$$\left(\frac{\text{Damper motion}}{\text{Wheel motion}}\right)_{\text{front}} = 0.63$$

$$\left(\frac{\text{Damper motion}}{\text{Wheel motion}}\right)_{\text{rear}} = 0.82$$

To conclude the description of the methodology adopted for the characterization of the model, it is important to describe the main quantities defined in the last CarSim section, namely the *Tires* section.

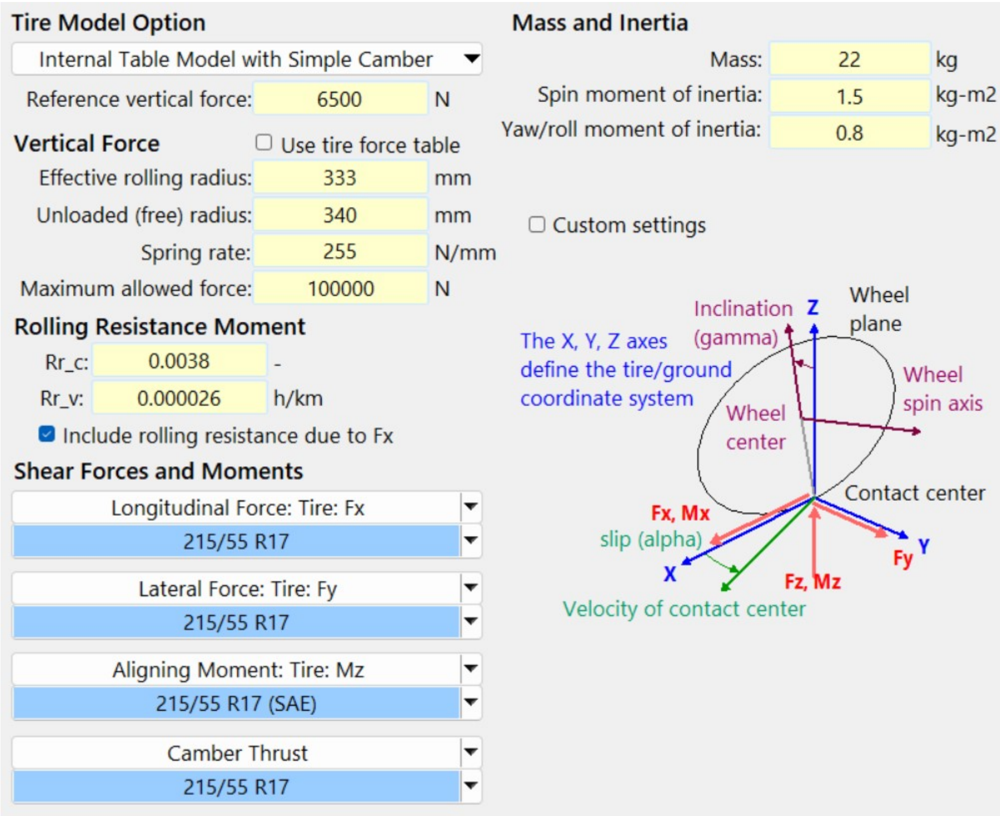

Figure 3.12: Main parameters defined in the CarSim Tires section.

The *Tires* section of CarSim is organized in a few main areas, within which only the parameters that are relevant for the present application are specified:

- *Tire model option*: selection of the internal table model with simple camber, which provides nonlinear force and moment characteristics based on tabulated data for the chosen tire size.
- *Mass and inertia*: definition of the tire mass and of the spin and yaw/roll moments of inertia, ensuring a consistent representation of the wheel–tire rotational dynamics with respect to the unsprung mass properties used in the suspension models.
- *Vertical force*: specification of the reference vertical load, effective rolling radius, unloaded radius and vertical spring rate, parameters that govern the radial stiffness of the tire and the evolution of the vertical force as a function of vertical deflection.
- *Rolling resistance moment*: introduction of a constant rolling resistance coefficient and of a speed-dependent term, so that the principal energy losses associated with tire rolling are taken into account in the longitudinal dynamics.
- *Shear forces and moments*: selection of the datasets used to compute longitudinal force, lateral force, aligning moment and camber thrust for the specified tire size, which define the longitudinal and lateral behaviour of the tire under combined slip conditions.

3.1.3 Definition of inputs, outputs and test maneuvers

Once the vehicle model has been fully characterized in CarSim, the next step consists in defining the input and output variables of interest and in introducing the driving maneuvers that will be used to excite the system during the simulations. In this work, particular attention is paid to the selection of the inputs as well as to the corresponding measured outputs, that are relevant for the subsequent analysis of vehicle dynamics and comfort.

The selected inputs and outputs are then used in the Simulink environment to carry out the simulations and to evaluate the vehicle response for the different maneuvers and road profiles. CarSim operates in co-simulation with Simulink: in particular, CarSim provides the nonlinear vehicle dynamics model, whereas Simulink handles the high-level control logic and the processing of the simulation data. In this framework, Simulink generates the input signals and records the relevant output variables, while CarSim focuses on the detailed computation of the vehicle behaviour.

Among the various **input channels** available in CarSim, two additional signals are imported from Simulink: the compressive force generated by the dampers and the vertical position of the ground at each tire contact patch.

Variables Activated for Import

	Name	Mode	Initial Value
1	IMP_FD_L1	Add	0
2	IMP_FD_R1	Add	0
3	IMP_FD_L2	Add	0
4	IMP_FD_R2	Add	0
5	IMP_ZGND_L1	Replace	0.0
6	IMP_ZGND_L2	Replace	0.0
7	IMP_ZGND_R1	Replace	0.0
8	IMP_ZGND_R2	Replace	0.0

Figure 3.13: Input variables activated for import in CarSim.

In particular, it is possible to explain the meaning of the two inputs:

- *Compressive force from the dampers*: four channels (front/rear and left/right) used to impose in CarSim the force delivered by the semi-active dampers computed in Simulink.

- *Z-coordinate of ground at the tire CTC*: four channels providing the road vertical profile at each tire contact center, which allow different road excitations to be applied to the vehicle model.

As far as the road excitation is concerned, the Simulink block that generates the road profile was directly provided as an input to this work and is applied to all four wheels of the vehicle model. The block includes two types of profiles: a *bump road profile* and a *random road profile* based on ISO 8608 classifications. For the random case, two different roughness levels are available, namely ISO B and ISO C, which are selected according to the value of the road roughness parameter G_r:

$$G_r = 6.4 \times 10^{-7} \;\Rightarrow\; \text{ISO B}$$

$$G_r = 2.56 \times 10^{-6} \;\Rightarrow\; \text{ISO C}$$

The graphical representation of the two road profiles within the Simulink environment is reported below.

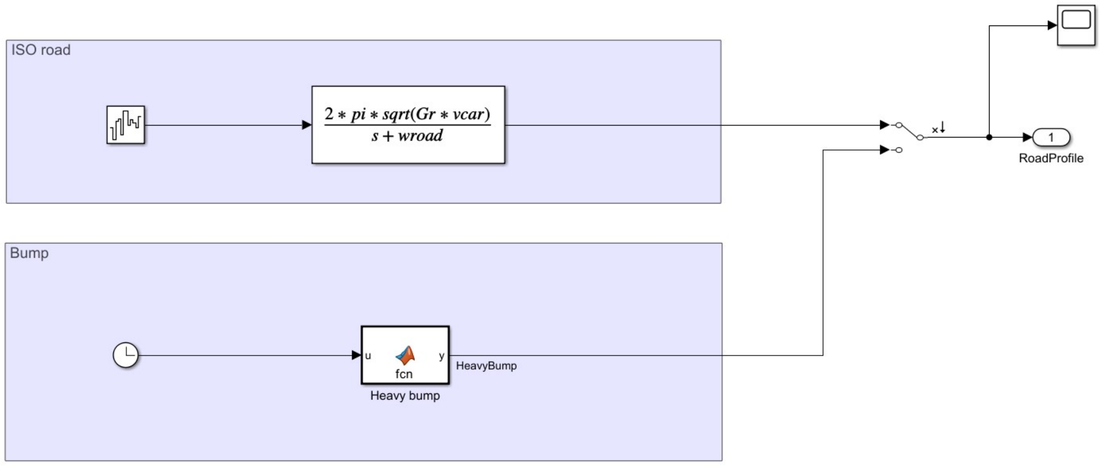

Figure 3.14: Graphical representation of the bump and random road profiles implemented in the Simulink environment.

Concerning the damper compressive forces, in the first stage these signals are computed directly within CarSim starting from the force–velocity characteristics used to model the damper behaviour as a function of its compression rate. In Simulink, it is therefore sufficient to introduce an input port block that imports the forces generated by the CarSim damper model. In a second step, these forces are progressively replaced by external control forces obtained through a negative-feedback strategy, on top of which additional semi-active control laws (such as Skyhook and Groundhook) are implemented.

After defining the input channels and their connection between CarSim and Simulink, the focus shifts to the selection of the **output variables** to be exported from the vehicle model. A large number of signals is available, but in this work only a subset is considered and subsequently grouped according to the type of vehicle dynamics under investigation, namely vertical (ride) and lateral (handling) dynamics.
For the analysis of the *vertical dynamics*, the following output variables are exported from CarSim to Simulink and grouped according to their main physical meaning.

- *Vertical acceleration of CG sprung mass* ($a_{z,\mathrm{SM}}$): vertical acceleration at the vehicle sprung-mass centre of gravity, used as the main indicator of ride comfort.

- *Z-coordinate of CG sprung mass* ($z_{CG,\mathrm{SM}}$): vertical displacement of the sprung-mass centre of gravity, describing the global heave motion of the vehicle body.

- *Z-coordinate of wheel center* ($z_{WC,L1}$, $z_{WC,L2}$): vertical position of the left wheel centres on the front and rear axles, used to monitor the suspension travel and the relative motion between wheels and body on the left side of the vehicle.

- *Compression of damper* ($s_{D,L1}$, $s_{D,L2}$): damper compression at the front-left and rear-left corners, providing information on the working range of the semi-active dampers and on the effectiveness of the control strategies.

- *Pitch angle of the vehicle* (θ): global pitch rotation of the vehicle body, associated with longitudinal load transfer during braking and acceleration over uneven roads.

- *Pitch acceleration of the vehicle* ($\ddot{\theta}$): angular acceleration about the pitch axis, used to characterize the dynamic response of the vehicle in terms of fore–aft body motion.

- *Vertical tire forces* ($F_{z,L1}$, $F_{z,L2}$): vertical forces at the front-left and rear-left tire contact patches, employed to assess road holding and to relate body motion and suspension travel to the load distribution on the tires.

For the analysis of the *lateral dynamics*, instead, the following output variables are considered and grouped according to their main physical meaning:

- *Lateral acceleration of the sprung-mass centre of gravity* ($a_{y,\mathrm{SM}}$): Serves as the primary indicator of the lateral excitation acting on the vehicle body, influencing both handling dynamics and passenger comfort.

- *Roll angle of the vehicle body* (ϕ): Represents the macroscopic chassis rotation, which directly dictates the lateral load transfer and the overall cornering behaviour.

- *Roll acceleration of the vehicle body* ($\ddot{\phi}$): Measures how quickly the roll angle of the vehicle body changes over time, that is, how fast the body starts or stops rolling around its longitudinal axis during cornering.

- *Lateral tire forces* ($F_{y,L2}$, $F_{y,R2}$): Evaluate the cornering forces generated at the contact patches, essential for assessing the utilization of available tire grip and vehicle stability.

The main output variables selected for the analysis of the vertical and lateral dynamics are summarized in Table 3.2 and Table 3.3..

Symbol	Description	Unit
$a_{z,\mathrm{SM}}$	Vertical acceleration of sprung-mass CG	g
$z_{CG,\mathrm{SM}}$	Vertical position of sprung-mass CG	m
$z_{W,L1}$, $z_{W,L2}$	Vertical position of wheel centres L1 and L2	m
$s_{D,L1}$, $s_{D,L2}$	Damper compression at corners L1 and L2	mm
θ	Pitch angle of vehicle body	deg
$\ddot{\theta}$	Pitch angular acceleration	rad/s^2
$F_{z,L1}$, $F_{z,L2}$	Vertical tire forces at corners L1 and L2	N

Table 3.2: Output variables used for the analysis of vertical dynamics.

Symbol	Description	Unit
$a_{y,\mathrm{SM}}$	Lateral acceleration of sprung-mass CG	g
ϕ	Roll angle of vehicle body	deg
$\ddot{\phi}$	Roll acceleration of vehicle body	rad/s^2
$F_{y,L2}$, $F_{y,R2}$	Lateral tire forces at corners L2 and R2	N

Table 3.3: Output variables used for the analysis of lateral dynamics.

To conclude, different test maneuvers are considered in order to exercise both the vertical and the lateral dynamics of the vehicle model. A brief classification of the maneuvers used in the following is reported below:

- *Vertical dynamics (comfort)*: maneuvers primarily aimed at exciting the vertical motion of the sprung and unsprung masses, such as driving on uneven road profiles or speed bumps road inputs.
- *Lateral dynamics (handling)*: maneuvers mainly devoted to the assessment of lateral stability and handling behaviour, such as step steer, sine wave or lane change tests.

A detailed description of the implementation and purpose of each maneuver is provided in the next subsection for the validation of the vehicle model.

3.2 Vehicle model testing

The testing of the vehicle model is carried out by means of a set of simulations combining different road profiles and driving maneuvers. The objective is to assess whether the CarSim–Simulink model is able to reproduce the expected behaviour of the real vehicle in terms of both vertical (ride) and lateral (handling) dynamics.

3.2.1 Road profiles analysis

First, the road excitation is defined by means of the bump and random road profiles introduced in Section 3.1.3. These profiles are applied to all four wheels and are used consistently across the validation maneuvers in order to excite the relevant dynamic modes of the vehicle.

Bump road profile

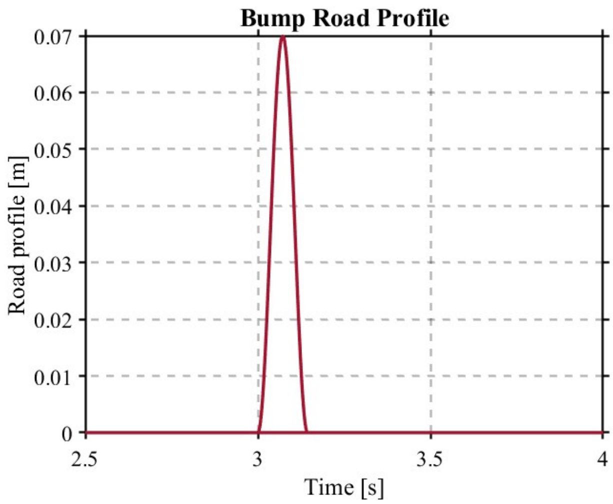

Figure 3.15: Bump road profile implemented in the Simulink environment.

The first road excitation considered is a bump road profile, consisting of a single localized elevation of the road surface. This type of profile is commonly used to strongly excite the vertical dynamics of the vehicle and to analyze the transient response of both the suspension system and the sprung mass when crossing a discrete obstacle. Specifically, it allows for the evaluation of critical performance metrics, such as impact absorption capabilities, maximum suspension stroke and the settling time required to restore the vehicle's steady-state equilibrium.

In the present work, the bump is modelled as a short-duration pulse in the road elevation with a peak amplitude of about 7×10^{-2} m, as shown in Figure 3.15. This specific geometry ensures that the vehicle experiences a pronounced but isolated vertical disturbance, forcing the shock absorbers to rapidly dissipate a sudden injection of kinetic energy, thereby highlighting the overall damping efficiency of the system.

ISO B - ISO C road profiles

According to the ISO 8608 standard, road surface irregularities are modeled as stationary random processes and characterized by the Power Spectral Density (PSD), denoted as $\bar{S}(\varpi)$. This function describes the vertical road displacement variance in relation to the spatial frequency ϖ (cycles/m). Since spatial frequency is the inverse of the spatial wavelength ($\lambda = 1/\varpi$), the PSD effectively illustrates how the road's energy is distributed across different wavelengths, providing a compact description of the road roughness. This distinction is crucial in vehicle dynamics, as long wavelengths primarily affect sprung mass kinematics (ride comfort), while short wavelengths strongly excite the unsprung masses (tire grip).

The spectrum is mathematically described by the power law:

$$\bar{S}(\varpi) = G_r \, \varpi^{-n}$$

where G_r represents the roughness coefficient associated with a specific road class, and n is the waviness exponent. In the standard ISO 8608 formulation, this exponent is conventionally set to $n = 2$, reflecting the physical tendency of road profiles to exhibit much larger displacement amplitudes at lower spatial frequencies compared to high-frequency surface texturing.

Furthermore, the standard categorizes road severities into distinct classes (from Class A to Class H), each defined by a specific range of G_r. Lower values indicate smooth surfaces, such as well-maintained highways (Class A or B). Conversely, higher values describe severely degraded or unpaved profiles (Classes C to H), characterized by massive elevation variations at all wavelengths, which impose substantially higher dynamic demands on the vehicle's suspension system.

Class	$G_{r,\min}$ [m^{2}cycles/m]	$G_{r,\text{mean}}$ [m^{2}cycles/m]	$G_{r,\max}$ [m^{2}cycles/m]
A	–	1.6×10^{-6}	3.2×10^{-6}
B	3.2×10^{-7}	6.4×10^{-7}	1.28×10^{-6}
C	1.28×10^{-6}	2.56×10^{-6}	5.12×10^{-6}
D	5.12×10^{-6}	1.024×10^{-5}	2.048×10^{-5}
E	2.048×10^{-5}	4.096×10^{-5}	8.192×10^{-5}
F	8.192×10^{-5}	1.6384×10^{-4}	3.2768×10^{-4}
G	3.2768×10^{-4}	6.5536×10^{-4}	1.31072×10^{-3}
H	1.31072×10^{-3}	2.62144×10^{-3}	–

Table 3.4: Minimum, mean and maximum values of the roughness coefficient G_r for the ISO 8608 road classes. The study cases considered in this work correspond to classes ***B*** and ***C***.

In the following, the plots related to the road classes *ISO B* and *ISO C* under investigation are reported, together with a brief description of the trends.

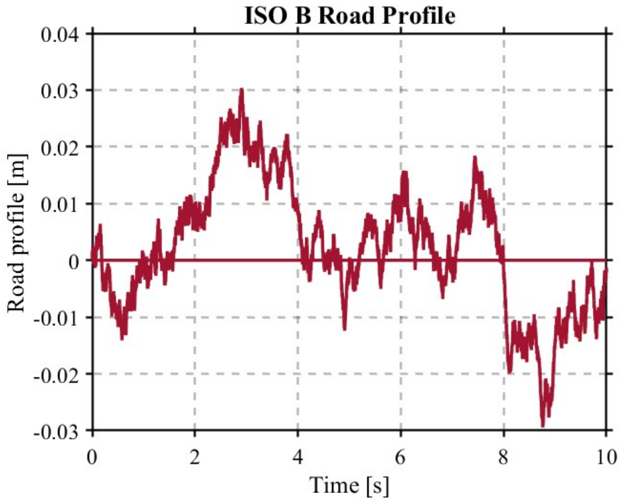

Figure 3.16: ISO class B road profile.

The ISO class B road profile shows a stochastic elevation signal fluctuating around the zero level, with moderate positive peaks up to about $+0.03\,\mathrm{m}$ and negative troughs down to approximately $-0.025\,\mathrm{m}$ over the 10 s time interval.

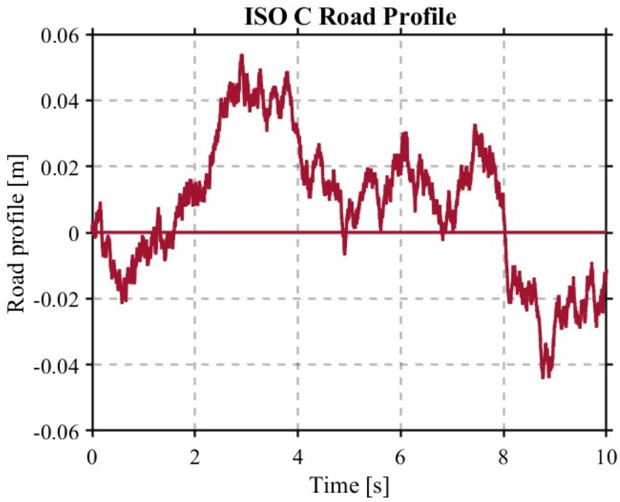

Figure 3.17: ISO class C road profile.

The ISO class C road profile exhibits a rough stochastic elevation signal fluctuating around the zero level, with higher positive peaks up to about $+0.05\,\mathrm{m}$ and deeper negative troughs down to approximately $-0.045\,\mathrm{m}$ over the 10 s time interval.
To conclude this section, the plot comparing the trends of the ISO class B and C road profiles is also reported, in order to highlight the different roughness levels of

the two surfaces.

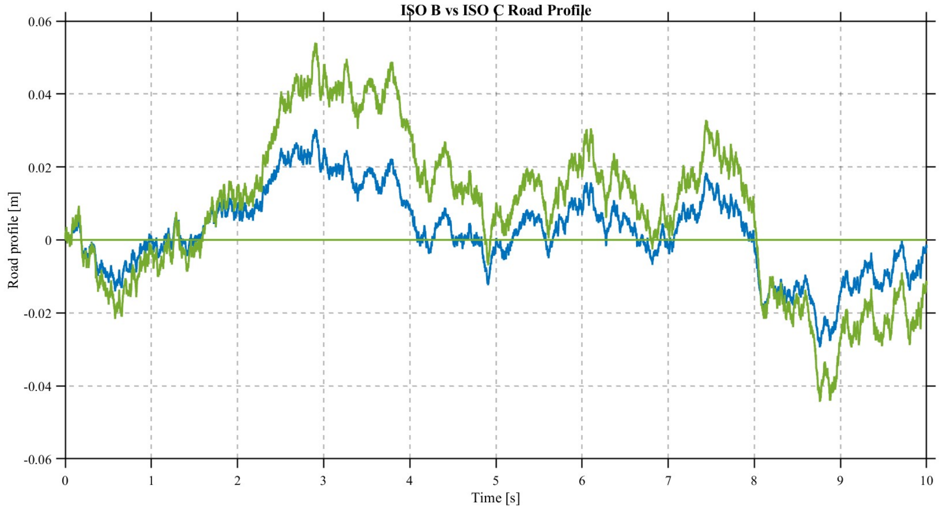

Figure 3.18: ISO class B vs ISO class C road profiles.

3.2.2 Vehicle dynamics response for selected manoeuvres on different road profiles

In the following section, the vehicle behaviour during selected manoeuvres is analyzed over different road profiles, focusing on the three different surfaces introduced above. Moreover, it is worth pointing out that each manoeuvre is carried out at an appropriate constant vehicle speed, selected according to the manufacturer data.

***Vertical dynamics*: Constant target speed 30 km/h - Bump road profile**

In this manoeuvre, the vehicle travels in a straight line over the bump road profile at a constant target speed of 30 km/h. This condition represents a typical low-speed transient excitation, where the road elevation is characterised by a single, localised irregularity superimposed on an otherwise flat surface.

The vertical response of the vehicle is evaluated by inspecting the outputs of the vertical dynamics discussed in Section 3.1.3.

The corresponding plots of the main quantities, together with a brief explanation of the trend of each graph, are reported in the following.

The first set of plots, which refers to the *chassis motion*, reports the time histories of the ***sprung mass centre-of-gravity vertical acceleration*** and ***displacement*** for the bump manoeuvre. These quantities describe how the vehicle body moves in the vertical direction when crossing the bump and are therefore directly linked to the ride comfort perceived by the occupants.

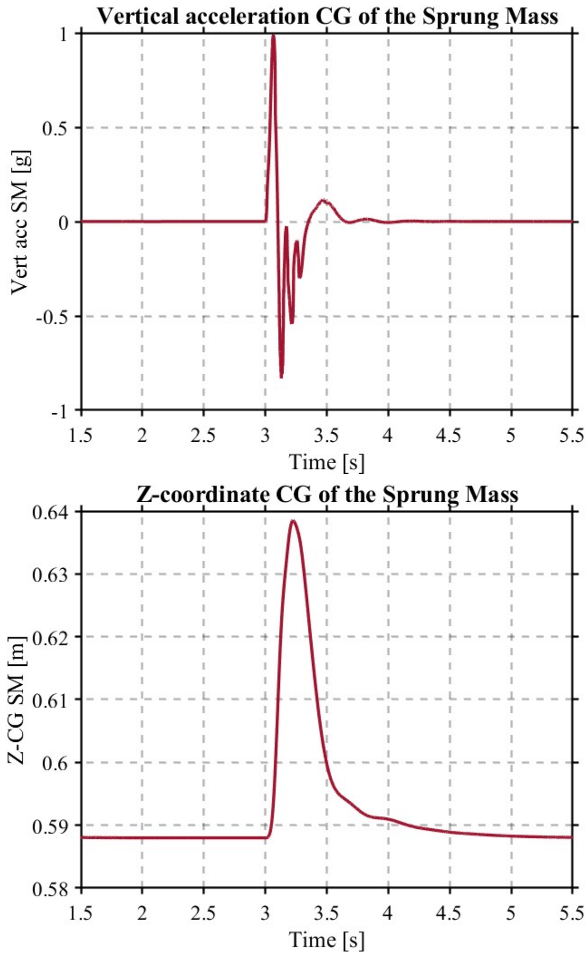

Figure 3.19: Chassis motion for the bump road profile manoeuvre: sprung mass CG vertical acceleration (top) and vertical displacement (bottom).

The plots in Figure 3.19 can be interpreted as follows:

- *Vertical acceleration CG of the sprung mass*: at the bump crossing, the acceleration signal shows a sharp positive peak of about $+1$ g followed by a negative peak close to -0.8 g, reflecting the rapid upward and downward motion of the vehicle body. Afterwards, the oscillations quickly decay and the acceleration returns to values close to zero, showing that the suspension efficiently damps the transient vertical vibrations.

- *Z-coordinate CG of the sprung mass*: the vertical displacement of the sprung mass CG exhibits a single pronounced upward excursion, reaching approximately 0.64 m, and then gradually converges back to the initial level of about 0.59 m, confirming that the bump induces a transient vertical motion without a permanent change in ride height.

The second set of plots also belongs to the *chassis motion* category and reports the time histories of the ***pitch angle*** and ***pitch acceleration*** of the vehicle for the bump manoeuvre.

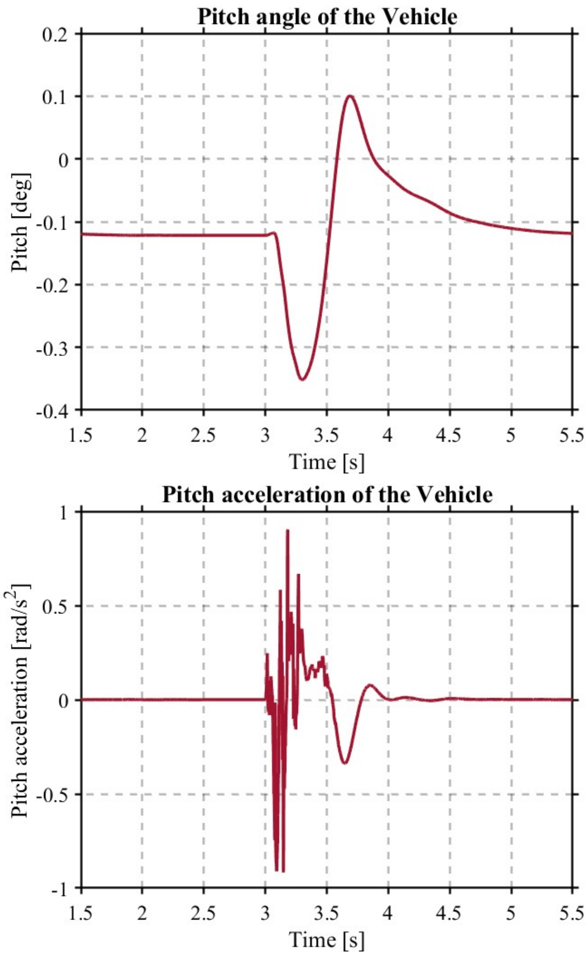

Figure 3.20: Chassis motion for the bump road profile manoeuvre: vehicle pitch angle (top) and pitch acceleration (bottom).

The plots in Figure 3.20 can be interpreted as follows:

- *Pitch angle of the vehicle*: the bump excitation produces a transient pitch motion, with the body first rotating backward and then forward before gradually returning to the nominal position.

- *Pitch acceleration of the vehicle*: the corresponding pitch acceleration signal exhibits a sharp positive and negative peak at the bump crossing, followed by damped oscillations that rapidly decay.

Focusing on the vertical behaviour of the unsprung masses, the next group of plots refers to the *wheels motion* and reports the time histories of the ***vertical acceleration*** and ***displacement*** of the *Front-left* and *Rear-left* wheels for the bump manoeuvre, in order to highlight the different behaviour of the front and rear axles.

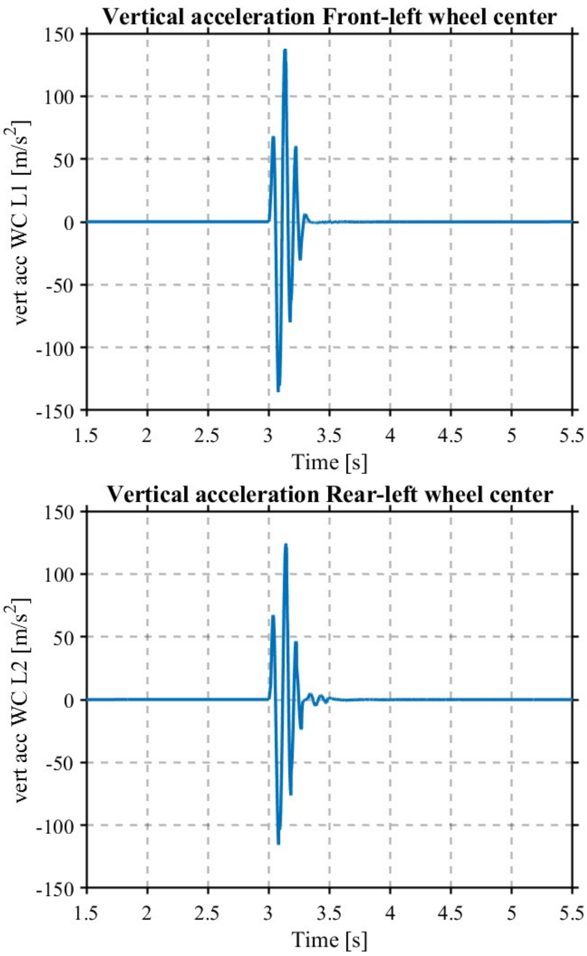

Figure 3.21: Comparison of vertical acceleration for the front-left (top) and rear-left (bottom) wheels during the bump manoeuvre.

The plots in Figure 3.21 compare the vertical acceleration at the wheel centre of the *front-left* (FL) and *rear-left* (RL) wheels during the bump manoeuvre. In both cases, the signal exhibits a sharp positive and negative peak at the bump crossing, followed by damped oscillations that quickly vanish, indicating a transient excitation of the unsprung masses.

The peak values are slightly higher for the front-left wheel, while the rear-left wheel shows a marginally smoother response. This difference can be related to the 45%–55% front–rear mass distribution of the vehicle and to the different suspension characteristics adopted on the two axles.

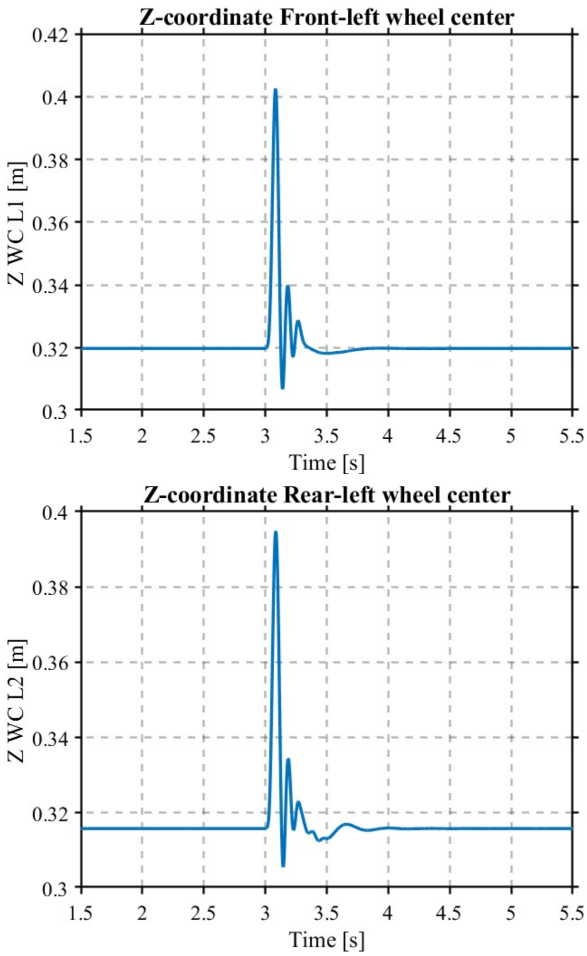

Figure 3.22: Comparison of vertical displacement for the front-left (top) and rear-left (bottom) wheels during the bump manoeuvre.

The plots in Figure 3.22 compare the vertical displacement (Z–coordinate) of the *front-left* (FL) and *rear-left* (RL) wheel centres during the bump manoeuvre. In both cases, the wheel centre moves upwards when crossing the bump, reaching a clear peak, and then gradually returns to the initial position, confirming that the road irregularity induces a transient vertical motion without permanent changes in ride height.

The maximum vertical displacement of the front-left wheel is slightly higher than that of the rear-left wheel, while the rear axle exhibits a marginally smoother decay of the oscillations. As said in the previous analysis of the acceleration, this difference is consistent with the 45%–55% front–rear mass distribution of the vehicle and the distinct suspension characteristics adopted on the two axles.

Going on with the analysis, we find the group of plots that refers to the *suspensions motion*. This category focuses on the ***compression of the dampers*** associated with the *front-left* (FL) and *rear-left* (RL) wheels during the bump manoeuvre. These quantities describe how the suspension elements deform in the vertical direction when the wheels are excited by the road irregularity.

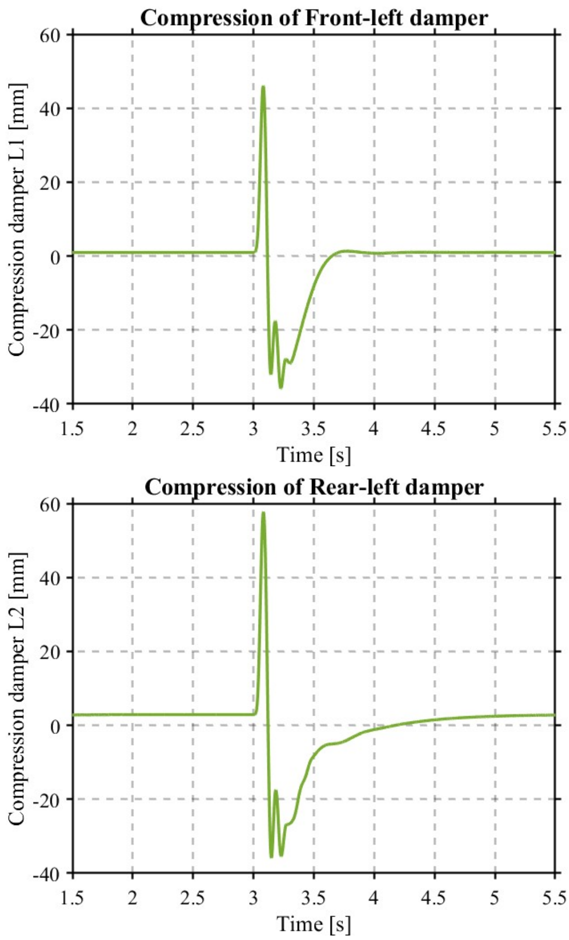

Figure 3.23: Comparison of damper compression for the front-left (top) and rear-left (bottom) suspension during the bump manoeuvre

In both cases, the road input generates a sharp transient compression followed

by a negative excursion and a gradual return to the nominal value, highlighting the ability of the suspension to absorb and dissipate the vertical excitation. The rear-left damper reaches a slightly higher peak compression and exhibits a smoother recovery than the front-left one.
Finally, the last group of plots refers to the *tires motion* and focuses on the ***vertical forces*** generated at the contact patch of the *front-left* and *rear-left* tires during the bump manoeuvre.

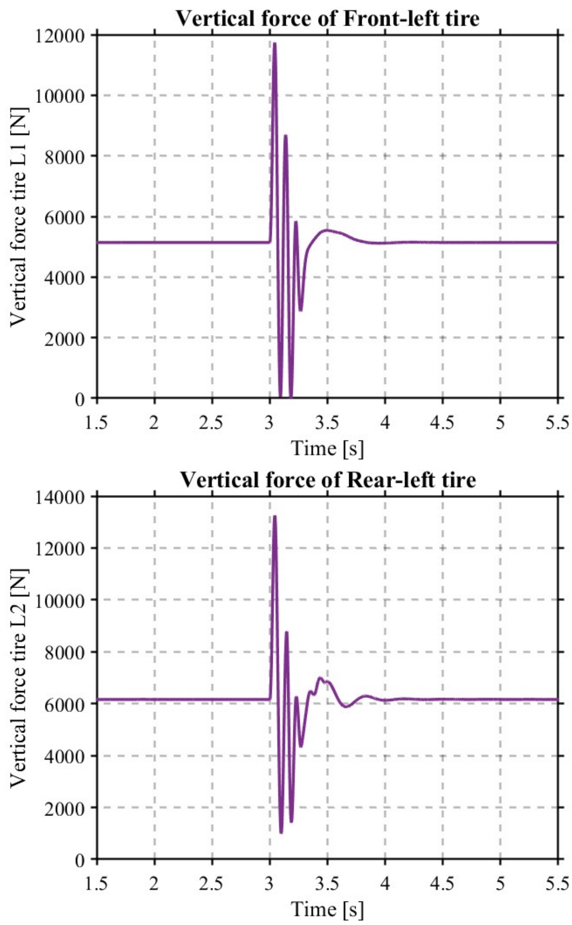

Figure 3.24: Vertical forces of the front-left (top) and rear-left (bottom) tires during the bump manoeuvre.

The road excitation produces a pronounced transient variation of the normal load on both wheels, with different peak values and oscillation patterns that reflect the front–rear load distribution and the interaction between tires and suspension. After the initial disturbance, the vertical forces quickly settle back close to their static values, showing that the bump manoeuvre does not drive the tires near saturation.

Vertical Dynamics: ISO B (70 km/h) vs. ISO C (35 km/h)

This section adopts a comparative approach to analyze the vehicle behavior across the two road profiles at different speeds: a standard ISO B surface at 70 km/h and a degraded ISO C track at 35 km/h. The following analysis shows that, despite the halved speed, the rougher pavement still imposes higher dynamic demands on chassis, wheels, suspensions and tires.

Starting with the *chassis motion* analysis, the relevant plots are reported below.

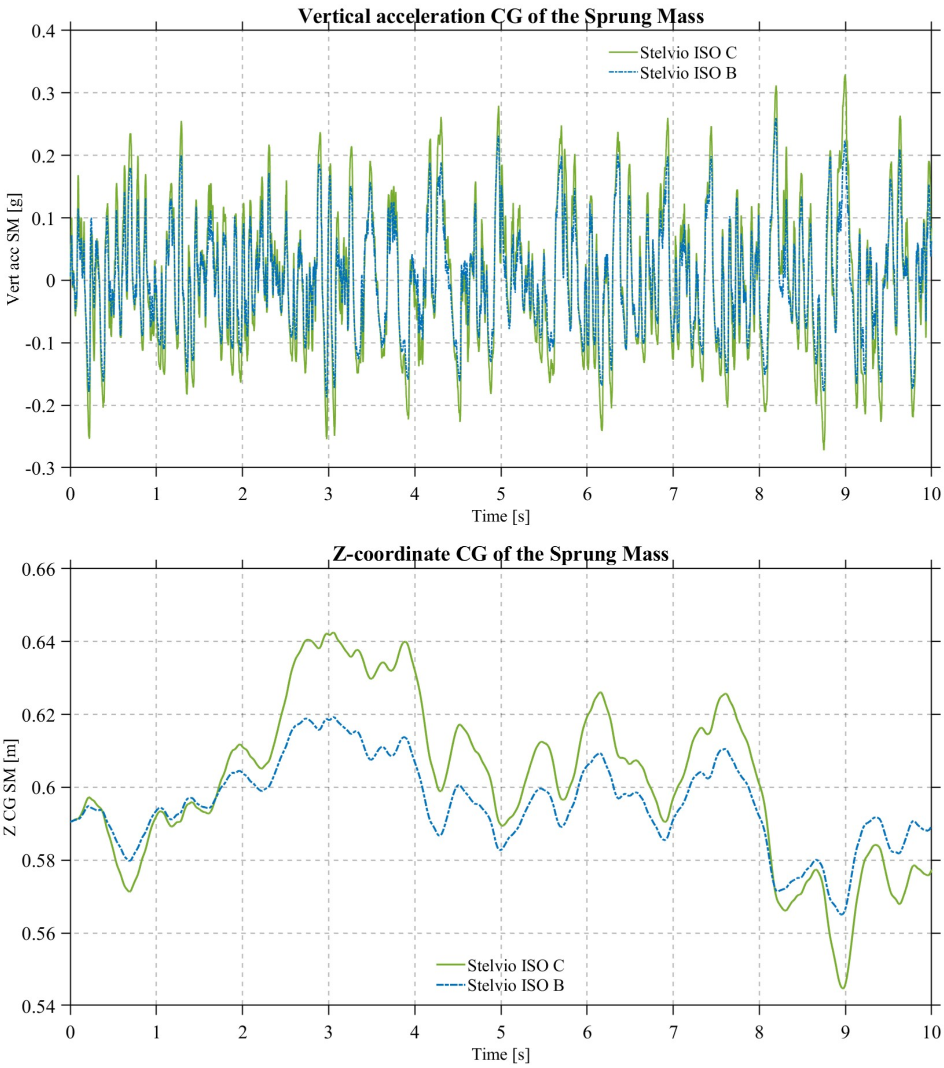

Figure 3.25: ISO C vs ISO B road profile: Vertical acceleration of the sprung mass (top) and Vertical displacement of the sprung mass (bottom).

The plots in Figure 3.25 can be interpreted as follows:

- *Vertical acceleration of the sprung mass*: The ISO C profile clearly degrades ride comfort by generating harsh peaks exceeding ±0.3 g, whereas the smoother ISO B baseline confines vibrations mostly within ±0.2 g.

- *Vertical displacement of the vehicle body CG*: Oscillating around a 0.59 m static equilibrium, the chassis experiences wider heave excursions on the ISO C surface (ranging from 0.54 m to 0.64 m). This indicates a higher suspension workload compared to the tighter movements on the ISO B profile.

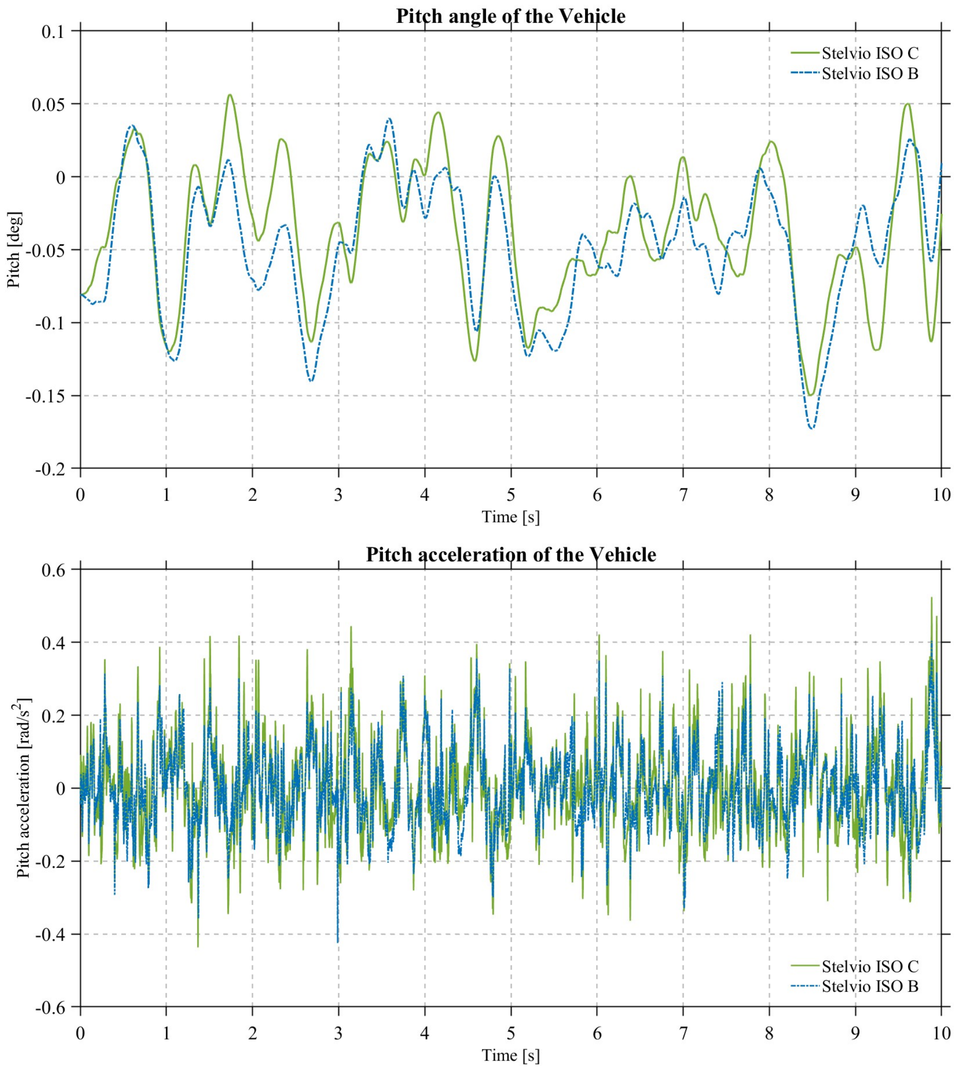

Figure 3.26: ISO C vs ISO B road profile: Pitch angle (top) and Pitch acceleration (bottom) of the vehicle body.

The pitch motion plots can be interpreted as follows:

- *Pitch angle of the vehicle*: Both profiles induce macroscopic pitch motions ranging between -0.17° and +0.05°. Due to the reduced vehicle speed, the ISO C amplitude matches the baseline, though its curve exhibits noticeably more irregular variations.
- *Pitch acceleration of the vehicle*: The severe ISO C profile amplifies rotational vibrations, generating sharp peaks that reach ±0.4 rad/s^2. In contrast, the ISO B baseline confines these accelerations mostly within ±0.3 rad/s^2.

Regarding the *wheels motion* category, the analysis starts from the following plots:

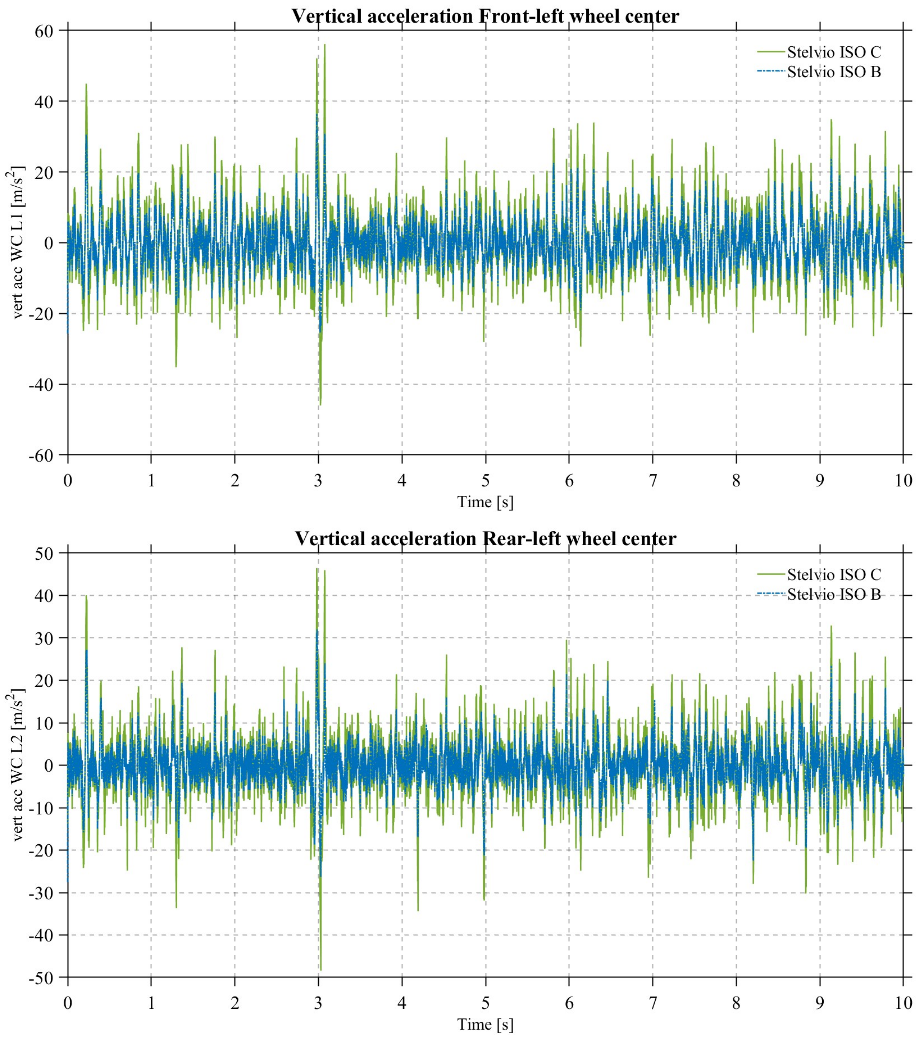

Figure 3.27: ISO C vs ISO B road profile: Vertical acceleration of the front-left (top) and rear-left (bottom) wheel centre.

The comparison of the *wheel centre vertical accelerations* highlights the severe impact of the ISO C profile on the unsprung masses. On this rougher surface, the front-left wheel experiences extreme peaks approaching ± 60 m/s^2, while the rear-left reaches ± 50 m/s^2. Conversely, the ISO B baseline confines vibrations for both wheels mostly within a ± 20 m/s^2 range. This massive amplification indicates that the tires are subjected to significantly higher dynamic loads. Consequently, despite the reduced speed, the degraded pavement compromises continuous tire-road contact, directly penalizing the vehicle's road holding.

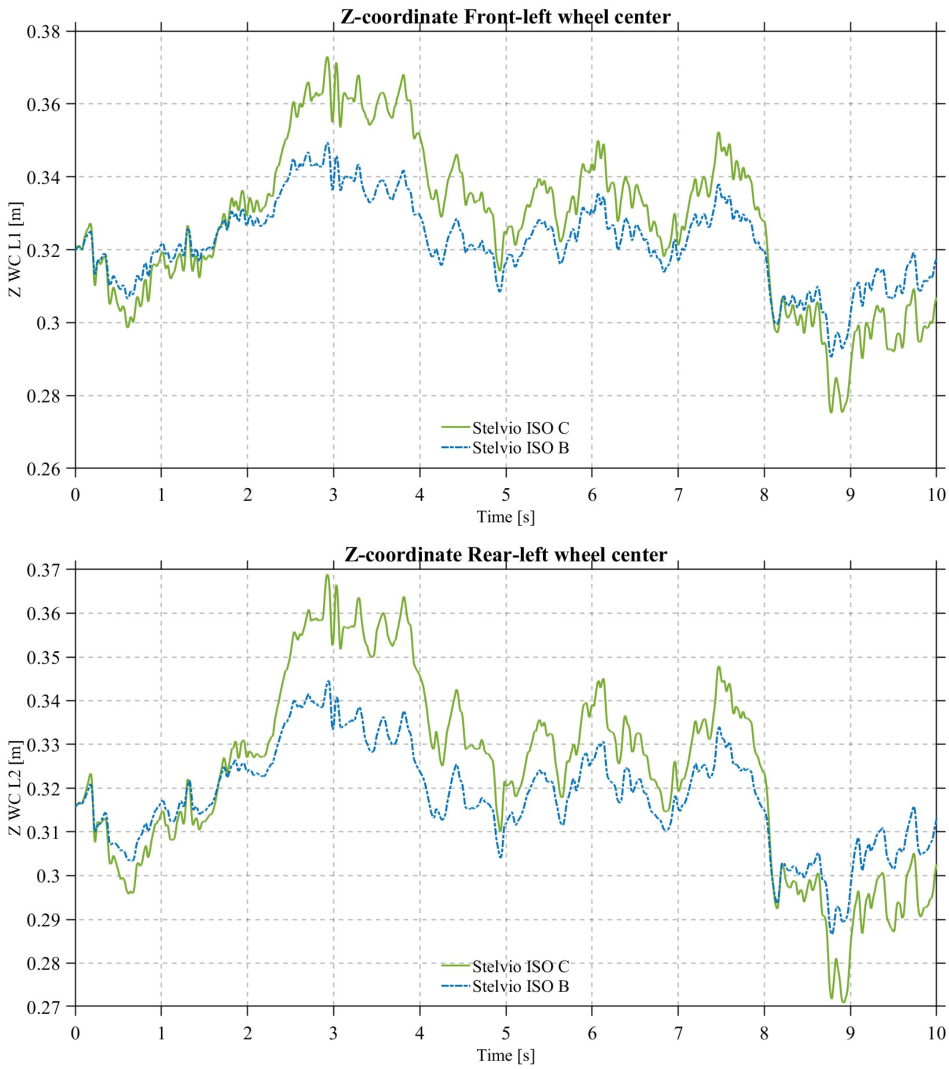

Figure 3.28: ISO C vs ISO B road profile: Vertical displacement of the front-left (top) and rear-left (bottom) wheel centre.

The *wheel centre vertical displacements* plots highlight the unsprung mass kinematics. Oscillating around a 0.32 m static equilibrium, both wheels experience pronounced excursions on the ISO C profile, fluctuating between 0.275 m and 0.375 m (front-left), and 0.27 m to 0.37 m (rear-left). Conversely, the smoother ISO B baseline tightly bounds these movements. This amplified travel demonstrates a significantly higher demand on the suspension's working space to absorb the degraded pavement.

The third class of our analysis, namely the *suspensions motion*, is characterized by the following plots:

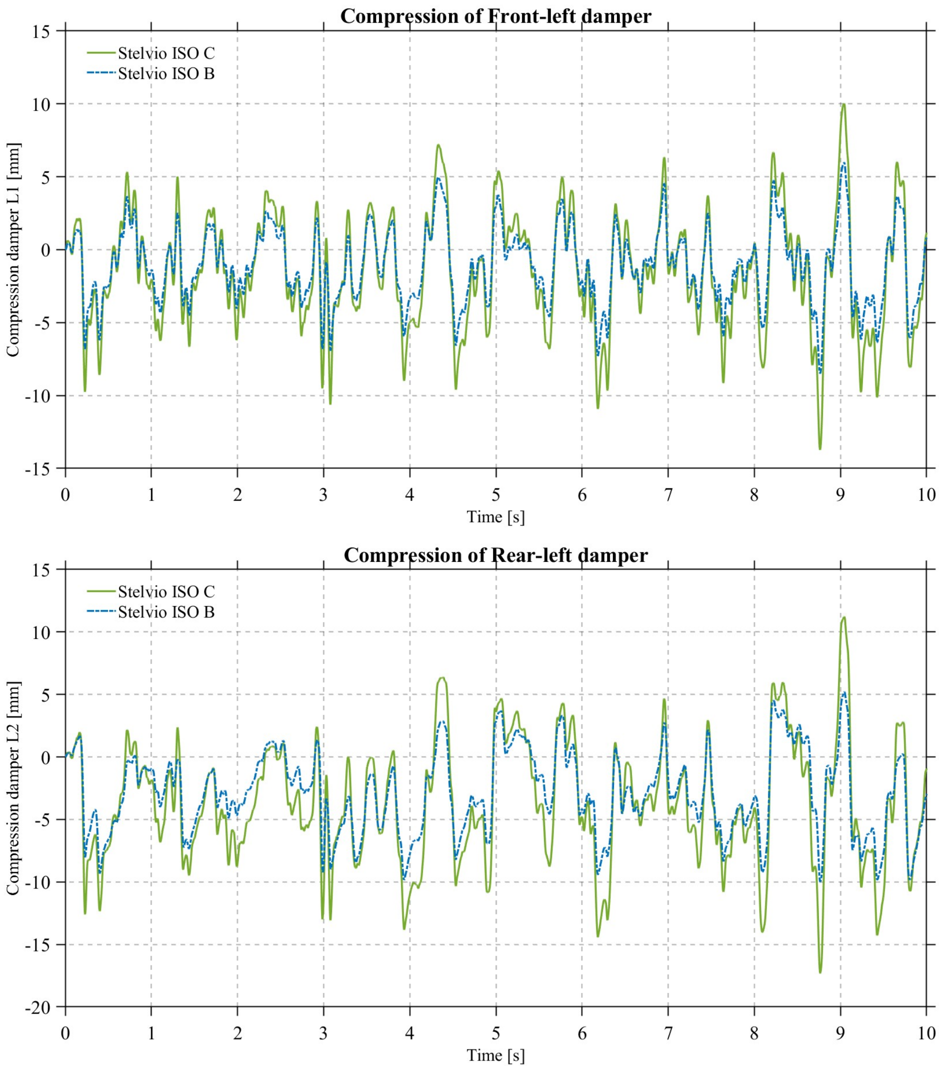

Figure 3.29: ISO C vs ISO B road profile: Compression of the front-left (top) and rear-left (bottom) damper.

The *damper compressions* plots illustrate the dynamic stroke of the suspension system. On the severe ISO C profile, the damper travel widens significantly, fluctuating between −14 mm and +10 mm (front-left), and from −17 mm to +11 mm (rear-left). Conversely, the smoother ISO B baseline tightly bounds these deformations within a narrower −10 mm to +6 mm range. This amplified travel confirms the increased stroke demand and energy dissipation required to the suspensions to filter the severe road irregularities.

To conclude, the *tires motion* category is analyzed by presenting the plots reported below.

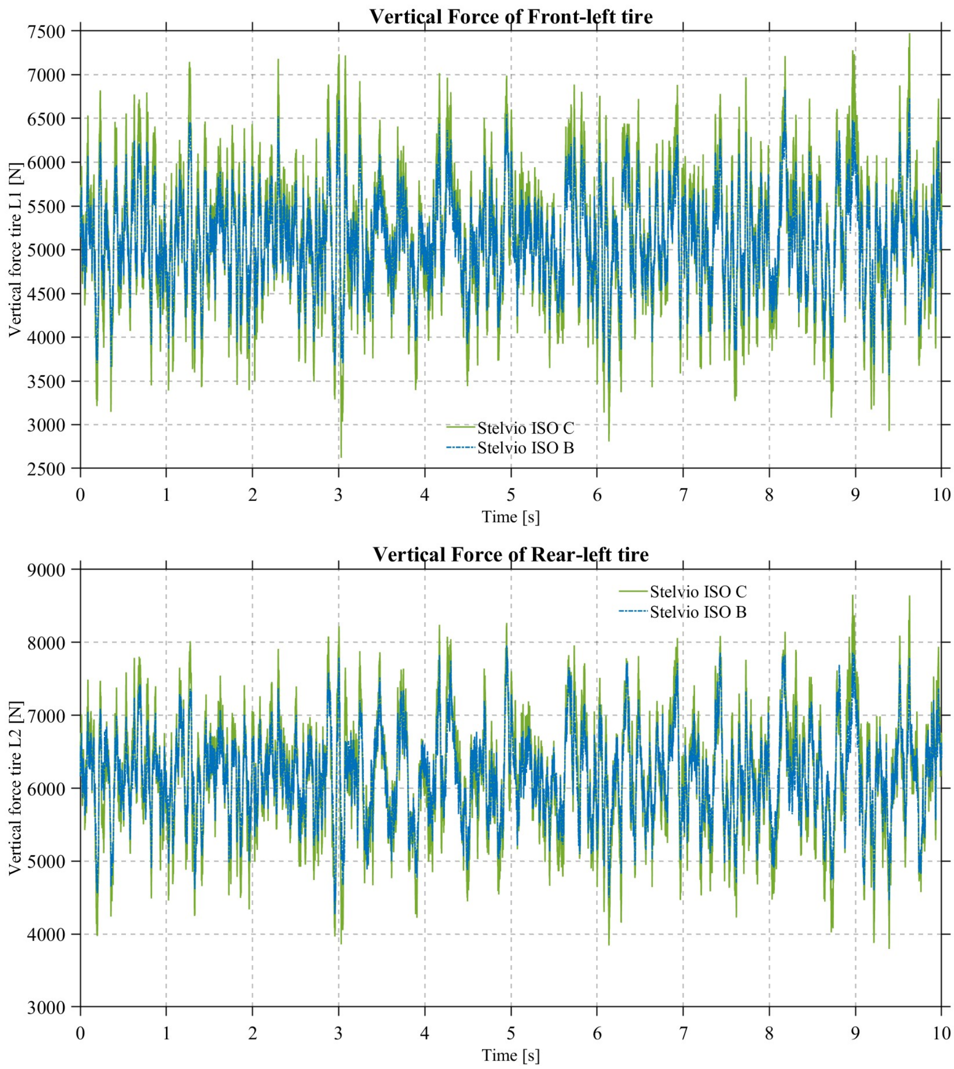

Figure 3.30: ISO C vs ISO B road profile: Vertical force of the front-left (top) and rear-left (bottom) tire.

The *vertical tire forces* plots highlight the dynamic load variations at the contact patch, which strictly govern the vehicle's road holding capabilities. On the severe ISO C profile, normal loads experience extreme fluctuations, ranging from 2600 N to 7500 N (front-left) and from 3800 N to 8700 N (rear-left). Conversely, the smoother ISO B baseline effectively confines these force variations within much tighter operational bands. This drastic amplification in dynamic load oscillations on the degraded pavement directly translates to a significant loss of instantaneous tire grip, perfectly confirming the severe handling degradation induced by the macroscopic road irregularities.

***Lateral dynamics*: Sine wave steering 10°, 0.25 Hz - 50 km/h**

The first lateral excitation considered is a sine wave steering maneuver, performed at a constant vehicle speed of 50 km/h. This open-loop test is specifically designed to evaluate the transient lateral handling and the roll dynamics of the chassis under continuous, periodic directional changes.

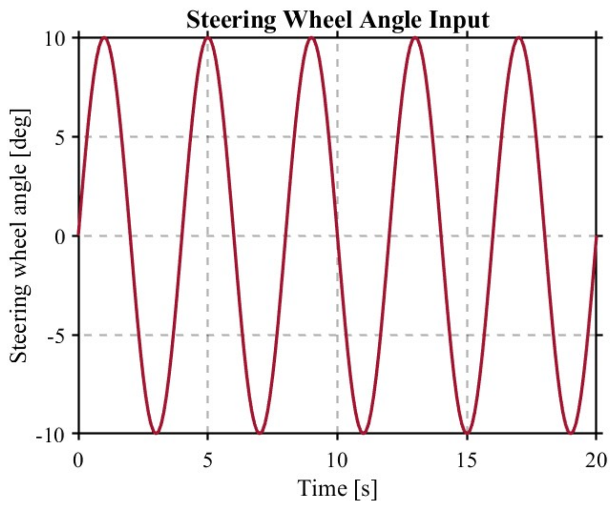

Figure 3.31: Sine wave steering input profile (10° amplitude, 0.25 Hz).

As shown in Figure 3.31, the steering wheel angle is defined as a pure sinusoidal signal with a peak amplitude of $\pm 10°$ and a frequency of 0.25 Hz. This type of input forces the vehicle into a regular sequence of left–right turns and creates a repeatable test condition that is well suited to studying how quickly and smoothly the vehicle reacts to the steering command, in particular in terms of lateral acceleration and tire forces.

In the following, the analysis of wheel and tire dynamics is limited to the rear axle. During lateral manoeuvres, the most relevant effects for load transfer are the chassis roll motion and the resulting change of vertical forces between the left and right wheels on the same axle. For this reason, comparing the rear-left and rear-right sides is sufficient to capture the main asymmetric behaviour of the vehicle, without adding extra plots from the front axle that would not change the overall conclusions.

Starting with the *chassis motion* category, the relevant plots characterizing this aspect of the vehicle's dynamic response are presented below.

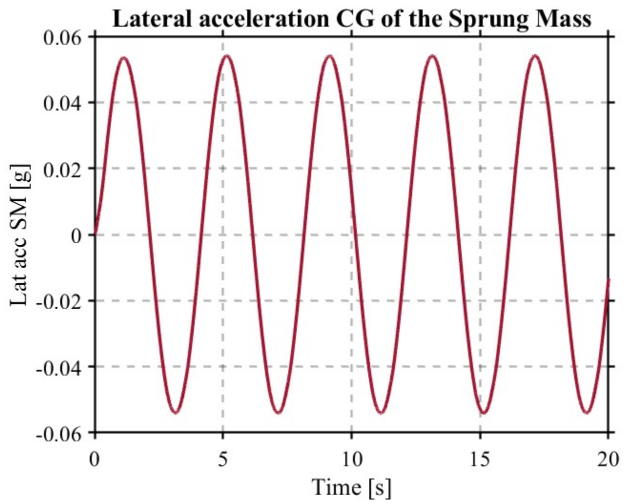

Figure 3.32: Sine wave steering maneuver: Lateral acceleration of the sprung-mass centre of gravity.

The *lateral acceleration of the sprung mass* shows an almost harmonic response that closely follows the 0.25 Hz steering input. The signal settles at peak amplitudes of about ± 0.055 g, which correspond to a mild lateral excitation and indicate that the vehicle operates well within its linear handling range, without approaching saturation of the tire lateral forces. These values are consistent with a comfortable manoeuvre that does not challenge the available grip and keeps the chassis response in the linear regime.

Remaining within the context of the *chassis motion*, two further parameters of critical importance for evaluating the vehicle's lateral dynamics are the **body roll angle** and the **body roll acceleration**. The corresponding time histories are reported below and provide additional insight into how the vehicle tilts and how fast this roll motion develops and is damped during the sine-wave steering manoeuvre.

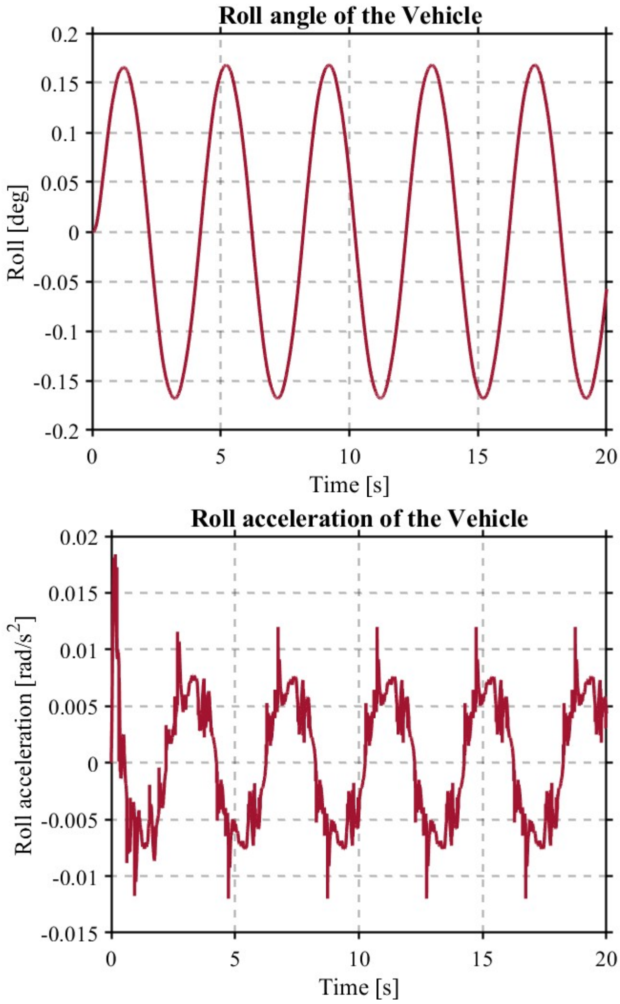

Figure 3.33: Sine wave steering maneuver: Roll angle (top) and roll acceleration (bottom) of the vehicle body.

The *roll angle of the vehicle* follows the sine-wave steering input with a nearly harmonic trend and small amplitudes, oscillating between about $-0.17°$ and $+0.17°$. This confirms that the chassis roll motion remains limited throughout the manoeuvre. The corresponding *roll acceleration of the vehicle* shows periodic peaks that are synchronized with the changes of roll angle, but their magnitude stays low and does not exhibit any unstable growth. Taken together, these plots indicate that the vehicle rolls smoothly from side to side and that the suspension effectively controls the onset and decay of the roll motion during the test.

Finally, concluding with the *tires motion* category, the analysis focuses on the **lateral forces** generated on the tires at the rear axle. The corresponding plots for these quantities are presented below.

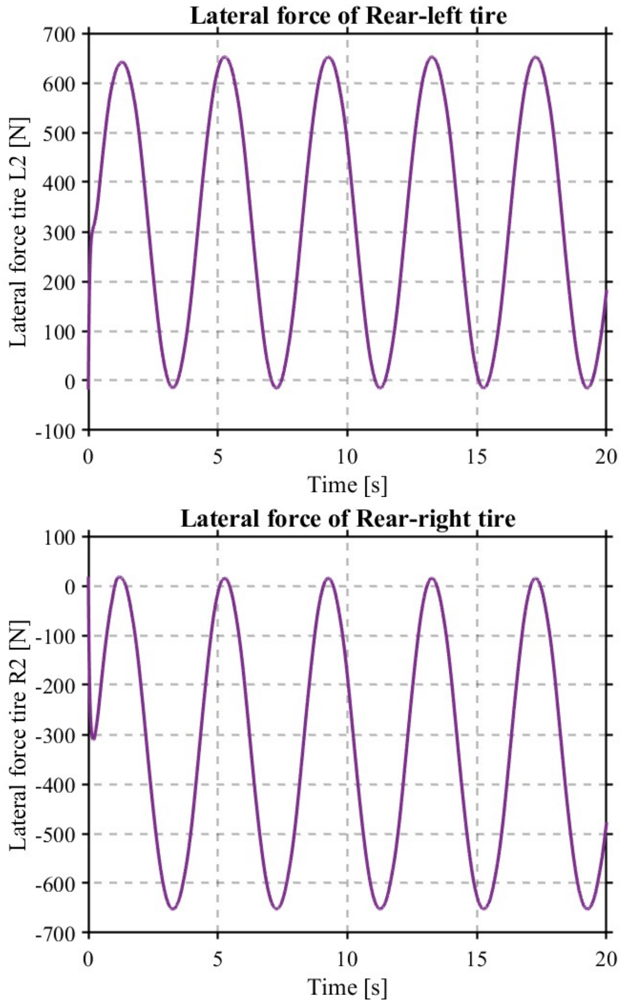

Figure 3.34: Sine wave steering maneuver: Lateral tire forces generated at the rear-left (top) and rear-right (bottom) wheels.

The *lateral forces* generated by the rear-left ($F_{y,L2}$) and rear-right ($F_{y,R2}$) tires follow the 0.25 Hz steering input with a regular harmonic trend and oscillate around mean values of about +315 N and −315 N. This offset is consistent with the baseline suspension geometry, for example the static toe and camber settings that create a small lateral force even in straight driving.

During the sine-wave manoeuvre these forces vary by roughly ±330 N around their mean values, which stays within a range where the tires can supply the requested lateral grip without approaching saturation, so the rear axle behaviour remains essentially linear over the entire test and no critical loss of adhesion is observed.

***Lateral dynamics*: Step steering 45° - 50 km/h**

is a step steering manoeuvre carried out at a constant speed of 50 km/h. This manoeuvre is mainly used to assess how the vehicle responds to a sudden change in steering, in terms of transient yaw behaviour and the way it settles into steady-state cornering. The steering wheel input used in the simulation is shown in the plot below.

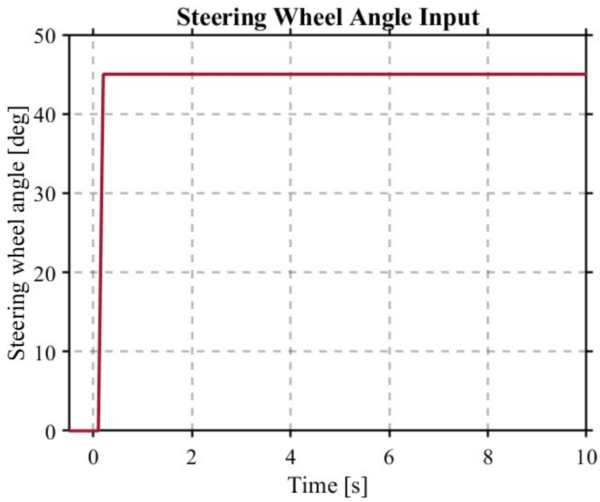

Figure 3.35: Steering wheel angle input for the step steer maneuver.

As shown in the plot, the steering wheel angle makes a rapid ramp from 0° to a constant value of 45° shortly after the start of the simulation. This sudden change approximates a step input and subjects the vehicle to a strong transient lateral excitation before it settles into steady-state cornering for the rest of the 10 s window.
In standard vehicle dynamics testing, the step steer manoeuvre is used to study the transient response of the chassis, by applying a constant steering input in a very short time. From the resulting yaw rate and lateral acceleration signals, key indicators such as response time, overshoot and settling time can be extracted. Once the transient vanishes, the vehicle reaches steady-state cornering, which reveals its basic handling balance and whether it behaves mainly as an understeer or oversteer car under continuous lateral loading.

To maintain a consistent approach throughout the study, the vehicle's dynamic response is characterized by considering the same two areas of interest analyzed in the previous lateral dynamics manoeuvre: *chassis motion* and *tires motion*. Starting from the *chassis motion* category, the key plots describing this part of the vehicle's dynamic response are shown below.

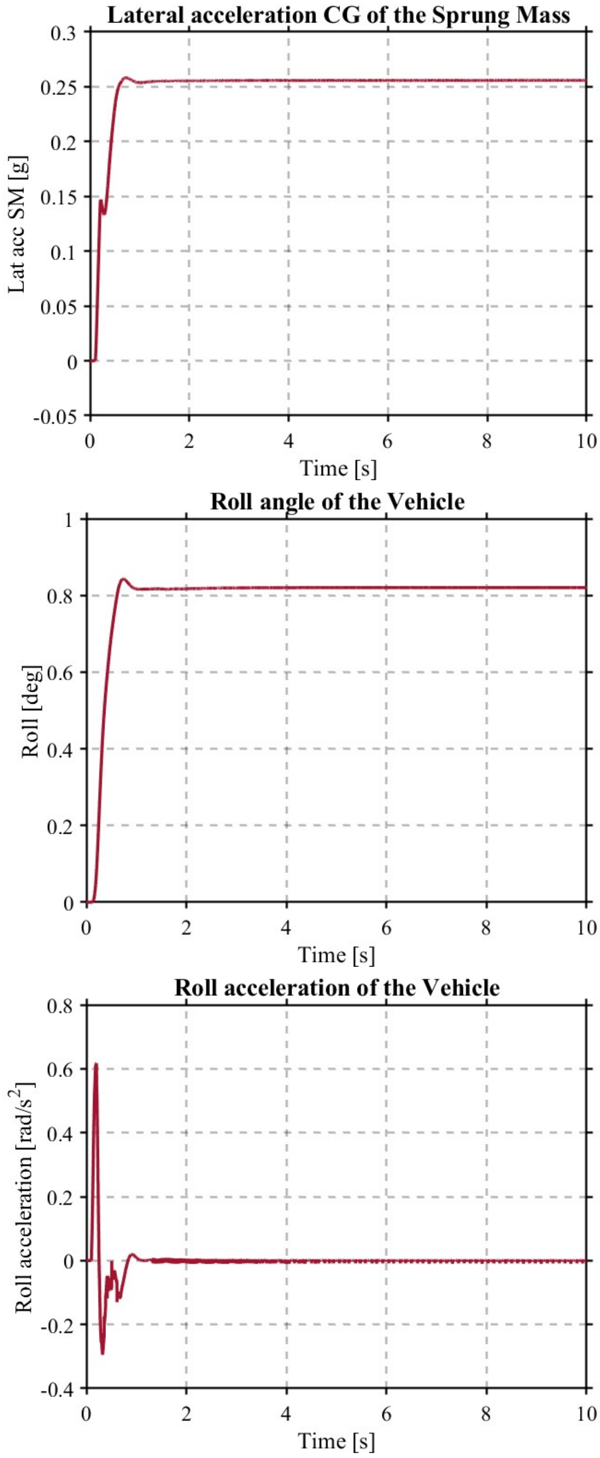

Figure 3.36: Step steer maneuver: Time history of the lateral acceleration of the sprung-mass centre of gravity(1), of the roll angle (2) and roll acceleration (3) of the vehicle body.

The *lateral acceleration of the sprung mass* shows a fast rise immediately after the step steering input and then stabilizes at a steady value of about 0.26 g, indicating that the vehicle quickly reaches a constant cornering condition. The *roll angle of the vehicle* exhibits a similar behaviour, with a rapid increase up to approximately 0.82° followed by a flat plateau, which confirms that the chassis roll motion is limited and well controlled. The corresponding *roll acceleration* displays a short initial burst, associated with the onset of roll, and then decays towards zero, showing that the roll dynamics are effectively damped and do not generate persistent oscillations.

To conclude the analysis, the focus shifts to the final category, namely the *tires motion*, evaluating its relevant tire key indicators.

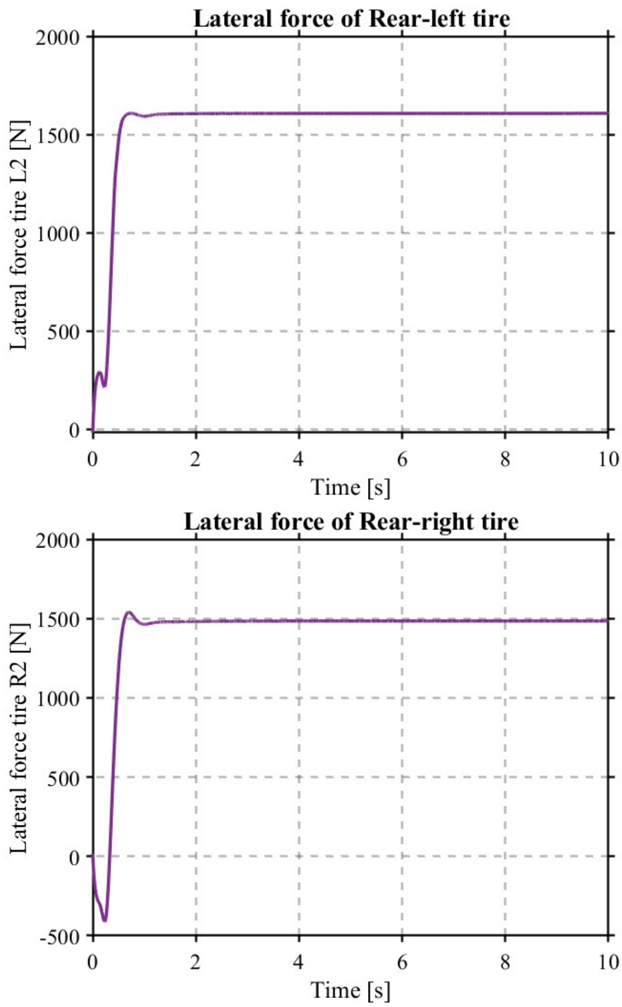

Figure 3.37: Step steer maneuver: Lateral tire forces generated at the rear-left (top) and rear-right (bottom) wheels.

The lateral forces of the rear-left ($F_{y,L2}$) and rear-right ($F_{y,R2}$) tires show a fast transient response and reach a stable level in less than one second. In the steady-state cornering phase, the left tire delivers about 1600 N, whereas the right tire settles around 1500 N. This difference is mainly due to lateral load transfer: the centrifugal force increases the vertical load on the outer rear tire, which allows it to generate a higher lateral force than the more lightly loaded inner tire.

Chapter 4

Vehicle model validation

4.1 Vehicle model validation overview

This chapter focuses on validating the custom vehicle model developed in the previous sections to ensure its accuracy and physical reliability. To achieve this, the dynamic response of the proposed architecture is evaluated through a comparative analysis against two distinct baselines.

- *Standard default model*: The simulation outputs are first compared with a baseline vehicle model to check the global handling behaviour and overall chassis kinematics.
- *Quarter Car model*: The results are then compared with a theoretical quarter-car model developed in MATLAB/Simulink, specifically to validate the vertical dynamics and the suspension parameters.

This dual-validation approach confirms the mathematical fidelity of the model, ensuring it is suitable for advanced dynamic analyses.

4.2 Comparison with CarSim Default Vehicle Model

The first step of the validation process compares the dynamic response of the **custom vehicle** with a **standard CarSim default model** under the same test conditions. By examining the time-history plots of the main state variables, this analysis highlights the handling features introduced by the modified mass distribution, suspension geometry and tyre properties. This comparison is used to verify the overall stability and the physically consistent behaviour of the proposed vehicle architecture.

4.2.1 Stelvio vs Default Vehicle: ISO Class B Road Profile at 70 km/h

To evaluate the vertical dynamics, both vehicles are simulated on an ISO Class B road profile at a constant speed of 70 km/h. The following plots present the time-history responses of the key variables of interest: the vertical accelerations of the sprung and unsprung masses, together with the vertical tire forces. These profiles will later be used as the basis for a *Root Mean Square (RMS)* comparison, with the goal of quantifying and contrasting the **ride comfort** and **road holding** performance of the two models.

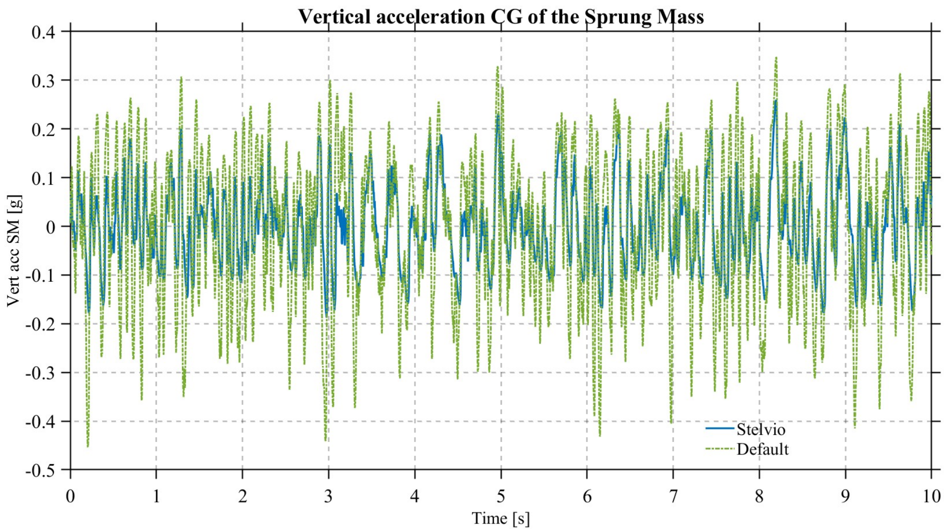

Figure 4.1: Stelvio vs Default vehicle: Vertical acceleration of the sprung mass for an ISO B Road at 70 km/h.

The time-history plot of the *sprung mass vertical acceleration* highlights the different ride characteristics of the two vehicles. The default model shows larger oscillation amplitudes, with peaks that often exceed ±0.3 g, whereas the Stelvio model tends to remain within a narrower ±0.2 g band. These differences reflect the specific suspension layouts and mass distributions of the two configurations, rather than a performance improvement of one over the other.

To quantify this behaviour, the *Root Mean Square* values of the signals were computed: the Stelvio model reaches a RMS vertical acceleration of about **0.086** g, compared with **0.160** g for the default vehicle. These results show that the custom Stelvio model reproduces vertical dynamics that are consistent with those of a reference default vehicle, making it a credible reference for the subsequent analyses.

Shifting the focus to the unsprung masses, the analysis now examines the **vertical accelerations of the front wheel centers**. These metrics provide a crucial insight into the vehicle's road-holding capabilities of the models.

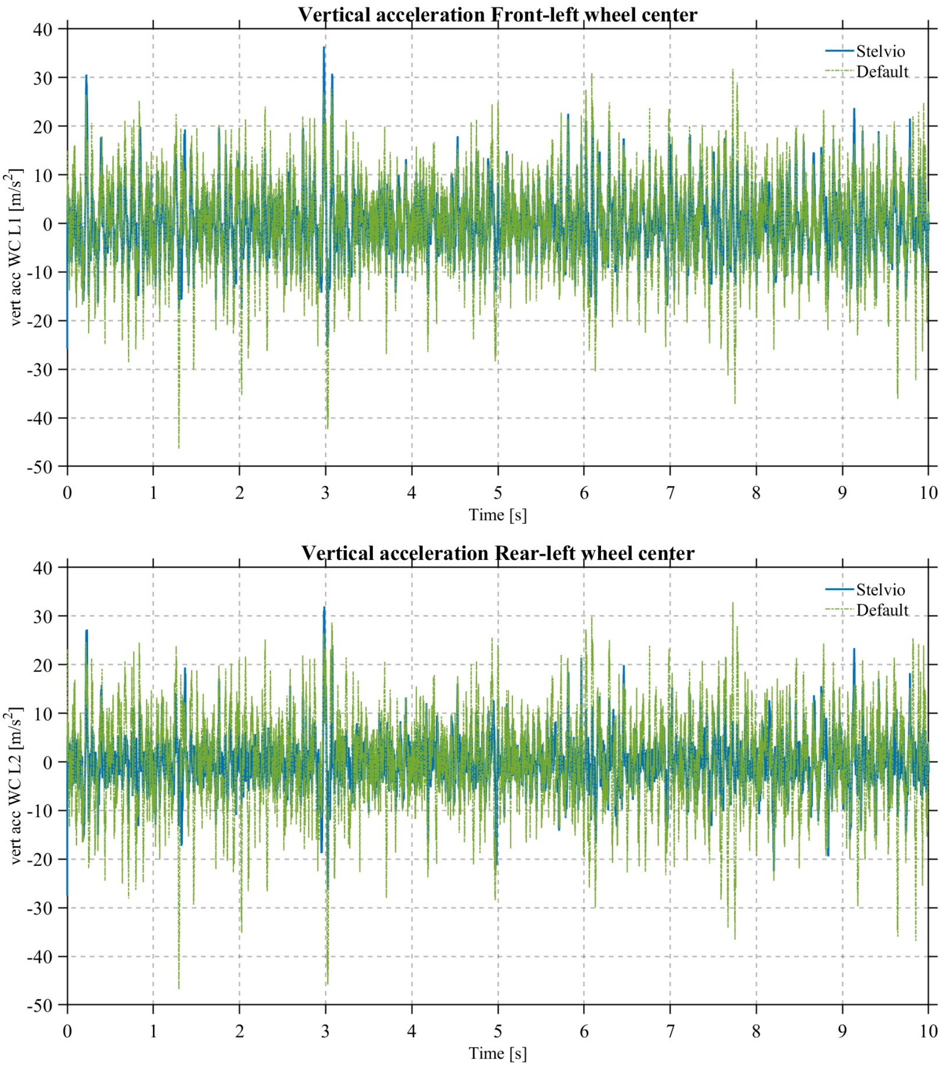

Figure 4.2: Stelvio vs Default vehicle: Vertical acceleration of the front-left (top) and front-right (bottom) wheel centers for an ISO B Road at 70 km/h.

The time-history plots for the front-left (L1) and rear-left (L2) wheel centres highlight a clear difference in the *wheel acceleration* levels of the two models. While the default vehicle shows pronounced spikes exceeding ± 30 m/s^2, the Stelvio configuration generally remains within a narrower ± 15 m/s^2 range. These features are a direct consequence of the respective suspension and tyre characteristics and show comparable trends between the two configurations, indicating that the underlying vertical dynamics are sufficiently similar to make the Stelvio model a credible and plausible representation of a real vehicle.

To conclude this comparative analysis, the **dynamic vertical tire forces** are evaluated. The plots of these two quantities are reported in the following:

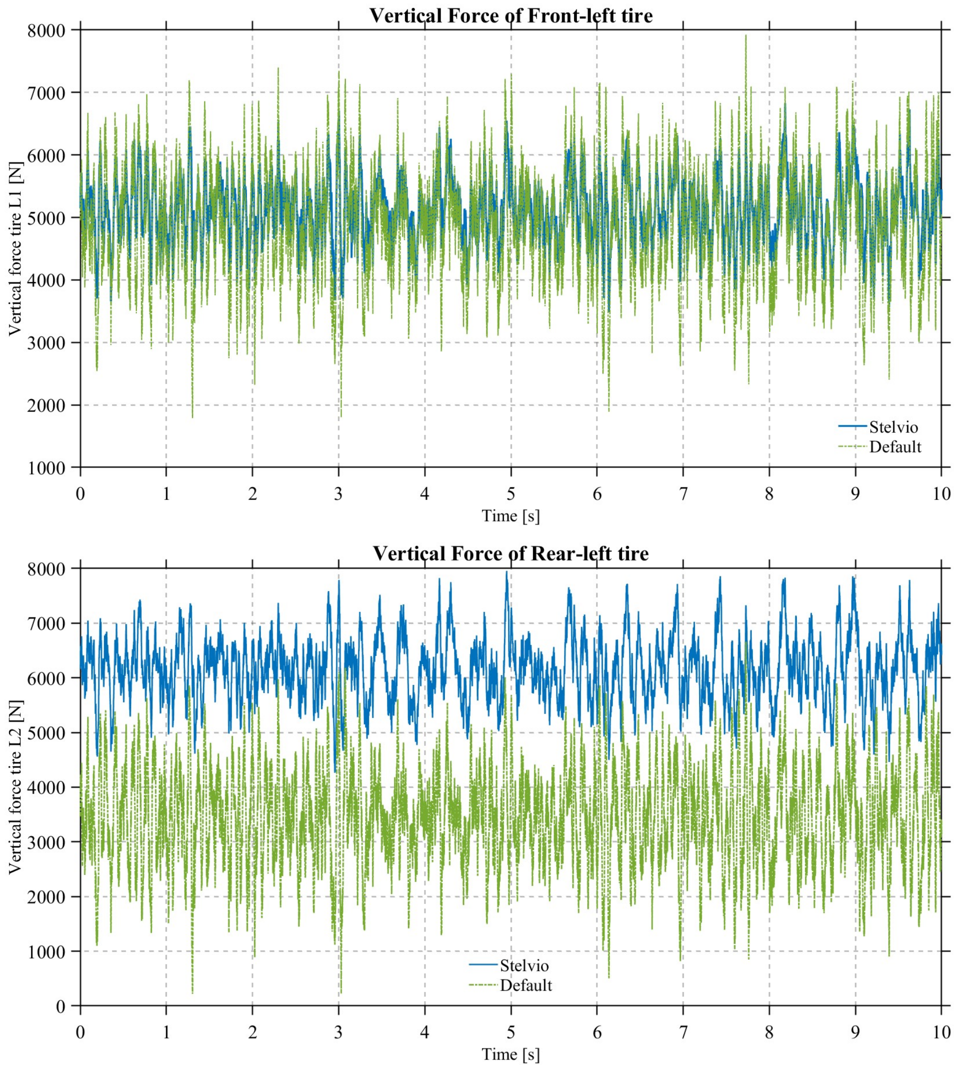

Figure 4.3: Stelvio vs Default vehicle: Vertical tire forces for the front-left (top) and rear-left (bottom) wheels for an ISO B Road at 70 km/h.

The offset in the average *force level*, especially on the rear axle, reflects the different inertial properties: the default vehicle has a mass of 1430 kg with a 50–50 distribution, whereas the Stelvio model has a mass of 2087 kg and a rear-biased

45–55 distribution. In spite of the higher static load, the custom vehicle shows smaller dynamic wheel-load variations, and the corresponding force histories remain in line with those of the template, indicating comparable trends and supporting the Stelvio configuration as a reliable representation for the road-holding analysis.

4.3 Comparison with a Quarter-car Model

The second validation phase compares the Stelvio model against a theoretical Quarter-Car model developed in MATLAB/Simulink environment. This simplified mathematical baseline is ideal for isolating and specifically validating the vertical dynamics and suspension parameters.

4.3.1 Stelvio vs Quarter-car Vehicle: ISO Class B Road Profile at 70 km/h

The test maneuver, road profile and vehicle speed remain strictly identical to the ones analyzed in the previous subsection. To properly compare the full vehicle against the simplified Quarter-Car model, this analysis focuses exclusively on the front axle. The following plots evaluate the same key variables considered before—vertical accelerations of the sprung and unsprung masses and the vertical tire force—with the addition of the damper compression, in order to provide a more complete view of the suspension kinematics.

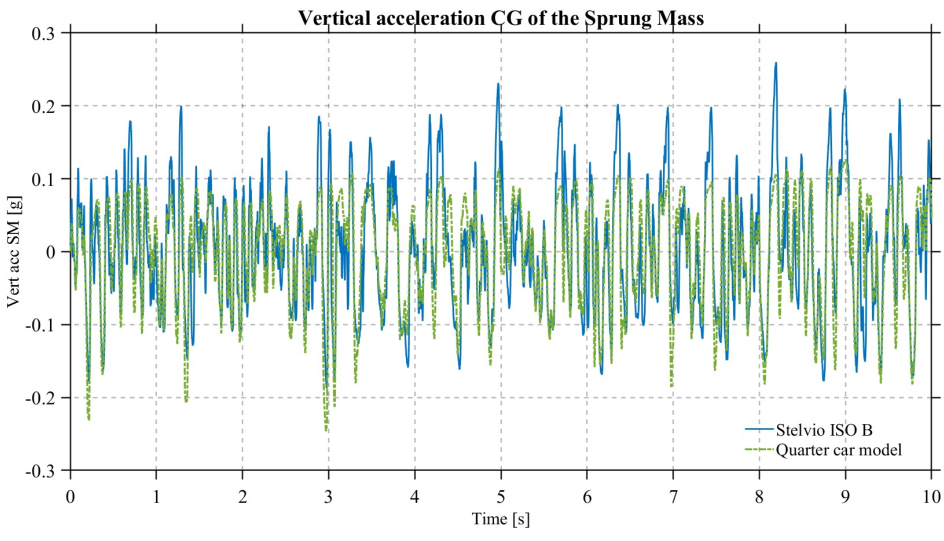

Figure 4.4: Stelvio vs Quarter-car: Vertical acceleration of the sprung mass for an ISO B Road at 70 km/h.

The time-history plot of the *sprung mass vertical acceleration* shows a strong similarity in the dominant frequency content of the two models. Differences in amplitude—such as the larger positive peaks of the Stelvio and the deeper negative excursions of the Quarter-Car—are expected and can be attributed to the simplified 1D nature of the theoretical model, which does not fully reproduce 3D kinematics, pitch and roll motions.

From a quantitative standpoint, the full Stelvio model yields an *RMS acceleration* of **0.086** g, compared with **0.075** g for the Quarter-Car. This small and physically consistent offset indicates that the vibrational energy transmitted to the body is of the same order in both cases, supporting the conclusion that the vertical suspension behaviour of the multi-body vehicle is well aligned with that of the simplified reference model.

Going on with the analysis, the focus shifts on the suspension kinematics by evaluating the **damper compression** on the front axle. This variable illustrates how effectively the suspension system exploits its available working space to absorb the road irregularities.

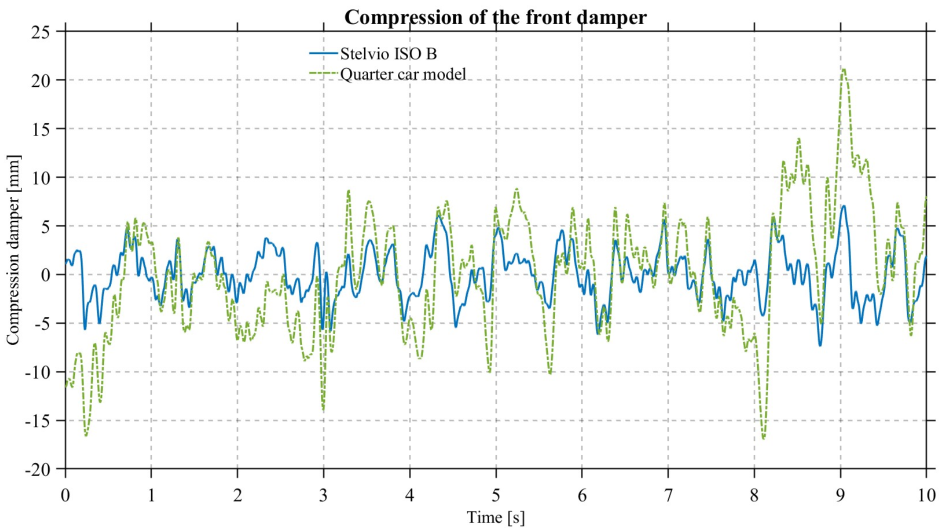

Figure 4.5: Stelvio vs Quarter-car: Front damper compression for an ISO B Road at 70 km/h.

The *damper compression* plot indicates that the basic suspension kinematics are consistent in both setups. The Quarter-Car model, however, shows much larger stroke amplitudes, with excursions above 20 mm and down to about -17 mm, whereas the complete Stelvio model remains confined to roughly ± 8 mm. This difference is expected and reflects the simplified 1D formulation of the theoretical model, which does not include the actual suspension geometry and 3D kinematic constraints present in the full multi-body vehicle representation.

After this kinematic analysis, the focus moves to the dynamic behaviour of the unsprung mass. The next plots report the **vertical acceleration of the front wheel centre** and the **vertical force of the front tyre**.

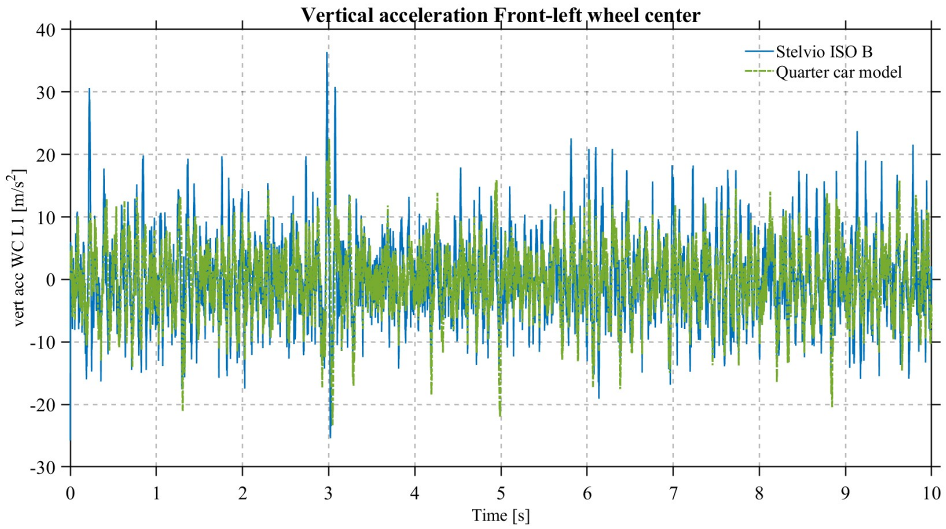

Figure 4.6: Stelvio vs Quarter-car: Vertical acceleration of the front wheel center for an ISO B Road at 70 km/h.

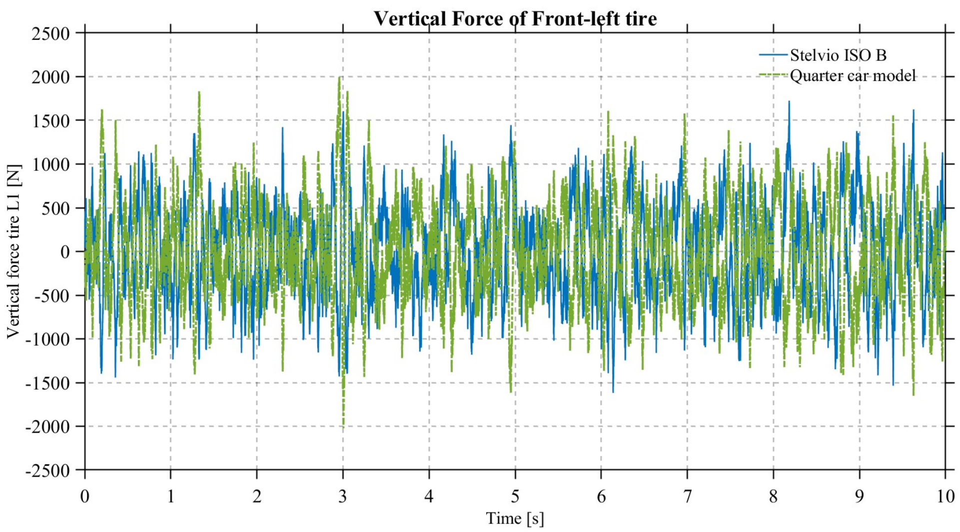

Figure 4.7: Stelvio vs Quarter-car: Vertical tire force of the front tire for an ISO B Road at 70 km/h.

- *Front wheel centre acceleration*: The full Stelvio model shows higher high-frequency content, with sharp transient peaks that can exceed 30 m/s^2, whereas the 1D Quarter-Car response remains confined to a narrower band. This behaviour is consistent with the simplified nature of the theoretical model, which does not reproduce the full set of 3D multi-link constraints and detailed tire–road interactions present in the complete vehicle.

- *Dynamic vertical tire force*: The corresponding force plot indicates that both models share the same fundamental trends, but with different fluctuation amplitudes. The Quarter-Car exhibits variations that can reach about ±2000 N, while the Stelvio solution is mostly contained within ±1500 N. These differences reflect the distinct suspension representations, while the overall evolution of the signals remains comparable, supporting the use of the full Stelvio model as a realistic description of front-corner road-holding behaviour.

4.3.2 Stelvio vs Quarter-car Vehicle: Bump Road Profile at 30 km/h

Following the continuous excitation analysis, this section evaluates the transient response over a discrete bump profile at 30 km/h. This specific test compares the full Stelvio multi-body model against the 1D Quarter-Car baseline to directly evaluate shock absorption and damping settling time when the vehicle is subjected to an isolated vertical irregularity.

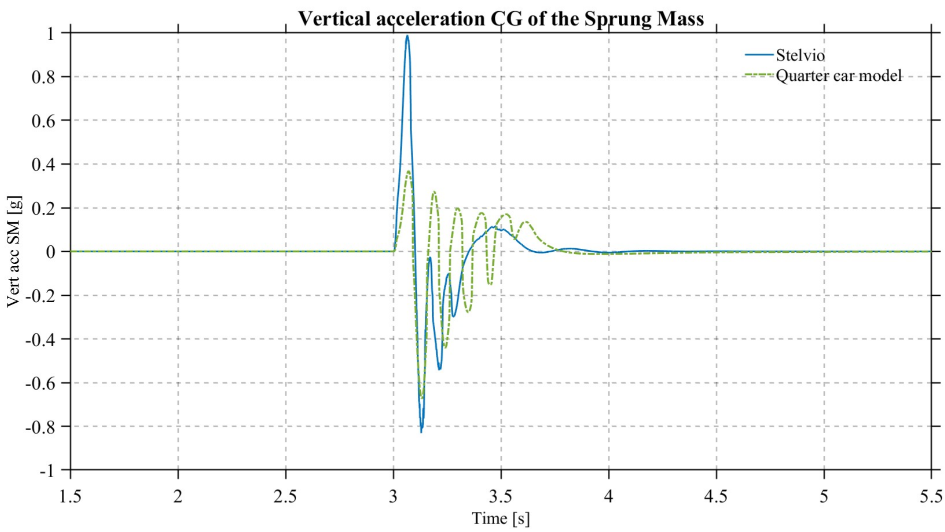

Figure 4.8: Stelvio vs Quarter-Car: Sprung mass vertical acceleration for a bump at 30 km/h.

The *sprung mass vertical acceleration* (Figure 4.8) highlights two distinct transient behaviours. At the instant of impact ($t \approx 3$ s), the Stelvio model shows a sharper peak, reaching nearly 1.0 g, whereas the Quarter-Car response remains below 0.4 g, in line with the more idealised representation of the suspension geometry. In the phase following the impact, however, the full vehicle settles noticeably faster, returning to a quasi-steady condition in about one second and avoiding the longer oscillations predicted by the 1D model. This combination of a more pronounced initial peak and quicker decay is reflected in the overall RMS values, equal to **0.084** g for the complete Stelvio and **0.063** g for the simplified Quarter-Car.

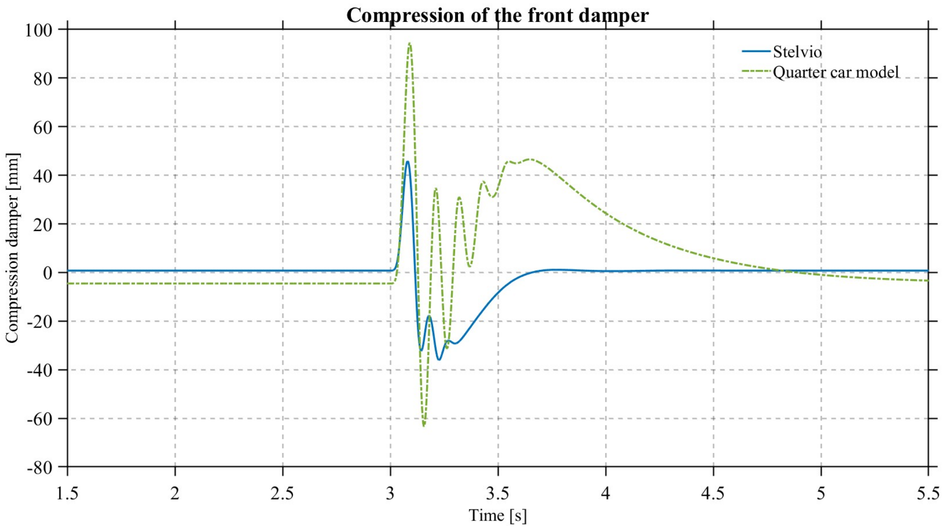

Figure 4.9: Stelvio vs Quarter-Car: Front damper compression for a bump at 30 km/h.

The *damper compression* (Figure 4.9) also highlights the different transient behaviours of the two models. At the moment of impact, the Quarter-Car clearly overestimates the stroke, with peaks of about 95 mm in compression and −60 mm in rebound, whereas the complete Stelvio model keeps the motion confined to roughly 45 mm and −35 mm. Thanks to realistic structural stiffness and 3D kinematic constraints, the full vehicle limits the maximum shock absorber travel and returns smoothly to equilibrium by $t \approx 4$ s, avoiding the persistent oscillations predicted by the idealized 1D formulation.

Following the analysis of the sprung mass and suspension kinematics, the evaluation now shifts to the unsprung mass dynamics and the consequent road-holding performance. The upcoming analysis will present the **vertical acceleration of the front wheel center** and the **dynamic vertical force of the front tire**. The plots of these two quantities are reported in the following.

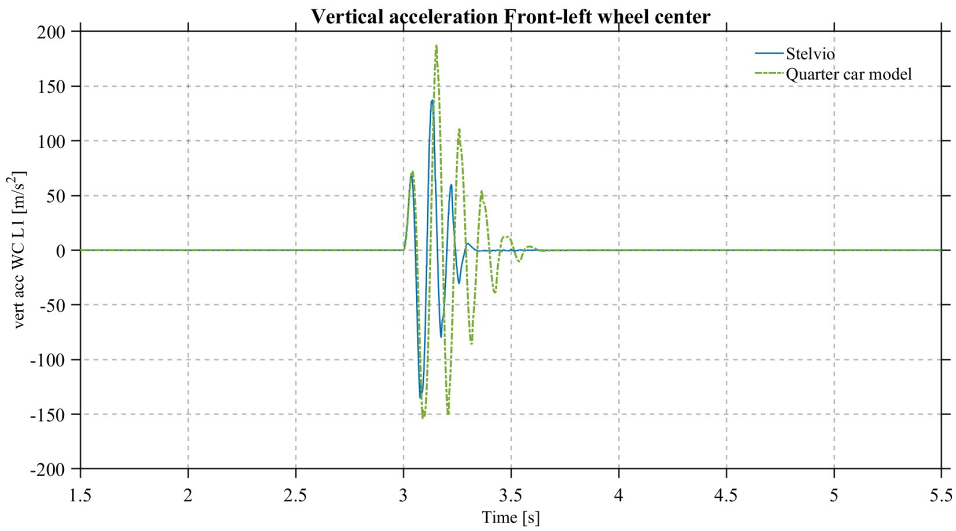

Figure 4.10: Stelvio vs Quarter-Car: Front-left wheel center vertical acceleration for a bump at 30 km/h.

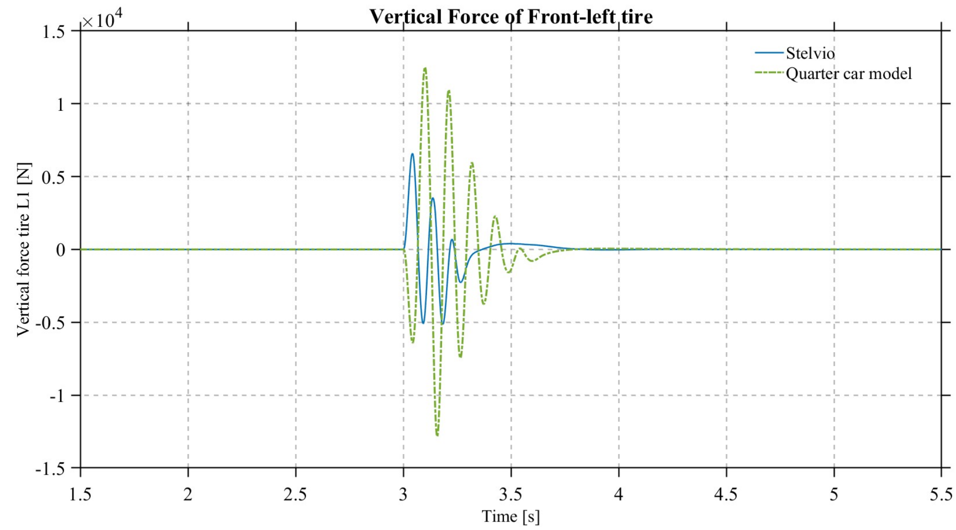

Figure 4.11: Stelvio vs Quarter-Car: Front-left tire vertical force for a bump at 30 km/h.

- *Front wheel centre acceleration*: The Quarter-Car model predicts very high transient peaks, approaching 190 m/s^2, together with longer residual oscillations. In comparison, the full Stelvio model limits the maximum acceleration to about 140 m/s^2 and returns to a stable condition by $t \approx 3.5$ s, which is consistent with the presence of realistic multi-link damping and 3D kinematic constraints.

- *Dynamic vertical tyre force*: The corresponding force history shows that the 1D model produces load variations exceeding 1.2×10^4 N, whereas the complete vehicle keeps the peak values close to 0.6×10^4 N and restores equilibrium more rapidly. Although the amplitudes differ, the main trends of the signals are comparable, indicating that the multi-body Stelvio representation captures a plausible evolution of tire–road contact forces after the bump event.

4.4 RMS Values Analysis

To provide an objective evaluation of the vehicle's dynamic performance, this section summarizes the Root Mean Square (RMS) values of the key metrics analyzed in the previous comparisons. The data are divided into two categories: vertical accelerations, which directly describe the kinematics of the sprung and unsprung masses, and vertical tire forces, which are crucial for assessing dynamic loads.

4.4.1 Stelvio vs Default Vehicle: ISO Class B Road Profile at 70 km/h

The following tables summarize the RMS metrics obtained from the full-vehicle comparison, numerically quantifying the dynamic differences between the custom Stelvio setup and the default baseline over the ISO B road profile.

Vertical Acceleration Metric	Stelvio model	Default model
Sprung Mass [g]	0.086	0.160
Front-Left (L1) Wheel Center [m/s^2]	6.559	9.563
Rear-Left (L2) Wheel Center [m/s^2]	5.169	9.665

Table 4.1: RMS Comparison: Vertical Accelerations for an ISO B Road at 70 km/h.

Vertical Tire Force Metric	Stelvio model	Default model
Front-Left (L1) F_z [N]	5129.4	4980.9
Rear-Left (L2) F_z [N]	6189.5	3580.4

Table 4.2: RMS Comparison: Vertical Tire Forces for an ISO B Road at 70 km/h.

- Table 4.1 reports the *RMS vertical accelerations* over the ISO B road at 70 km/h. The Stelvio model shows lower RMS levels for the sprung mass and both left wheel centres, indicating a generally milder vertical excitation while maintaining trends that are consistent with those of the default baseline.
- Table 4.2 presents the *RMS dynamic vertical tire forces* on the left side. The Stelvio configuration yields higher RMS values at the front and rear tires, in line with its different mass distribution and static loading, but the force magnitudes remain comparable to the baseline, supporting a coherent picture of the road-holding behaviour.

4.4.2 Stelvio vs Quarter-car Vehicle: ISO Class B Road Profile at 70 km/h

The following tables summarize the RMS metrics comparing the front-left corner of the full Stelvio multi-body model against the theoretical 1D Quarter-Car baseline over the same ISO B road profile.

Vertical Acceleration Metric	Stelvio model	Quarter-Car model
Sprung Mass [g]	0.086	0.075
Wheel Center [m/s^2]	6.559	5.473

Table 4.3: RMS Comparison: Vertical Accelerations (Stelvio vs Quarter-Car).

Vertical Tire Force Metric	Stelvio model	Quarter-Car model
Dynamic F_z [N]	519.2	569.0

Table 4.4: RMS Comparison: Dynamic Vertical Tire Forces (Stelvio vs Quarter-Car).

- Table 4.3 reports the *RMS vertical accelerations* at the sprung mass and front-left wheel centre for the ISO B road. The Stelvio model yields RMS values that are only slightly higher than those of the Quarter-Car baseline, showing that the full multi-body vehicle reproduces a vertical response that is broadly consistent with the simplified 1D model.
- Table 4.4 summarizes the *RMS of the dynamic vertical tire force* at the front-left corner. The Quarter-Car model shows a marginally larger RMS value than the Stelvio configuration, yet the difference is limited, confirming that

both models predict comparable levels of dynamic loading at the tire–road interface for this operating condition.

4.4.3 Stelvio vs Quarter-car Vehicle: Bump Road Profile at 30 km/h

To quantitatively evaluate the transient response during the 30 km/h bump test, the subsequent tables outline the RMS metrics for both the complete Stelvio multi-body architecture and the 1D Quarter-Car baseline.

Vertical Acceleration Metric	**Stelvio model**	**Quarter-Car model**
Sprung Mass [g]	0.084	0.063
Wheel Center [m/s^2]	11.196	17.122

Table 4.5: RMS Comparison: Vertical Accelerations (Stelvio vs Quarter-Car).

Vertical Tire Force Metric	**Stelvio model**	**Quarter-Car model**
Dynamic F_z [N]	554.4	1298.4

Table 4.6: RMS Comparison: Dynamic Vertical Tire Forces (Stelvio vs Quarter-Car).

- Table 4.5 reports the *RMS vertical accelerations* during the 30 km/h bump test. The Stelvio model shows a slightly higher sprung-mass RMS value than the Quarter-Car (0.084 g versus 0.063 g), while the wheel-centre RMS accelerations are noticeably lower (11.196 m/s^2 versus 17.122 m/s^2), indicating comparable but not identical vertical responses for the two modelling approaches.
- Table 4.6 summarizes the *RMS dynamic vertical tire force* at the front-left corner for the same manoeuvre. The Quarter-Car model yields a larger RMS value (1298.4 N) than the Stelvio configuration (554.4 N), consistently with the stronger load oscillations observed in the time histories, but both results remain within a realistic range and support the plausibility of the custom vehicle model.

Chapter 5

Control strategies implementation: Ideal Skyhook and Groundhook

5.1 Ideal Skyhook and Groundhook: theoretical overview

In vehicle dynamics, active and semi-active suspension control strategies are algorithms that continuously adjust the damping forces in real time. Their main objective is to overcome the physical limitations of conventional passive suspensions, mitigating the intrinsic trade-off between passenger ride comfort and vehicle road holding. Within this framework, two theoretical control paradigms are commonly used as ideal performance references: the *Ideal Skyhook* and the *Ideal Groundhook*.

- **Ideal Skyhook:** A theoretical control strategy designed to maximize ride comfort. It suppresses chassis vibrations by simulating a virtual shock absorber connected between the vehicle's sprung mass and a fixed, absolute inertial reference frame (the "sky").
- **Ideal Groundhook:** A control strategy dedicated at maximizing road holding. It operates by simulating a fictitious damper connected between the unsprung mass and a fixed inertial reference frame (the "ground"), aiming to minimize dynamic tire load variations.

The subsequent sections provide a comprehensive analysis of these two reference control strategies. Specifically, each approach is detailed through its theoretical principles, analytical formulation and a schematic graphical representation.

5.1.1 Ideal Skyhook: theoretical and analytical characterization

The Ideal Skyhook strategy represents a virtual shock absorber, defined by the damping coefficient c_{sky}, directly connected between the vehicle sprung mass and an absolute, stationary reference frame (the "sky") [25].

The control law is based solely on the absolute vertical velocity of the chassis: a proportional damping force is applied to oppose upward body motion, while the damping action is reduced during downward motion so as not to transmit road-induced forces back into the passenger compartment.

The main objective is to maximize ride comfort by isolating the chassis as much as possible from ground disturbances. In doing so, the sprung mass motion is effectively stabilized, but the wheel assembly receives less damping and the unsprung mass oscillations tend to increase. For this reason, the Ideal Skyhook is usually regarded as a theoretical benchmark for comfort optimization, inherently accepting a degradation in tire grip and road-holding performance. [26].

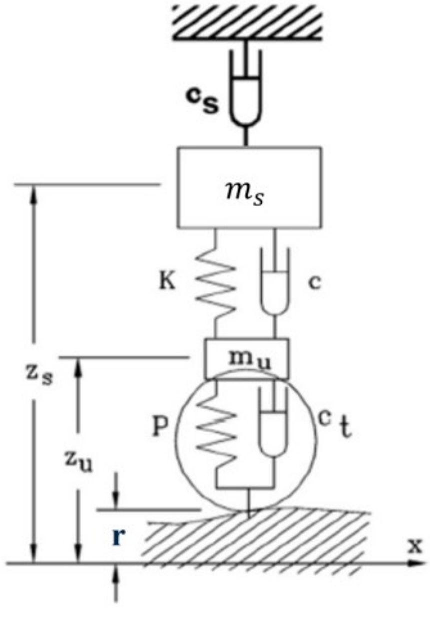

Figure 5.1: Schematic representation of the Ideal Skyhook control strategy.

Following this conceptual overview, the analytical formulation of the Ideal Skyhook strategy is detailed in the following. Establishing this mathematical characterization is a crucial step, as it will serve as the theoretical foundation required to evaluate and quantify the ride comfort index of the target vehicle's suspension system in the subsequent sections.

To maintain consistency with the notation introduced in Chapter 2, the variables from the reference mathematical model presented in Figure 5.1 have been appropriately adapted. Specifically:

- the suspension stiffness K is denoted as k_s;
- the passive suspension damping c is expressed as c_s;
- the tire stiffness P is represented by k_t;
- the theoretical skyhook damping coefficient c_s is redefined as c_{sky}.

The equations of motion for the Ideal Skyhook quarter-car model are therefore expressed as follows:

$$m_s\ddot{z}_s + c_s(\dot{z}_s - \dot{z}_u) + c_{sky}\dot{z}_s + k_s(z_s - z_u) = 0 \tag{5.1}$$

$$m_u\ddot{z}_u + c_s(\dot{z}_u - \dot{z}_s) + c_t(\dot{z}_u - \dot{r}) + k_s(z_u - z_s) + k_t(z_u - r) = 0 \tag{5.2}$$

These equations can be reorganized and written in matrix form to represent the complete dynamic system:

$$\begin{bmatrix} m_s & 0 \\ 0 & m_u \end{bmatrix} \begin{Bmatrix} \ddot{z}_s \\ \ddot{z}_u \end{Bmatrix} + \begin{bmatrix} c_s + c_{sky} & -c_s \\ -c_s & c_s + c_t \end{bmatrix} \begin{Bmatrix} \dot{z}_s \\ \dot{z}_u \end{Bmatrix} + \begin{bmatrix} k_s & -k_s \\ -k_s & k_s + k_t \end{bmatrix} \begin{Bmatrix} z_s \\ z_u \end{Bmatrix} = \begin{Bmatrix} 0 \\ c_t\dot{r} + k_t r \end{Bmatrix} \tag{5.3}$$

Since attaching a damper to an absolute reference is physically unfeasible, the Ideal Skyhook serves purely as a theoretical control target. In practice, this imaginary configuration is approximated by a semi-active damper generating a controllable force between the sprung and unsprung masses [26].

5.1.2 Ideal Groundhook: theoretical and analytical characterization

As a complementary concept to the Skyhook approach, the Ideal Groundhook strategy models a virtual shock absorber, described by the damping coefficient c_{ground}, directly connected between the vehicle unsprung mass and a fixed ground reference [25].

In this case, the control action is centred on the wheel assembly rather than on the chassis: by virtually anchoring the unsprung mass to the road surface, the system generates a damping force that actively reduces the vertical oscillations of the tire.

The main objective is to minimize dynamic tire–road contact forces and thus maximize road-holding capability. While this configuration stabilizes the tire contact and improves handling, it tends to transmit higher levels of vibration to the vehicle body and the passenger compartment. For this reason, the Ideal Groundhook is regarded as the theoretical benchmark for tire grip and stability, achieved at the expense of pure ride comfort.

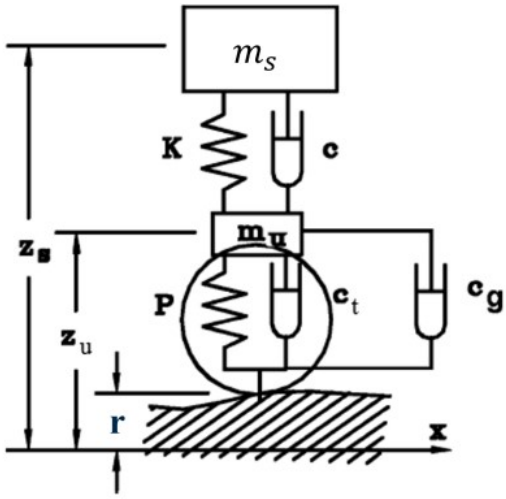

Figure 5.2: Schematic representation of the Ideal Groundhook control strategy.

Similar to the previous section, the analytical formulation of the Ideal Groundhook strategy is detailed below. To maintain consistency, the variables from the reference mathematical model presented in Figure 5.2 remain identical to those defined in the previous section, with the sole exception of the theoretical groundhook damping coefficient c_g, which is redefined as c_{ground}.
The equations of motion for the Ideal Groundhook quarter-car model are therefore expressed as follows:

$$m_s\ddot{z}_s + c_s(\dot{z}_s - \dot{z}_u) + k_s(z_s - z_u) = 0 \tag{5.4}$$

$$m_u\ddot{z}_u + c_s(\dot{z}_u - \dot{z}_s) + c_t(\dot{z}_u - \dot{r}) + c_{ground}(\dot{z}_u - \dot{r}) + k_s(z_u - z_s) + k_t(z_u - r) = 0 \tag{5.5}$$

Yielding the following equation in matrix form to represent the complete dynamic system:

$$\begin{bmatrix} m_s & 0 \\ 0 & m_u \end{bmatrix} \begin{Bmatrix} \ddot{z}_s \\ \ddot{z}_u \end{Bmatrix} + \begin{bmatrix} c_s & -c_s \\ -c_s & c_s + c_t + c_{ground} \end{bmatrix} \begin{Bmatrix} \dot{z}_s \\ \dot{z}_u \end{Bmatrix} + \\ + \begin{bmatrix} k_s & -k_s \\ -k_s & k_s + k_t \end{bmatrix} \begin{Bmatrix} z_s \\ z_u \end{Bmatrix} = \begin{Bmatrix} 0 \\ (c_t + c_{ground})\dot{r} + k_t r \end{Bmatrix} \tag{5.6}$$

As with the skyhook strategy, the physical realization of an ideal groundhook damper is inherently impossible. In practical applications, this conceptual model is approximated by modulating a controllable force between the vehicle's sprung and unsprung masses.

5.2 Performance Indexes Analysis

To objectively evaluate and compare the effectiveness of the above mentioned suspension configurations, a rigorous analysis of specific performance indexes is required. The following evaluation will focus on two primary metrics:

- The **root mean square (RMS) value of the sprung mass acceleration** **(**$\ddot{z}_s$**)**, which serves as the fundamental indicator for passenger ride comfort;
- The **road holding coefficient** η_{RH}, which quantifies the tire's ability to maintain stable contact with the ground, ensuring vehicle handling and safety. This index is analytically calculated as the ratio between the dynamic tire force and the total static weight of the quarter-car system:

  $$\eta_{RH} = \frac{F_{tire}}{(m_s + m_u)g} \tag{5.7}$$

  where F_{tire} represents the dynamic tire-road contact force, g is the acceleration due to gravity and the term $(m_s + m_u)$ defines the total mass of the system, combining the sprung and unsprung masses.

The dynamic behaviour of these two performance parameters will be systematically analyzed as a function of different damping configurations. In particular, the variations of the indexes will be evaluated with respect to:

- The passive relative damping coefficient c_{rel};
- The skyhook damping coefficient c_{sky}, when evaluating the Ideal Skyhook control strategy;
- The groundhook damping coefficient c_{ground}, when assessing the Ideal Groundhook control strategy.

5.2.1 Performance indexes as a function of the relative damping c_{rel}

Before assessing advanced control strategies, it is useful to establish a reference by analyzing the dynamic behaviour of a conventional passive suspension. In this standard quarter-car configuration, the response is mainly governed by the passive relative damping coefficient c_{rel}, which acts only on the relative motion between sprung and unsprung masses.

This section examines how the previously defined performance indicators—the root mean square (RMS) of the sprung mass acceleration and the road-holding coefficient η_{RH}—change over a range of c_{rel} values.

Analyzing these trends is essential to expose the basic design compromise of passive dampers, namely the unavoidable trade-off between isolating the chassis to improve passenger comfort and controlling the wheel assembly to secure adequate tire grip. The graphical results of this parametric study are reported and discussed in the following plots.

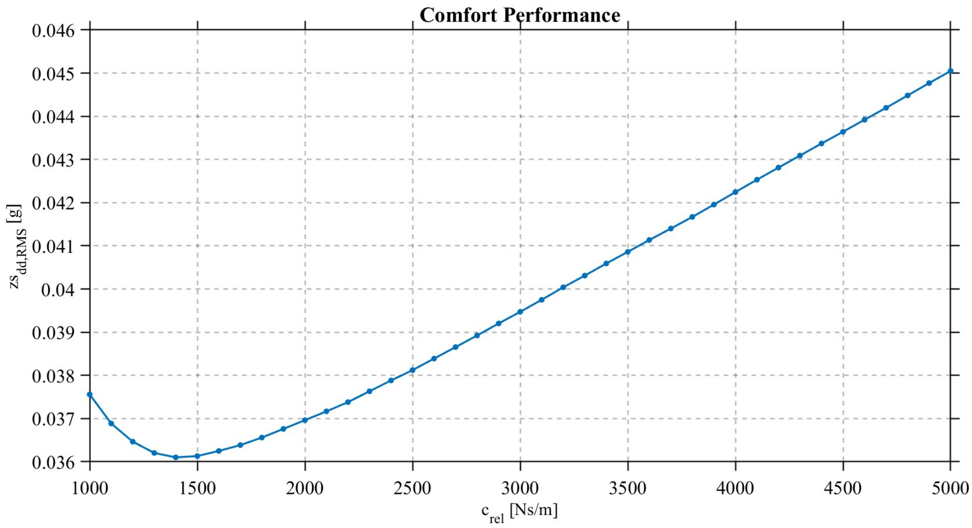

Figure 5.3: RMS value of the sprung mass acceleration as a function of the relative damping coefficient c_{rel}.

Figure 5.3 illustrates the **sprung mass acceleration RMS** as a function of the passive relative damping c_{rel}. The curve exhibits a convex trend with a well-defined global minimum.

At lower damping values (approaching 1000 Ns/m), the underdamped system struggles to dissipate the spring's kinetic energy, resulting in amplified chassis oscillations. As damping increases, ride comfort improves, reaching its optimal dynamic isolation at a minimum RMS value near 1400 Ns/m.

Beyond this threshold, further increases in c_{rel} progressively degrade ride comfort. Excessive damping creates a rigid dynamic coupling between the masses, transmitting high-frequency road disturbances directly to the chassis. This phenomenon is reflected in the steady, nearly linear increase of the acceleration RMS as c_{rel} approaches 5000 Ns/m.

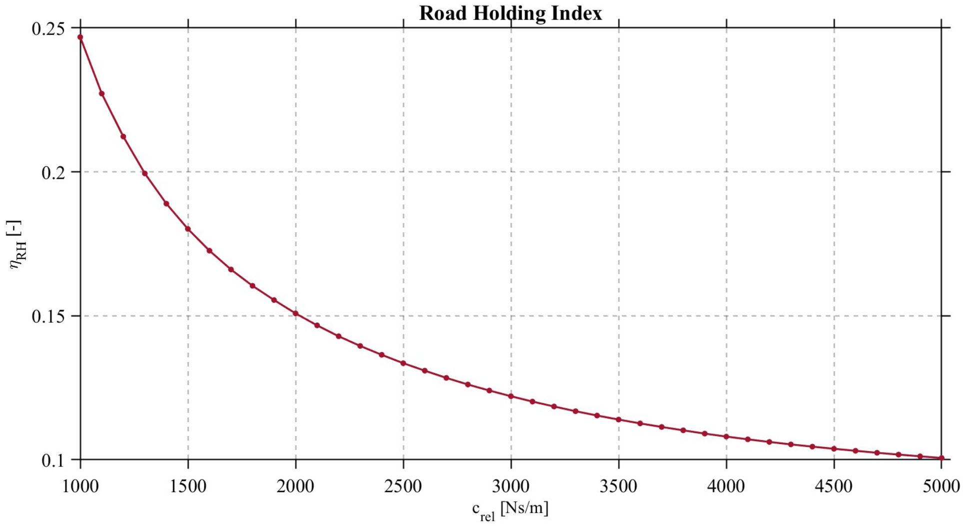

Figure 5.4: Road holding coefficient η_{RH} as a function of the relative damping coefficient c_{rel}.

Figure 5.4 shows how the **road-holding coefficient** η_{RH} varies with the passive relative damping c_{rel}. Over the investigated range, the curve displays a monotonically decreasing trend. At low damping levels, pronounced unsprung-mass oscillations cause large fluctuations in the dynamic tire forces, which translate into a higher (i.e. worse) road-holding index. As c_{rel} increases, the suspension damps the vertical motion of the wheel assembly more effectively, stabilizing the tire footprint and gradually improving grip.

When this behaviour is compared with the previous sprung-mass acceleration RMS plot, the intrinsic compromise of passive suspensions clearly emerges: high damping values (for example above 1400 Ns/m) are beneficial for road holding and overall stability, but they inevitably penalize passenger comfort.

5.2.2 Performance indexes as a function of the damping c_{sky}

Having established the baseline limitations of a passive suspension, this section evaluates the dynamic behaviour of the Ideal Skyhook control strategy. In this

configuration, the system's performance is primarily governed by the skyhook damping coefficient c_{sky}, which virtually connects the sprung mass to an absolute fixed reference.
The resulting trends highlight the theoretical advantages of the skyhook logic in isolating the chassis and overcoming the traditional passive trade-offs.

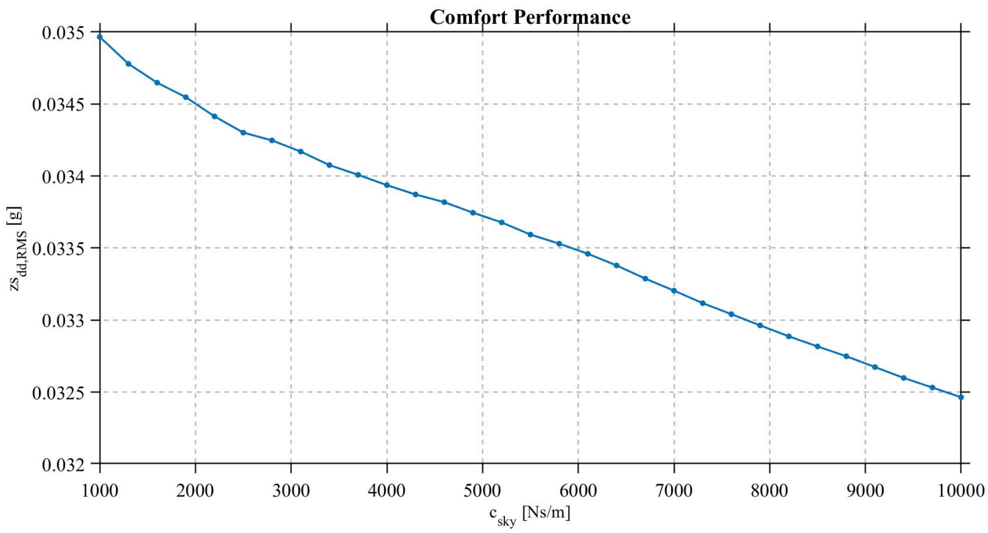

Figure 5.5: RMS value of the sprung mass acceleration as a function of the skyhook damping coefficient c_{sky}.

The dynamic behaviour of the Ideal Skyhook strategy is illustrated in Figure 5.5. The analysis of the performance metric shows that the **sprung mass acceleration RMS** follows a clearly monotonically decreasing trend over the investigated range of c_{sky}. As the skyhook damping coefficient increases, the virtual damper connected to the inertial "sky" reference becomes more effective in dissipating energy, progressively stabilising the chassis motion with respect to the absolute frame and reducing the level of vertical vibrations perceived by the occupants. In other words, higher values of c_{sky} lead to a smoother body response, continuously enhancing ride comfort without introducing the rigid dynamic coupling effects that typically limit traditional passive suspensions.

To conclude the analysis of the Ideal Skyhook strategy, the following plot presents a comprehensive 3D surface response, which maps the combined influence of both the passive relative damping c_{rel} and the skyhook damping c_{sky} on the chosen ride comfort index. This representation makes it possible to outline potential trade-offs between passive and virtual damping contributions when defining an overall suspension tuning.

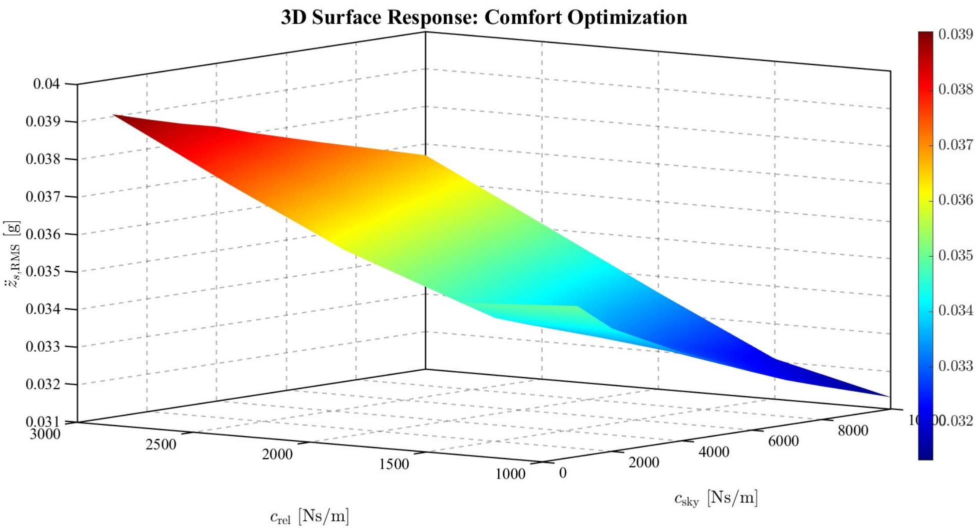

Figure 5.6: 3D surface response of the sprung mass acceleration RMS as a function of both relative damping c_{rel} and skyhook damping c_{sky}.

The surface clearly maps the dynamic interaction between the two parameters:

- The worst comfort conditions (indicated by the red region) occur when the system relies heavily on passive damping (high c_{rel}) with minimal or zero skyhook contribution;
- Conversely, the optimal comfort performance (the dark blue region representing the minimum RMS value) is achieved by maximizing the absolute skyhook damping (c_{sky}) while keeping the passive relative damping (c_{rel}) at its lower boundary.

This 3D visualization clearly illustrates the fundamental concept of the skyhook strategy: to ensure optimal passenger comfort, the system must reduce the traditional damping between the vehicle body and the wheels, relying instead on the virtual fixed reference.

5.2.3 Performance indexes as a function of the damping c_{ground}

After analyzing the comfort-oriented skyhook approach, the focus now shifts to the second advanced control strategy: the Ideal Groundhook. In this configuration, the system's dynamic performance is governed by the groundhook damping coefficient c_{ground}, which creates a virtual connection between the unsprung mass and the road profile.

This section investigates the variation of both the sprung mass acceleration RMS and the road holding index η_{RH} across a range of c_{ground} values. The resulting trends will highlight how this specific control logic operates to maximize tire grip and overall vehicle stability, providing a complementary perspective to the previous strategy.

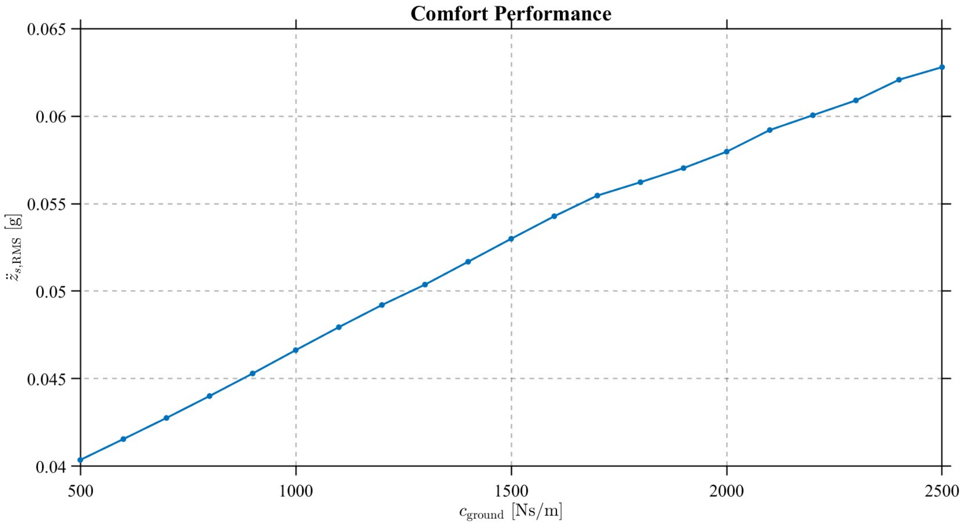

Figure 5.7: RMS value of the sprung mass acceleration as a function of the groundhook damping coefficient c_{ground}.

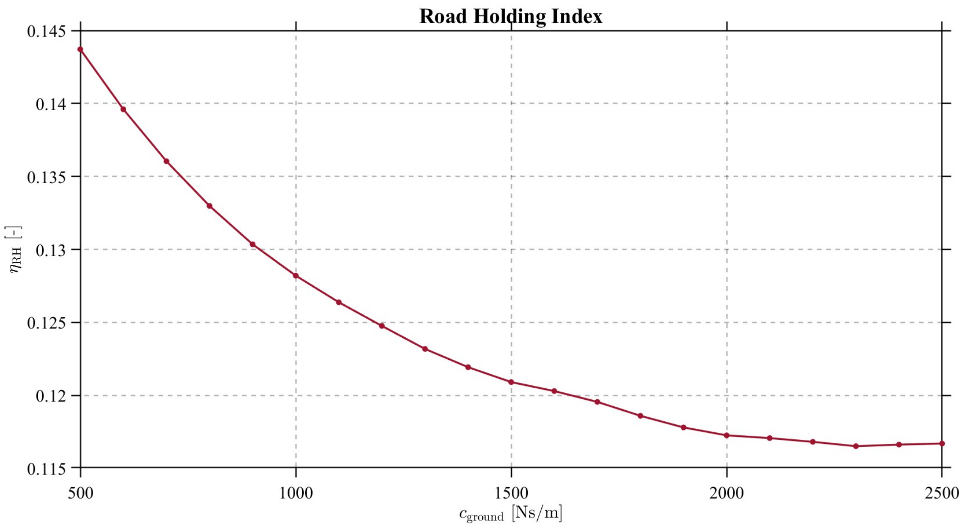

Figure 5.8: Road holding coefficient η_{RH} as a function of the groundhook damping coefficient c_{ground}.

The dynamic behaviour of the Ideal Groundhook strategy is illustrated in Figure 5.8. The analysis of the performance metrics highlights the following key characteristics:

- *Ride Comfort Degradation:* The **sprung mass acceleration RMS** exhibits a strictly increasing, nearly linear trend. As c_{ground} increases, the control logic forces the wheel assembly to closely track the road profile. While this tightly controls the unsprung mass, it inevitably transmits a higher level of road harshness and vibrations to the chassis, progressively worsening passenger comfort.

- *Road Holding Optimization:* Conversely, the **road holding coefficient** η_{RH} demonstrates a significantly decreasing (improving) trend, reaching an optimal minimum value near 2300 Ns/m. The virtual damping effectively suppresses the dynamic oscillations of the wheel, stabilizing the tire-road contact footprint and maximizing overall grip.

Unlike the skyhook approach, these trends demonstrate that the groundhook strategy heavily penalizes ride comfort to achieve its primary objective: the strict minimization of dynamic tire force variations to ensure maximum vehicle handling and safety.

To conclude the analysis of the Ideal Groundhook strategy, the plot in the following represents a comprehensive 3D surface response, illustrating the combined influence of the passive relative damping c_{rel} and the groundhook damping c_{ground} on the road holding index.

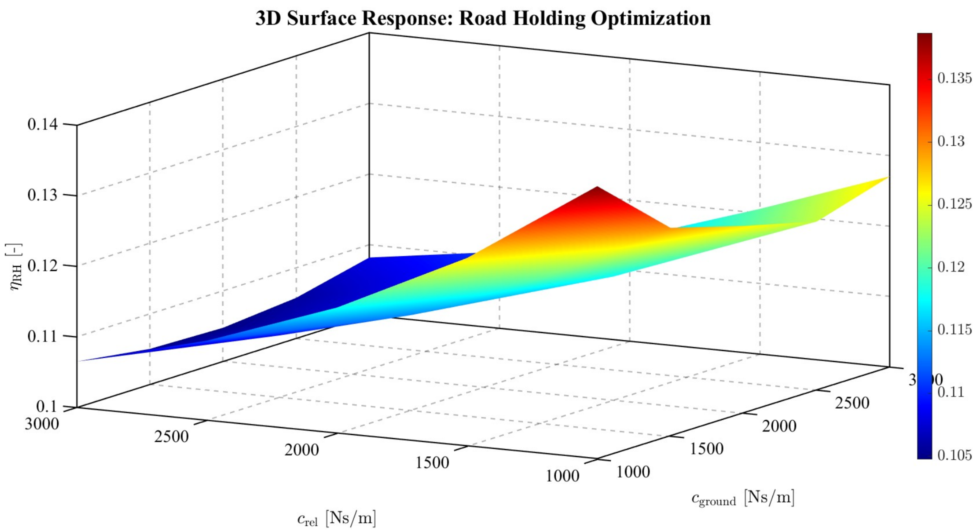

Figure 5.9: 3D surface response of the road holding index η_{RH} as a function of both relative damping c_{rel} and groundhook damping c_{ground}.

The surface maps the dynamic interaction between these two parameters, revealing their specific influence on the system:

- The worst road holding conditions (the red peak) occur when both damping coefficients are at their minimum (1000 Ns/m), leaving the wheel assembly underdamped and prone to large dynamic oscillations.
- Increasing the groundhook damping c_{ground} steadily improves tire grip, as the virtual connection to the road helps stabilize the unsprung mass.
- Nevertheless, the passive relative damping c_{rel} remains the dominant factor. The optimal road holding (the dark blue region) is achieved by maximizing c_{rel} (approaching 3000 Ns/m), largely independently of the specific c_{ground} value.

This confirms that while the groundhook strategy improves grip, a high passive damping is still the most effective way to suppress unsprung mass oscillations. However, as previously demonstrated, maximizing c_{rel} severely penalizes passenger comfort, reiterating the fundamental suspension trade-off.

Chapter 6

Conclusions and future works

6.1 Conclusions

This work presented a comprehensive workflow including the development, testing and control of a vehicle suspension system, starting with the construction of a custom vehicle model within the CarSim environment. To achieve a faithful representation of the physical system, the unsprung mass kinematics were defined through specific jounce-dependent curves. In addition, the dynamic response of the main suspension components, namely springs and shock absorbers, was modeled using dedicated force-displacement and force-velocity look-up tables.

To support the active control implementation, a co-simulation environment was configured between CarSim and Simulink. By explicitly defining the appropriate input and output variables, the multi-body vehicle model could communicate directly with the external control algorithms. Once assembled, the system was tested under different longitudinal velocities, road roughness profiles, and driving maneuvers to observe its baseline dynamic behavior.

The study then moved to a validation phase, comparing the custom model with a default CarSim vehicle and a standard quarter-car mathematical model. The structural and dynamic plausibility of the proposed vehicle was verified by evaluating the Root Mean Square (RMS) values of both the sprung mass accelerations and the vertical tire forces. Furthermore, the time-domain plots of these simulated quantities closely mirrored the dynamic trends of both reference models. This comprehensive alignment with the theoretical benchmarks confirmed that the vehicle correctly reproduces the fundamental vertical dynamics, making it a reliable platform for the subsequent control analysis.

In the final stage, this validated digital vehicle was employed to test two ideal semi-active control strategies: the Skyhook and the Groundhook. The application of the Skyhook logic effectively isolated the vehicle body from road disturbances, leading to a noticeable improvement in passenger comfort. Conversely, the Groundhook strategy minimized the dynamic fluctuations of the tire contact forces, maximizing overall grip and road holding. Ultimately, the results confirmed that the two architectures provide a viable solution to overcome the structural limits of passive systems, allowing to actively manage the traditional design trade-off between comfort and handling.

6.2 Future Works

Building upon the methodologies and the findings of this thesis, several promising directions for future research and development can be identified:

- *Implementation of Realistic Semi-Active Algorithms:* Transitioning from ideal control strategies to realistic, bounded algorithms (e.g., Clipped Skyhook) that account for the physical passivity constraints and the response times of real-world controllable dampers.
- *Advanced Control Architectures:* Exploring the application of more sophisticated optimal control techniques, such as Linear Quadratic Regulator (LQR) or Model Predictive Control (MPC), to handle multi-objective optimization (comfort and road holding) in real-time.
- *Hybrid Control Logics:* Developing an adaptive, hybrid Skyhook-Groundhook controller capable of automatically shifting its priority between ride comfort and tire grip based on instantaneous driving conditions, vehicle state, and road roughness estimation.
- *Experimental Validation:* Extending the validation phase through experimental testing on a physical test rig or a prototype vehicle. This would allow for the assessment of real-world phenomena not fully captured in simulation, such as sensor noise, communication delays and complex non-linearities in the suspension bushings.

Bibliography

[1] Samy Aly Hassan. «Fundamental Studies of Passive, Active and Semi-active Automotive Suspension Systems». PhD thesis. Leeds, UK: University of Leeds, Department of Mechanical Engineering, 1986 (cit. on p. 1).

[2] Jacob Kwaku Nkrumah, Sherry Kwabla Amedorme, Baba Ziblim, and David Inusah Offei. «Review of Suspension Control and Simulation of Passive, Semi-Active and Active Suspension Systems Using Quarter Vehicle Model». In: *American Scientific Research Journal for Engineering, Technology, and Sciences* 90.1 (2022), pp. 144–160 (cit. on p. 1).

[3] Thomas D. Gillespie. *Fundamentals of Vehicle Dynamics*. SAE International, 1992 (cit. on p. 2).

[4] P. S. Els. «The Ride Comfort vs. Handling Compromise for Off-Road Vehicles». In: *Journal of Terramechanics* (2005) (cit. on p. 2).

[5] *Sprung Mass – an overview*. ScienceDirect Topics (cit. on pp. 2, 3).

[6] Wikipedia contributors. *Unsprung mass*. Online encyclopedia. 2024 (cit. on p. 2).

[7] Rajesh Rajamani. *Vehicle Dynamics and Control*. 2nd ed. Springer, 2012 (cit. on p. 2).

[8] R. S. Sharp and S. A. Hassan. *Vehicle Suspensions: Handling and Ride*. SAE International, 1986 (cit. on p. 3).

[9] TEVEMA. *Introduction to Vehicle Suspension Springs*. Technical note (cit. on p. 3).

[10] Lesjöfors. *Understanding Vehicle Suspension Springs: A Complete Guide*. Technical note (cit. on p. 3).

[11] Wikipedia contributors. *Shock absorber*. Online encyclopedia. 2024 (cit. on p. 4).

[12] *How Shock Absorbers Function?* Automotive Q&A (cit. on p. 4).

[13] S. A. Author. «Passive Suspension System». In: *Encyclopedia of Automotive Engineering*. ScienceDirect topic overview on passive suspension systems. Elsevier, 2015 (cit. on p. 5).

[14] H. Li, X. Zhao, and Y. Wang. «Review of Suspension Control and Simulation of Passive, Semi-Active and Active Suspension Systems». In: *American Scientific Research Journal for Engineering, Technology, and Sciences* 87.1 (2022), pp. 45–63 (cit. on pp. 5–7).

[15] Aref M. A. Soliman and Mina M. S. Kaldas. «Semi-active suspension systems from research to mass-market – a review». In: *Journal of Low Frequency Noise, Vibration and Active Control* 38.4-5 (2019), pp. 1545–1574 (cit. on p. 6).

[16] Ahmad Hafizal Mohd Yamin, Mohd Firdaus Abas, Mohd Faizal Esa, Mohd Mustaqim Tukiman, Shafawi Ismail, Izzul Nisa' Muhamad Noor, and Muhammad Syakir Mohd Nasir. «Advancing Semi-Active Suspension Systems: A Comprehensive Review of Magneto-Rheological (MR) Dampers». In: *Advances in Fluid, Heat and Materials Engineering* (2024) (cit. on p. 11).

[17] Shuaishuai Sun, Xin Tang, Jian Yang, Donghong Ning, Haiping Du, Shiwu Zhang, and Weihua Li. «A New Generation of Magnetorheological Vehicle Suspension System With Tunable Stiffness and Damping Characteristics». In: *IEEE Transactions on Industrial Informatics* 15.8 (2019), pp. 4696–4708 (cit. on p. 12).

[18] Péter Gáspár, József Bokor, and Zoltán Szabó. «Modelling of Electro-Rheological Dampers for Automotive Suspension Systems». In: *Proceedings of the IFAC Workshop on Advances in Control and Automation Theory for Transportation Applications*. 2018 (cit. on p. 13).

[19] Min Yu, Simos A. Evangelou, and Daniele Dini. «Advances in Active Suspension Systems for Road Vehicles». In: *Engineering* 33 (2024), pp. 160–177 (cit. on pp. 13, 14, 16, 18, 19).

[20] Renato Galluzzi, Salvatore Circosta, Nicola Amati, and Andrea Tonoli. «Rotary regenerative shock absorbers for automotive suspensions». In: *Mechatronics* 77 (2021), p. 102580 (cit. on pp. 14, 15).

[21] Zhang Cheng. «Review of Structural Design and Control Methods for Active Suspension Systems in Automobiles». In: *International Journal of Science and Engineering Applications* 14.10 (2025), pp. 50–52. DOI: 10.7753/IJSEA1410.1007 (cit. on p. 16).

[22] Abhishek Goyal and Ashish Sharma. «Advances in Active Suspension System». In: *International Conference on Communication & Computational Technologies (ICCCT)*. IJCRT, 2017 (cit. on p. 16).

[23] Yuan-kui Sun and Xiao-bin Fan. «Research on the Application of CarSim in Vehicle Simulation and Development». In: *International Journal of Plant Engineering and Management* 22.4 (2017), pp. 200–211 (cit. on pp. 17–19).

[24] Mechanical Simulation Corporation. *CarSim Overview*. Accessed: June 2026. 2026 (cit. on pp. 17–19).

[25] Jiyuan Wang, Zhenxing Huang, Haodong Hong, Siyao Yu, Weihan Shi, and Xiaoliang Zhang. «Skyhook-Based Techniques for Vehicle Suspension Control: A Review of the State of the Art». In: *Machines* 13.8 (2025), p. 727 (cit. on pp. 75, 76).

[26] M. Farid Aladdin and Jasdeep Singh. «Modelling and Simulation of Semi-Active Suspension System for Passenger Vehicle». In: *Journal of Engineering Science and Technology* (2018). 7th EURECA 2016 Special Issue July, pp. 104–125 (cit. on pp. 75, 76).